

**A METHOD FOR PREDICTING LOCAL
STRUCTURE-INDUCED SEDIMENT SCOUR BASED
ON NEAR BOTTOM FLOW MEASUREMENTS**

by

Maximo Ramon Castillo Ramos III

Thesis

1993

A METHOD FOR PREDICTING
LOCAL STRUCTURE-INDUCED SEDIMENT SCOUR
BASED ON NEAR BOTTOM FLOW MEASUREMENTS

By

MAXIMO RAMON CASTILLO RAMOS III

A THESIS PRESENTED TO THE GRADUATE SCHOOL
OF THE UNIVERSITY OF FLORIDA IN PARTIAL FULFILLMENT
OF THE REQUIREMENTS FOR THE DEGREE OF
MASTER OF SCIENCE

UNIVERSITY OF FLORIDA

1993

ACKNOWLEDGEMENTS

I would like to express my sincere appreciation and gratitude to my advisor and supervisory committee chairman, Prof. D. Max Sheppard, for his continuous support and guidance throughout my study at the University of Florida. My thanks are also extended to Dr. Alan Wm. Neidoroda and Dr. Ashish J. Mehta for serving as members on my supervisory committee.

Many thanks go to Sidney Schofield, Jim Joiner, Chuck Broward, Vernon Sparkman, Danny Brown and the other members of the Coastal and Oceanographic Laboratory for their cooperation and assistance on this project. This work would not have been accomplished without the assistance of Mike Dombrowski, Suresh, Prashant and Kailash during the hydrodynamic and scour experiments.

I am also grateful to the Florida Department of Transportation for providing financial support for this research and to the Department of Civil Engineering at the University of Florida for allowing this research to be conducted in their Hydraulic Research Flume.

Thanks go to my fellow Coastals; Mark, Mike Del, Phil, Phil and Eric. A big thank you goes to my two best friends, Cherryl and Ica, for their love, patience and support. Finally, I am most grateful to my parents who showed me how important and enjoyable pursuing an education can be.

TABLE OF CONTENTS

ACKNOWLEDGEMENTS	ii
LIST OF TABLES	v
LIST OF FIGURES	vii
KEY TO SYMBOLS	xii
ABSTRACT	xiv
CHAPTER 1 INTRODUCTION	1
CHAPTER 2 LITERATURE REVIEW	5
2.1 Overview	5
2.2 Scour Measurements Around Multiple Pile Structures	6
2.3 Flow and Scour Depth Measurements Inside a Scour Hole	8
2.4 Flow Measurements Using Constant Temperature Anemometers	9
2.5 Sediment Transport Formulas	10
CHAPTER 3 PROBLEM STATEMENT AND METHODOLOGY	12
3.1 Problem Statement	12
3.2 Solution Method	13
3.3 Selection of Parameters and Scale Modeling	13
3.4 Experimental Plan and Test Facility	17
CHAPTER 4 HYDRODYNAMIC STUDY	22
4.1 Background	22
4.2 Experimental Procedures	27
4.3 Data Acquisition	32
4.3.1 X Sensor Probe	32
4.3.2 Temperature Probe	33
4.4 Data Reduction	38

CHAPTER 5 SCOUR STUDY	40
5.1 Background	40
5.2 Sediment	41
5.3 Instrumentation	44
5.4 Test Procedures	45
5.5 Data Acquisition	48
5.5.1 Echo Sounder	48
5.5.2 Potentiometer Readings	49
5.6 Data Reduction	49
5.7 Time Rate of Scour	57
 CHAPTER 6 ANALYSIS OF HYDRODYNAMIC AND SCOUR RESULTS	 63
6.1 Mathematical Model	63
6.2 Mathematical Model Results	66
 CHAPTER 7 RESULTS AND CONCLUSIONS	 80
7.1 Results	80
7.2 Conclusions	85
 APPENDIX A HYDRODYNAMIC STUDY	 89
A.1 Instrumentation	90
A.2 Temperature Correction	91
A.3 Vortex Shedding from Probe Holder	92
A.4 Preliminary Flow Measurements	93
 APPENDIX B SCOUR STUDY	 99
B.1 Instrumentation	100
B.2 Echo Sounder Head Angle Calibration	101
B.3 Sediment	105
 APPENDIX C DETAILED RESULTS	 107
 REFERENCE LIST	 129
 BIOGRAPHICAL SKETCH	 131

LIST OF TABLES

2.1	Some formulas for bed load and total load	10
3.1	Reynolds numbers for hydrodynamic and scour studies	18
3.2	Sequence of hydrodynamic tests	19
3.3	Sequence of scour tests	19
A.1	Constant temperature anemometer technical data	90
A.2	X sensor probe technical data	90
A.3	Temperature probe technical data	91
A.4	Variation of mean velocity with time at the same location	97
A.5	Variation of mean velocity across the tank in front of and away from the influence of the structure	97
A.6	X sensor probe cosine response - <u>probe vertical</u>	98
A.7	X sensor probe cosine response - <u>probe horizontal</u>	98
B.1	Echo sounder technical data	100
C.1	Values of x and y at grid points of hydrodynamic study	108
C.2	Results of hydrodynamic Test H-1	110
C.3	Results of hydrodynamic Test H-2	112
C.4	Results of hydrodynamic Test H-3	114
C.5	Predicted and measured bottom elevations for scour Test S-1 (no pile cap structure)	116

C.6	Predicted and measured bottom elevations for scour Test S-2 (70° pile cap structure - top position)	122
C.7	Predicted and measured bottom elevations for scour Test S-3 (70° pile cap structure - bottom position)	128

LIST OF FIGURES

3.1	Definition sketch of pile cap.	20
4.1	Shear stress profiles in front of and away from the influence of the structure	25
4.2	Velocity profile corresponding to shear stress profiles in Figure 4.1	25
4.3	Grid points for hydrodynamic study (1:1 scale)	26
4.4	Grid points for hydrodynamic study (distorted 1:4.5 scale)	26
4.5	Placement of test structure prior to hydrodynamic experiment	28
4.6	Experimental set-up for hydrodynamic study	28
4.7	Overall set-up of experimental apparatus and instrumentation for hydrodynamic study	29
4.8	Calibration curve for the temperature probe	30
4.9	Calibration curve for the X sensor probe	31
4.10	Unfiltered U and V velocity components for hydrodynamic Test H-1 at grid point B2	34
4.11	Filtered U and V velocity components for hydrodynamic Test H-1 at grid point B2	35
4.12	Power density spectra of U velocity components in Figures 4.10 and 4.11	36
4.13	Power density spectra of V velocity components in Figures 4.10 and 4.11	37
4.14	Mean velocity in front of structure vs. time	38

4.15	Turbulent energy/unit mass in front of structure vs. time	39
5.1	Overall set-up of experimental apparatus and instrumentation for scour study	42
5.2	Experimental set-up for scour study	43
5.3	Test area of flume showing no pile cap structure and central region near structure	43
5.4	Calibration curve for the echo sounder output signal	45
5.5	Modified calibration curve for echo sounder angle.	46
5.6	Unfiltered output signals after completion of Test S-1	50
5.7	Filtered output signals after completion of Test S-1	51
5.8	Power density spectra of echo sounder output (Channel CH00) in Figures 5.6 and 5.7	52
5.9	Power density spectra of y position potentiometer (Channel CH03) in Figures 5.6 and 5.7	53
5.10	Definition sketch showing measurements needed for conversion of raw data to x-y coordinates	55
5.11	Data points before start of scour Test S-1 (No pile cap structure)	56
5.12	Data points after completion of scour Test S-1 (No pile cap structure) . . .	56
5.13	Time rate of scour of piles 1,2 and 6 of no pile cap structure	58
5.14	Time rate of scour of piles 1,2 and 6 of 70° pile cap (top position) structure	59
5.15	Time rate of scour of pile 1	60
5.16	Time rate of scour of pile 2	61
5.17	Time rate of scour of pile 6	62

6.1	Comparison of measured bottom elevation, predicted equilibrium bottom elevation and dimensionless shear stress for the no pile cap structure (row 2 : x = 10 cm)	67
6.2	Comparison of measured bottom elevation, predicted equilibrium bottom elevation and dimensionless shear stress for the no pile cap structure (row 3 : x = 40 cm)	68
6.3	Comparison of measured bottom elevation, predicted equilibrium bottom elevation and dimensionless shear stress for the no pile cap structure (row 4 : x = 70 cm)	69
6.4	Comparison of measured bottom elevation, predicted equilibrium bottom elevation and dimensionless shear stress for the no pile cap structure (row 5 : x = 100 cm)	70
6.5	Comparison of measured bottom elevation, predicted equilibrium bottom elevation and dimensionless shear stress for the no pile cap structure (row 6 : x = 130 cm)	71
6.6	Comparison of measured bottom elevation, predicted equilibrium bottom elevation and dimensionless shear stress for the no pile cap structure (row 7 : x = 160 cm)	72
6.7	Comparison of measured bottom elevation, predicted equilibrium bottom elevation and dimensionless shear stress for the 70° pile cap (top) structure (row 2 : x = 10 cm)	73
6.8	Comparison of measured bottom elevation, estimated and predicted equilibrium bottom elevations and dimensionless shear stress for the 70° pile cap (top) structure (row 3 : x = 40 cm)	74
6.9	Comparison of measured bottom elevation, predicted equilibrium bottom elevation and dimensionless shear stress for the 70° pile cap (top) structure (row 4 : x = 70 cm)	75
6.10	Comparison of measured bottom elevation, predicted equilibrium bottom elevation and dimensionless shear stress for the 70° pile cap (top) structure (row 5 : x = 100 cm)	76
6.11	Comparison of measured bottom elevation, predicted equilibrium bottom elevation and dimensionless shear stress for the 70° pile cap (top) structure (row 6 : x = 130 cm)	77

6.12	Comparison of measured bottom elevation, predicted equilibrium bottom elevation and dimensionless shear stress for the 70° pile cap (top) structure (row 7 : x = 160 cm)	78
6.13	Comparison of measured bottom elevation, predicted equilibrium bottom elevation and dimensionless shear stress for the 70° pile cap (bottom) structure (row 1 : x = 10 cm)	79
7.1	Contours of dimensionless shear stress, τ_d , around no pile cap structure .	82
7.2	Contours of dimensionless shear stress, τ_d , around 70° pile cap (top position) structure	82
7.3	Contours of measured bottom elevation around no pile cap structure after completion of the scour test	83
7.4	Contours of predicted equilibrium bottom elevation around no pile case structure	83
7.5	Contours of measured bottom elevation around 70° pile cap (top position) structure after completion of the scour test	84
7.6	Contours of predicted equilibrium bottom elevation around 70° pile cap (top position) structure	84
7.7	70° pile cap (bottom position) structure before the scour test	87
7.8	70° pile cap (bottom position) structure after completion of the scour test	87
7.9	70° pile cap (top position) structure before the scour test	88
7.10	70° pile cap (top position) structure after completion of the scour test . . .	88
A.1	Mean velocity vs number of data points sampled	95
A.2	Variation of mean velocity parallel to the 70° pile cap (top position) structure	96
A.3	Variation of mean velocity normal to the 70° pile cap (top position) structure	96
B.1	Calibration curve for the echo sounder head angle	101
B.2	Profile of flat bottom using original calibration curve	103

B.3	Modified calibration curves of the echo sounder head angle	104
B.4	Profile of flat bottom using modified calibration curves	104
B.5	Sediment size distribution for Category 1 sand (away from structure). . .	105
B.6	Sediment size distribution for Category 2 sand (anchoring layer)	106
B.7	Sediment size distribution for Category 3 sand (around structure)	106

KEY TO SYMBOLS

a	dimensionless constant relating $-\overline{u'w'}$ and $u'^2 + v'^2$
b	dimensional empirical coefficient in $de=f(\tau)$
c	dimensionless empirical coefficient in $de=f(\tau)$
de	scour depth
de_p	predicted equilibrium scour depth
de_e	estimated equilibrium scour depth
de_m	measured scour depth after 28 hours
d_{50}	median sediment diameter (0.60 mm)
d	diameter of probe holder
D	diameter (or width) of piles
f_v	vortex shedding frequency of probe holder
g	acceleration of gravity
h	water depth
k	dimensionless constant relating $u'^2 + v'^2$ and $u'^2 + w'^2$
S_t	Strouhal Number; $f_v d/U$
T	water temperature
u'	fluctuating velocity component in x direction

U	velocity component in x direction
U_c	value of U where motion of sediment with sediment diameter d_{50} is initiated on a flat bottom away from the structure
v'	fluctuating velocity component in y direction
V	velocity component in y direction
w'	fluctuating velocity component in z direction
W	velocity component in z direction
x	position along the tank (in line to flow)
y	position across the tank (transverse to flow)
z	distance from the bottom (positive upward)
Θ	angle of echo sounder head with vertical
ϕ	sediment angle of repose (32°)
ρ	water density
ρ_s	sediment density
τ_d	dimensionless shear stress, ratio of τ and τ_o
τ	near-bottom shear stress
τ_v	viscous near-bottom shear stress
τ_t	turbulent near-bottom shear stress
τ_o	near-bottom shear stress away from influence of structure
τ_{vo}	viscous near-bottom shear stress away from influence of structure
τ_{to}	turbulent near-bottom shear stress away from influence of structure
μ	dynamic (absolute) viscosity

Abstract of Thesis Presented to the Graduate School
of the University of Florida in Partial Fulfillment of the
Requirements for the Degree of Master of Science

A METHOD FOR PREDICTING
LOCAL STRUCTURE-INDUCED SEDIMENT SCOUR
BASED ON NEAR BOTTOM FLOW MEASUREMENTS

By

Maximo Ramon Castillo Ramos III

May 1993

Chairperson: Dr. D. Max Sheppard
Major Department: Department of Coastal and Oceanographic Engineering

A method of predicting equilibrium scour depths around multiple pile structures based on pre-scoured bottom shear stress was developed in this study. It was hypothesized that a relationship exists between the pre-scoured bottom shear stress and the equilibrium scour depth. A series of hydrodynamic tests were conducted in which near-bottom flow measurements were made in the vicinity of a variety of multiple pile structures. The distribution of bottom shear stress was estimated from these flow measurements. Scour tests were then made in the same flume using the same structures. A simple relationship between the equilibrium scour depth and the pre-scoured bottom shear stress was formulated and the data from the two sets of experiments were used to calibrate and test the formulation. The formulation gives reasonable predictions for the range of conditions tested. The approach appears promising as an alternative way of

estimating equilibrium local scour depths for complex multiple pile structures. In addition, a number of interesting and useful findings were made regarding the rate at which a local scour hole forms near complex structures.

CHAPTER 1 INTRODUCTION

Most bridge piers are supported by piles. The friction between these piles and the surrounding sediment is essential to the structural integrity of the bridge. If the stream bed elevation drops such that more of the piles are exposed, the structure is significantly weakened.

There are several ways in which the stream bed elevation can change. One mechanism is aggradation or degradation of the stream bottom. This results from changes in the flow conditions and would occur whether the bridge was present or not. Although the aggradation/degradation of the stream is not caused by the presence of the bridge, this must be considered during the design of the bridge and its piers. Another cause of stream bed elevation change is contraction scour. If the cross-sectional area of the flow is decreased, there is a corresponding increase in flow velocity. Depending on the size of the bridge piers relative to the stream cross-sectional area, a significant amount of contraction scour can be caused by the presence of the bridge. The third mechanism is local scour. This is due to the individual elements of the bridge and is, in general, the most important factor regarding stream bed elevation changes around a pier (Shen et al., 1966). In addition to local scour, if the structure foundation is composed of multiple piles, this may result in global or dishpan scour. Jones (1989) found that when the piles are in close proximity to each other, $a/D < 3$, where a is the

distance between pile centers and D is the pile diameter, the characteristic width to be used in the pier scour equation is the sum of the widths of the piles. For $3 < a/D < 11$, both local and global scour are present, and for $a/D > 11$, the piles act as individual structures (Hannah, 1978).

As mentioned above, local scour is considered to be the most important factor of stream bed elevation change around a bridge pier. The main scour mechanism for steady flow around blunt vertical structures is thought to be the horseshoe vortex. This vortex is caused by a vertical gradient in the stagnation pressure along the leading edge of the structure resulting from velocity gradients in the bottom boundary layer (see e.g. Sheppard and Niedoroda, 1990). The presence of the bridge pier also tends to accelerate the flow around the structure which leads to an increase in the bottom shear stress.

During the past few years, several bridges in the United States have failed due to sediment scour. These accidents have resulted in fatalities and significant loss of property. Among the more recent bridge failures, are the New York Thruway bridge over Schoharie Creek in 1987 and a bridge on US 51 over the Hatchie River in Tennessee in 1989. These cases served to raise the level of concern among engineers responsible for the design and maintenance of bridges. Over the last few decades, various researchers have developed methods for predicting scour depths around bridge piers under extreme flow conditions.

All of the sediment scour mechanisms listed above are complex and difficult if not impossible to treat analytically. Computational approaches using large, high speed computers have not to date been successful in predicting sediment scour even for simple

structures. Consequently, researchers have resorted to empirical equations based primarily on laboratory data. A large number of experiments have been performed with simple structures such as circular and rectangular cylinders (see Shen et al., 1966). Fewer tests have been made with multiple pile structures (Hannah, 1978 and Sheppard and Niedoroda, 1992). There are many flow, sediment and structure variables important to the scour process. A large number of experiments are needed to examine the effects of each quantity on the scour process. Most laboratory tests have used prototype sediment and water while scaling many of the other parameters. This always raises questions regarding scale effects when relating model results to prototype conditions.

These problems motivated the approach taken in this thesis, which was an attempt to predict scour depths from near-bottom flow measurements over a fixed bed. The bottom shear stresses were estimated from flow measurements taken in the region surrounding the structure where local scour was anticipated. If the scour depths around a structure can be determined from these flow measurements, it would reduce the need for moveable bed scour tests. One of the problems with this approach, is that the flow pattern around the structure can be significantly altered as the scour hole deepens. The question then is whether there is sufficient information in the pre-scoured bottom shear stress to predict equilibrium scour depths.

A similar approach has been used in fixed bed models for sediment transport in coastal areas. A coastal structure like a jetty may need to be lengthened or have its shape altered. A (usually distorted) fixed bed scale model of the area of interest is constructed in a basin. Waves and/or currents are generated and the flow around the

various structure configurations being considered is measured. The sediment transport throughout the region is then estimated using the measured velocities.

The objectives of this study were to 1) estimate the bottom shear stress in the vicinity of a complex pier structure from near-bottom flow measurements and 2) estimate the equilibrium local scour depth near the structure using the pre-scoured bottom shear stress. The prediction scheme was calibrated using scour measurements from tests made with the same multiple pile models. It was assumed that the relation between the bottom shear stress and the equilibrium scour depths will hold if the structure configuration exposed to the flow does not change significantly as the scour hole develops. The structure configurations considered included a multiple pile pier without a pile cap and the same structure with a pile cap at two different vertical locations. The flow conditions (water depth and flow velocity) and mean sediment size were maintained constant throughout both the hydrodynamic and scour tests.

CHAPTER 2 LITERATURE REVIEW

The following chapter is a literature review of several fields of study and their approaches to solving flow-structure interaction problems. The review will cover: 1) scour experiments around multiple pile structures, 2) flow and scour depth measurements around and inside the scour hole, 3) fluid measurements using constant temperature anemometers and 4) sediment transport formulas. The approaches used in these fields can be combined to develop a method of relating near bottom hydrodynamic flow measurements to bottom shear stress. The shear stress measurements can then be used to predict scour depths around piers with pile caps or footings.

2.1 Overview

Most bridge piers are designed with footings and piles and it is not clear how the location and type of footing affects the scour depth around the pier. The presence of the footing makes it difficult to apply the scour depth equations developed for simple shapes. In order to determine the effect of the footing, it is usually necessary to conduct scale model tests to determine the scour depths. The limitation of this method would be the amount of time and expense needed to cover a large number of pier and footing configurations. If a relation between equilibrium scour depths and prescoured bottom shear stress can be developed, this would allow more pier and footing combinations to be studied.

2.2 Scour Measurements Around Multiple Pile Structures

There have been numerous authors such as Shen (1966), Melville and Raudkivi (1977) and Sheppard and Niedoroda (1992) who have conducted scour experiments around simple structures such as circular and rectangular cylinders. As a result of these experiments, a number of predictive equations have been developed. On the other hand, very little scour data exists for multiple pile structures. A brief discussion of the multiple pile structure papers reviewed as part of this study is given below.

Jones, Kilgore and Mistichelli (1992). Jones investigated the effect of the vertical location of a footing on local scour. He conducted scour experiments on a 1:50 scale model of a pier from the Baldwin Bridge in Connecticut. The experiments were performed in a 21.3 m long and 1.8 m wide tilting flume. Since the flume was unable to recirculate sediment, Jones was limited to clear water experiments with the flow slightly below incipient motion for the sediment in the test area. The sediment used in the tests had a d_{50} of 0.38 mm.

The model was a 9.7 cm wide pier with a 19.7 cm wide footing. The footing was designed such that it could be moved up or down in the flow field. The footing was modified to add an extension to the upstream face because Jones believed that without the extension, the original footing would have little effect on the diving currents associated with pier scour. The position of the footing ranged from slightly below the bed to the full flow depth.

The duration of the tests were 4 hours. At 4 hours, the rate of change in scour depth appeared to be negligible. Although other researchers have performed longer tests, Jones pointed out that those tests were for larger grain sizes.

The results indicate that local pier scour was reduced if the footing was flush or slightly below the bed. The scour hole depth and width increased as a larger percent of the footing was exposed to the flow.

Jones, Stein and Kilgore (1990). These researchers investigated the effects of varying the footing location relative to the stream bed. Clear water experiments were conducted on a 1:50 model of a pier of the Acosta Bridge in Jacksonville, Florida. At the start of the test, the flow was first set to that of incipient sediment motion. After reaching this flow, a pier was placed into the sand and allowed to scour for 4 hours.

The footing of the model tested was 0.51 m long, 0.46 m wide and 0.09 m thick and the pier was 0.46 m long and 0.17 m wide. The entire model was then moved up or down relative to the bed such that the footer would be at different flow levels. The results indicate that the scour depth is not greatly influenced by the footing location if the footing is at or above the bed. The pier in this study did not extend all the way to the bottom. Below the footing were piles that extended through the bed. It should be noted that the footer could not be moved up or down relative to the model. This resulted in different pile lengths for each test case and led the researchers to consider the results inconclusive.

2.3 Flow and Scour Depth Measurements Inside a Scour Hole

It is difficult to relate hydrodynamic flow measurements before scour begins around the structure to the actual scour depths because as the scour hole develops, the flow changes. The flow in the equilibrium scour hole may not resemble that of the pre-scour flow measurements. This section reviews experiments on cylinders which compare hydrodynamic flow measurements in and around a scour hole and the resulting scour depths.

Melville and Raudkivi (1977). Melville conducted clear water experiments on a 5.08 cm diameter cylinder in a flume 19 m long, 0.46 wide and 0.44 deep. The sediment used in these experiments had a d_{50} of 0.385 mm. The tests covered three stages of scour (initial flat bed, intermediate scour hole after 30 minutes from start and equilibrium scour hole). After each stage, a concrete (fixed bed) model was made of the scour hole using plaster-of-paris. The sand in the live bed experiments was used to coat the concrete model which was then placed in the tank. The researchers found the static angle of repose of the sand under water to be 32° .

The velocity and turbulence intensities in and around the scour hole were measured with a constant temperature anemometer using a single component conical probe. The mean bed shear stress was estimated using the mean velocity measurements at 2 mm above the bed such that

$$\tau = K \frac{\Delta \bar{u}}{\Delta y}, \quad (2.1)$$

where

$\Delta \bar{u}$ = local mean velocity at 2 mm from the bed,

Δy = 2 mm and

K = 2 kg•mm/m² (a calibration constant).

Melville found that the location of the maximum bed shear stress was where the scour hole first developed. The results also show that the locations of large bed shear stress correspond to regions of low turbulent intensity.

Carstens and Sharma (1975). The researchers found that the scour depths they measured near a 11.5 cm diameter cylinder were similar to maps of shear stress distribution of Hjorth (1974) around a 7.5 cm diameter cylinder. Hjorth conducted experiments on cylinders and measured bed shear stresses on a fixed bed up to 12 times higher than that of the undisturbed flow.

Carstens and Sharma noted that the scour hole covered a larger area than the zone of high shear stress. Studies have also found the bed shear stress in a scour hole to be 75% of the theoretical critical value for the sediment. Raudkivi (1976) attributed this to increased turbulence with strong intermittent eddies present.

2.4 Flow Measurements Using Constant Temperature Anemometers

Constant temperature anemometers measure fluid velocity by sensing the changes in heat transfer from a sensor exposed to fluid motion. Constant temperature anemometers have several features that make them suitable for turbulence studies (Goldstein, 1983). These anemometers have a high frequency response which allows it to measure the fluctuating components of the flow. Measurements up to several hundred

Khz are easily performed. Constant temperature anemometers are generally small in size which allows point measurement. A hot-wire sensor is typically 5 μm in diameter and about 2 mm long.

2.5 Sediment Transport Formulas

Sediment can be transported as bed load or suspended load near the bed. Bed load transport occurs when sediment next to the bed moves by rolling and sliding. During this time, the sediment remains close to the bed. Another method of transport, called saltation, is when the sediment performs jumps. The sediment is temporarily carried in the flow and then returns back to the bed. Total load refers to the sum of the bed load and the part of the suspended load that can also be found in the bed (Sleath, 1984). A list of some of the sediment transport formulas are shown in Table 2.1

Table 2.1 Some formulas for bed load and total load (Sleath, 1984).

Investigator	Formula	Comments
Du Boys (1879)	$Q_s = A\tau_o(\tau_o - \tau_c)$	Bed Load
O'Brien and Rindlaub (1934)	$Q_s = A(\tau_o - \tau_c)^m$	Bed Load
Shields (1936)	$Q_s = AQS(\tau_o - \tau_c) / ((\rho_s - \rho)gD)$	Bed Load
Brown (1950)	$Q_s = AD^{3/2}(\tau_o / ((\rho_s - \rho)gD)^3)$	Bed Load
Garde and Albertson (1958)	$Q_s = Q(D/d)f(D) (u_*d/\nu)^{2/3}$	Total Load
Chang et al. (1967)	$Q_s = A\bar{U}(\tau_o - \tau_c)$	Total Load

where

- Q_s = bed load transport rate,
- τ_c = critical shear stress on the bed for initial motion,
- τ_o = bed shear stress,
- \bar{u}_* = shear velocity, $(\tau/\rho)^{1/2}$ and
- A = constant or dependent on sediment characteristics.

Table 2.1 lists just a few of the sediment transport formulas that are based on bottom shear stresses. Note that the powers that the shear stress are raised to vary from 0.33 to 3.0.

CHAPTER 3 PROBLEM STATEMENT AND METHODOLOGY

3.1 Problem Statement

Structure-induced sediment scour has been studied by various researchers over the past few decades. Most experiments have been conducted on simple structures such as circular and rectangular cylinders and several predictive equations have been developed based on these experiments. Structures with multiple piles such as bridge piers and offshore oil platforms are also of interest. The flow near these structures is more complex and the scour more difficult to predict than the single element structure. The offshore industry divides the scour that occurs near structures into two categories, local and dishpan (or global). In this case, local refers to the scour adjacent to each piling and dishpan to the depression around the entire structure. Hydraulics engineers working with bridge pier scour combine the two and call it local scour.

Bridge piers come in many shapes and sizes. Some bridge piers are designed with a footing or pile cap. The presence of the pile cap usually complicates the flow field due to the enhanced turbulence and the size and complexity of the wake region. In general, the equations developed for simple structures cannot be used for these multiple pile structures. Thus, there is a need for innovative ways of dealing with this problem.

3.2 Solution Method

Due to the limited data for multiple pile structures, the scour prediction equations that exist are by necessity conservative to allow for uncertainties in both the data and the equations. Properly conducted scour tests are expensive and time consuming. The time required to reach equilibrium scour depths increases with the size and complexity of the structure. The results of this study clearly show that portions of the scour hole are far away from equilibrium after 28 hours of steady flow in the flume. This provided motivation for the approach taken in this thesis.

It was hypothesized that the equilibrium scour depths near a structure are related to the bottom shear stresses on the pre-scoured bed. To test this hypothesis, near-bottom flow measurements (from which bottom shear stresses could be estimated) were made near complex multiple pile structures. Sediment scour tests were then made in the same flume with the same structures and flow conditions. A simple relationship between equilibrium scour depth and bottom shear stress was formulated and data from the two sets of experiments were used to calibrate and test the formulation.

3.3 Selection of Parameters and Scale Modeling

The phenomenon of local structure-induced sediment scour depends on several flow and structure parameters (Sheppard and Niedoroda, 1990). These include the aspect ratio (h / D) , the sediment regime number $(U/U_c - 1)$, the Froude Number $(U / \sqrt{g h})$ and to a lesser extent, the Reynolds Number $(UD\rho / \mu)$, where

h = water depth,

- D = diameter (or width) of pile,
- U = depth (and time) average flow velocity,
- U_c = value of U where motion of sediment with diameter d₅₀ is initiated on a flat bottom away from the structure,
- ρ = mass density of water,
- μ = dynamic viscosity of water and
- g = acceleration of gravity.

Similitude modeling in open channel flow experiments can be performed using Froude or Reynolds scale modeling. If Froude scale modeling is used to achieve similarity between the model and prototype, the ratio of the inertia and gravity forces for the model should be equal to the ratio for the prototype, i.e.

$$\left(\frac{F_i}{F_g} \right)_m = \left(\frac{F_i}{F_g} \right)_p, \quad (3.1)$$

where F denotes force, i inertia, g gravity, m model and p prototype. Substituting the expression for these forces in terms of the physical properties, length scales and flow kinematics results in

$$\left(\frac{\rho V^2 L^2}{\rho g L^3} \right)_m = \left(\frac{\rho V^2 L^2}{\rho g L^3} \right)_p \quad (3.2)$$

or

$$\left(\frac{V^2}{g L} \right)_m = \left(\frac{V^2}{g L} \right)_p \quad (3.3)$$

or

$$\frac{(V_m / V_p)^2}{(g_m / g_p)(L_m / L_p)} = 1. \quad (3.4)$$

Note that

$$g_m = g_p, \quad (3.5)$$

thus

$$\frac{V_m^2}{V_p^2} = \frac{L_m}{L_p} \quad (3.6)$$

or

$$\frac{V_p}{V_m} = \sqrt{\frac{L_p}{L_m}}. \quad (3.7)$$

Let

$$\frac{L_p}{L_m} = \lambda, \quad (3.8)$$

then Equation 3.7 becomes

$$\frac{V_p}{V_m} = \sqrt{\lambda}. \quad (3.9)$$

On the other hand, if Reynolds scale modeling is used, the ratio of inertia to viscous forces for the model should be equal to the ratio for the prototype, i.e.

$$\left(\frac{F_i}{F_v} \right)_m = \left(\frac{F_i}{F_v} \right)_p, \quad (3.10)$$

where F denotes force, i inertia, v kinematic viscosity, m model and p prototype. Substituting the expressions for these forces in terms of the physical properties, length scales and flow kinematics results in

$$\left(\frac{\rho V^2 L^2}{\rho \nu V L} \right)_m = \left(\frac{\rho V^2 L^2}{\rho \nu V L} \right)_p. \quad (3.11)$$

In these experiments, water of similar mass density and viscosity to that of the prototype are used. Therefore

$$\rho_m = \rho_p \quad (3.12)$$

and

$$\nu_m = \nu_p. \quad (3.13)$$

Substituting Equations 3.12 and 3.13 into Equation 3.11 results in

$$(V L)_m = (V L)_p \quad (3.14)$$

or

$$\frac{V_p}{V_m} = \frac{L_m}{L_p} \quad (3.15)$$

Combining Equations 3.15 and 3.8 gives

$$\frac{V_p}{V_m} = \frac{1}{\lambda} \quad (3.16)$$

By comparing Equations 3.9 and 3.16, it is evident that both Froude and Reynolds scaling cannot be achieved for the problem under consideration without considerable effort and expense. Both the flow and sediment transport are less dependent on the Reynolds Number in the range of the flow parameters of interest in these tests (see Table 3.1) than the Froude Number. Table 3.1 lists the Reynolds Numbers based on the pile cap widths and the individual pile widths for the hydrodynamic and scour studies. Based on this, Froude scale modeling was used for the hydrodynamic and scour experiments.

3.4 Experimental Plan and Test Facility

Two sets of laboratory experiments were conducted on a 1:15 scale model of a bridge pier. The first set of experiments consisted of hydrodynamic tests on a bridge pier with and without a pile cap. Table 3.2 lists the hydrodynamic tests that were

Table 3.1 Reynolds numbers for hydrodynamic and scour studies.

	Hydrodynamic Study		Scour Study	
	prototype	model	prototype	model
Water depth (m)	5.33	0.36	5.85	0.39
Design Velocity (m/sec)	1.12	0.29	1.22	0.31
Re (based on pile cap width)	1.02×10^7	1.75×10^5	1.11×10^7	1.87×10^5
Re (based on pile width)	0.98×10^6	1.69×10^4	1.06×10^6	1.80×10^4

conducted. The type and location of the pile cap relative to the bottom was varied and near-bottom flow measurements were made over a portion of the area where scour was anticipated. A pile cap with 70° sides was used in these experiments (see Figure 3.1). Experiments were performed without the pile cap and with the pile cap at two different positions relative to the bottom. The no pile cap case represents the situation where the pile cap is positioned above the water surface. For the second position, the top of the 12.7 cm thick pile cap was 1.3 cm above the water surface. In the third position, the bottom of the pile cap was resting on the flume bottom. The second set of experiments consisted of sediment scour tests with the same multiple pile structures. A list of the scour tests that were conducted is given in Table 3.3. The hydrodynamic and scour tests had a flow skew angle of 0° , i.e. the flow was in line with the pier. During the sediment scour tests, an echo sounder was used to map the bottom in the vicinity of the pier

Table 3.2 Sequence of hydrodynamic tests.

Test Number	Pile Cap Type	Pile Cap Location
H-1	No Pile Cap	NA
H-2	70° Pile Cap	Top
H-3	70° Pile Cap	Bottom

Table 3.3 Sequence of scour tests.

Test Number	Pile Cap Type	Pile Cap Location
S-1	No Pile Cap	NA
S-2	70° Pile Cap	Top
S-3	70° Pile Cap	Bottom

before, during and after the 28 hour duration tests. Mechanical (point gauge) measurements were also made at the end of each test.

These experiments were conducted in the Hydraulics Research Flume in the Civil Engineering Department at the University of Florida. This recirculating flume has a flat, fixed bottom and the main flume is 30 m long, 2.44 m wide and 0.75 m deep. The flow is generated by a 100 hp pump with a maximum discharge of 1100 liters/sec. The flow rate and depth are controlled by a V-notch weir at the entrance and a tail gate at the downstream end of the flume. The water returns to the pump in a return channel 34 m

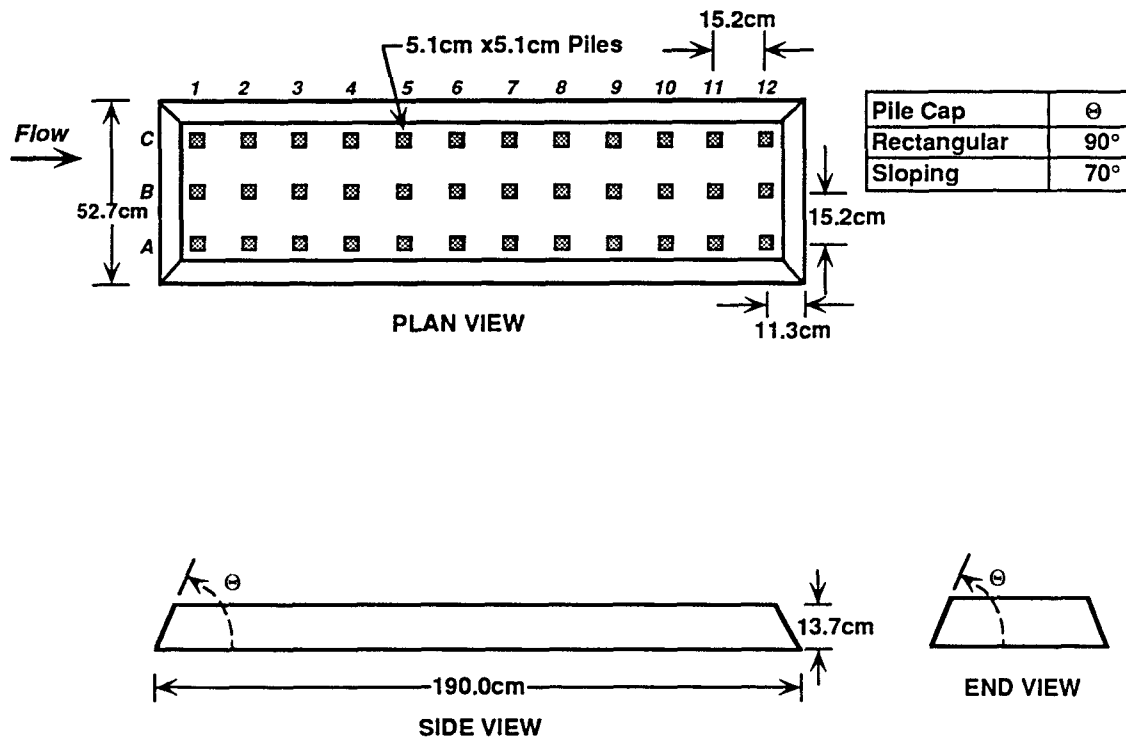


Figure 3.1 Definition sketch of pile cap.

long, 1.22 m wide and 1.00 m deep. Since the pump was not designed to recirculate sediment, a "sediment trap" was built prior to the sediment scour tests and placed at the downstream end to prevent sediment removed from the test area from reaching the pump.

The flume also has a 6.10 m long, 2.44 m wide and 0.33 m deep recess located approximately 13 m downstream from the entrance. During the hydrodynamic flow measurements, the recess was covered with metal plates. To obtain a uniform roughness, a layer of sand was glued to the plates. The plates were removed and the recess filled with sand for the scour tests.

CHAPTER 4 HYDRODYNAMIC STUDY

4.1 Background

As stated in the introduction, the primary objective of this study was to determine if equilibrium local scour depths can be predicted from near-bottom flow measurements over the pre-scoured bed near a multiple pile structure. The hydrodynamic study with the fixed bed is discussed in this chapter and the scour study is discussed in Chapter 5.

Sediment transport is a complex process but it is generally believed that the movement of sediment is related to the shear stress at the bed. For this reason, an attempt was made to estimate the bottom shear stress from flow measurements at a fixed distance above the bed (3 mm). In a fully developed open channel flow, estimation of the bottom shear stress is relatively straight forward. This is not the case for the complex "wake region" near a multiple pile structure and certain assumptions regarding the stress distributions had to be made. To further complicate the situation, the mean flow direction near the structure was found to vary with time as a result of the vortices being alternately shed by the piles and pile cap.

A two component Dantec 56C01 constant temperature anemometer was used for the flow measurements. The response of the Dantec R61 X sensor probe used was such that the high frequency fluctuating components of the velocity could be measured. It was

determined that when the X sensor probe was mounted such that the filaments lie in parallel vertical planes, variations in the mean velocity direction in a horizontal plane could not be resolved. That is, when the probe is orientated to measure velocities in the x (horizontal) and z (vertical) directions, changes in the direction of the horizontal velocity were not detected. This is to be expected since the probe is not designed for this flow situation. This means that the turbulent component of the shear stress, $-\rho\overline{u'v'}$, could not be accurately measured near the structure where the horizontal component of velocity undergoes fluctuations in direction as large as $\pm 15^\circ$. Ordinarily, the horizontal and vertical velocities would be measured and the mean horizontal velocity, \bar{U} , and time average of the product $u'w'$ computed in order to determine the total shear stress

$$\tau = \mu \frac{\partial \bar{U}}{\partial z} - \rho \overline{u'v'} . \quad (4.1)$$

To avoid the problem of the probe not being able to resolve variations in flow direction, it was decided to rotate the probe 90° so that the filaments were in parallel, horizontal planes. In this position, the probe measures the two horizontal components of velocity, U and V. It was assumed that the turbulent shear stress is proportional to $\rho(u'^2 + v'^2)$. The total shear stress would then be

$$\tau = \mu \frac{\partial \bar{U}}{\partial z} + a\rho(u'^2 + v'^2) , \quad (4.2)$$

where "a" is a constant to be determined from measurements in front of the structure at $x = -150.0$ cm and $z = 3$ mm. The analysis resulted in a value of 0.10 for "a".

The value of "a" in front of the structure at different heights ($z = 23.5, 105.5$ and 187.5 mm) above the bottom ranged from 0.08 to 0.12. The value of "a" next to the structure ranged from 0.04 to 0.09. The lower values of "a" next to the structure were probably due to the inability of the X sensor probe to resolve variations in the mean flow direction. Based on the above, a value of 0.10 was used throughout the flow field.

Figure 4.1 compares the shear stress profiles in front of and away from the influence of the structure computed using Equations 4.1 and 4.2. The shear stress profiles are similar and at $z = 3$ mm both give the same value for τ (0.22 N/m^2). The velocity profile corresponding to the shear stress profiles in Figure 4.1 is shown in Figure 4.2. A dimensionless constant k , was also computed ($k = 1.08$) to relate the turbulent energy obtained by using the probe in a horizontal position versus the two component turbulent energy using the probe in a vertical position such that

$$k = \frac{u'^2 + v'^2}{u'^2 + w'^2} \quad (4.3)$$

A grid was laid out over a portion of the area expected to scour. The region directly in front of the structure was excluded due to the complexity of the flow direction resulting from horseshoe vortices. The grid is shown in Figures 4.3 and 4.4. In Figure 4.3, the x and y scales are equal. The y scale has been expanded 4.5 times in Figure 4.4. This distorted scale is used to present both hydrodynamic and scour results.

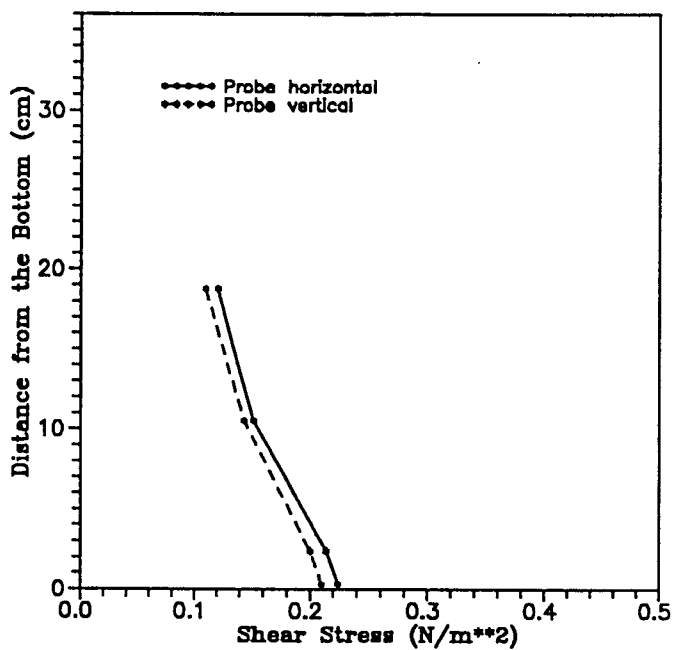


Figure 4.1 Shear stress profiles in front of and away from the influence of the structure at $x = -150.0$ cm and $y = 11.1$ cm.

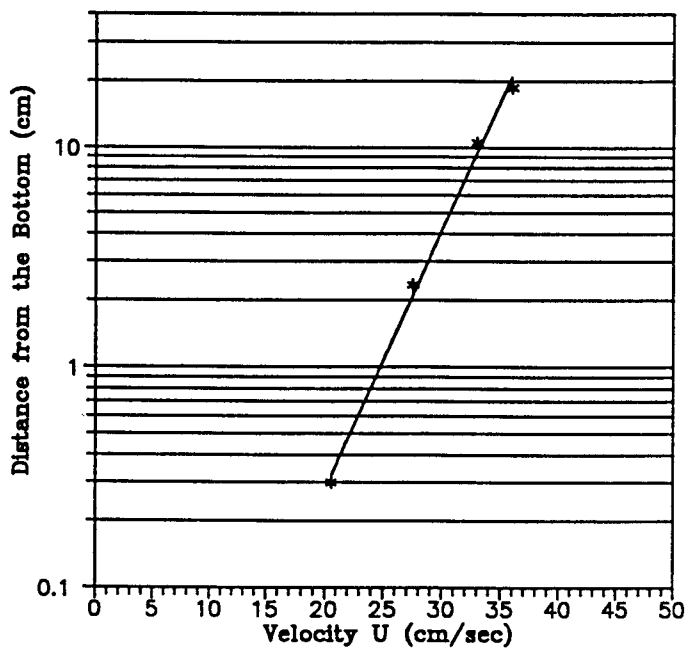


Figure 4.2 Velocity profile corresponding to shear stress profiles in Figure 4.1.

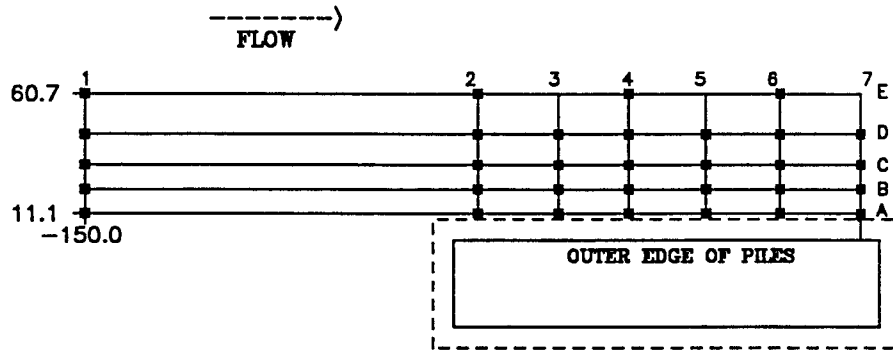


Figure 4.3 Grid points for hydrodynamic study (1:1 scale).

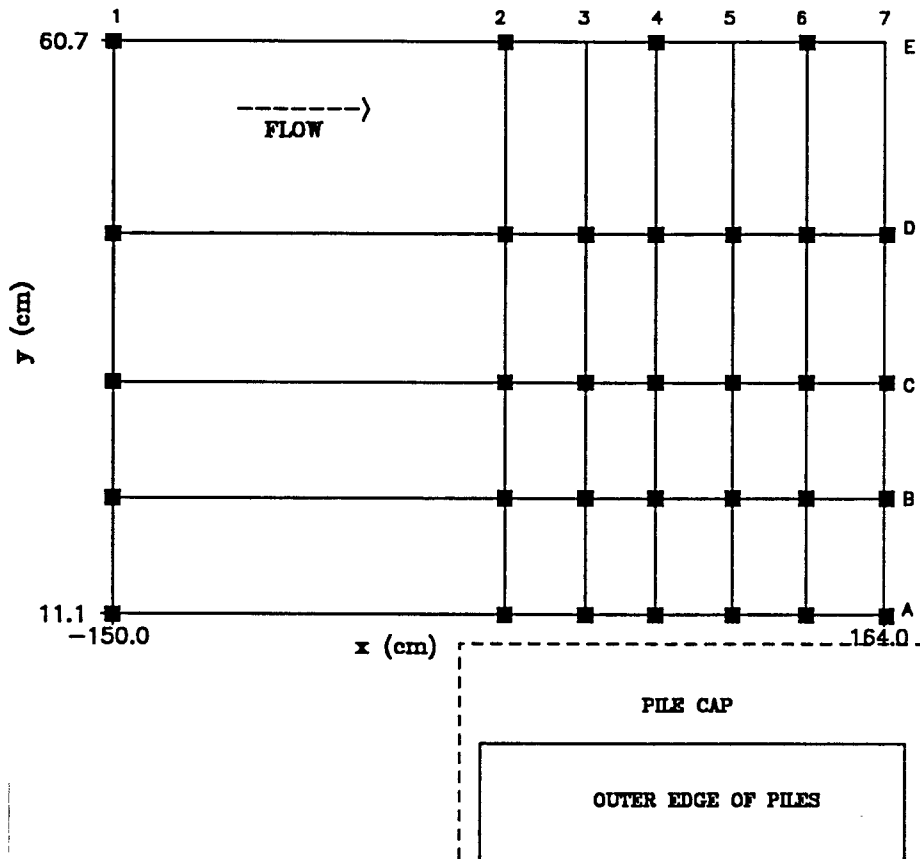


Figure 4.4 Grid points for hydrodynamic study (distorted 1:4.5 scale).

4.2 Experimental Procedures

Prior to conducting the actual tests, the instrumentation had to be set up and calibrated and the structure centered in the test area as shown in Figure 4.5. Figure 4.6 shows the experimental set-up for the hydrodynamic study. Preliminary tests were then conducted in the flume to determine the optimum location to place the model. It was determined that the flow over the V-notch weir had a jetting effect such that the velocity across the tank was not uniform as the flow approached the test area, so a fine mesh screen was constructed and placed directly downstream of the weir. This significantly decreased the jetting effect. A floating wooden lattice was also placed at the entrance of the flume to dampen the waves generated by the weir and a plastic wire mesh wave absorber placed at the downstream tailgate minimized wave reflection. The anemometer measurements were sensitive to water temperature variations so a temperature probe was placed near the anemometer probe as shown in Figure 4.7. The calibration curve for the temperature probe is shown in Figure 4.8. The hydrodynamic tests were conducted at water temperatures ranging from 25 to 29 °C.

The mean flow direction at each grid point had to be determined for each structure configuration. A vane was used to establish the mean flow direction at each grid point. Knowing the mean flow direction, the X sensor probe could be directed in that mean direction to minimize the probe skew angle.

The hydrodynamic tests were conducted at night (starting around midnight) when the air temperature was on the decline, to minimize the change in water temperature during the test. Even with the decline in air temperature, the water temperature increased

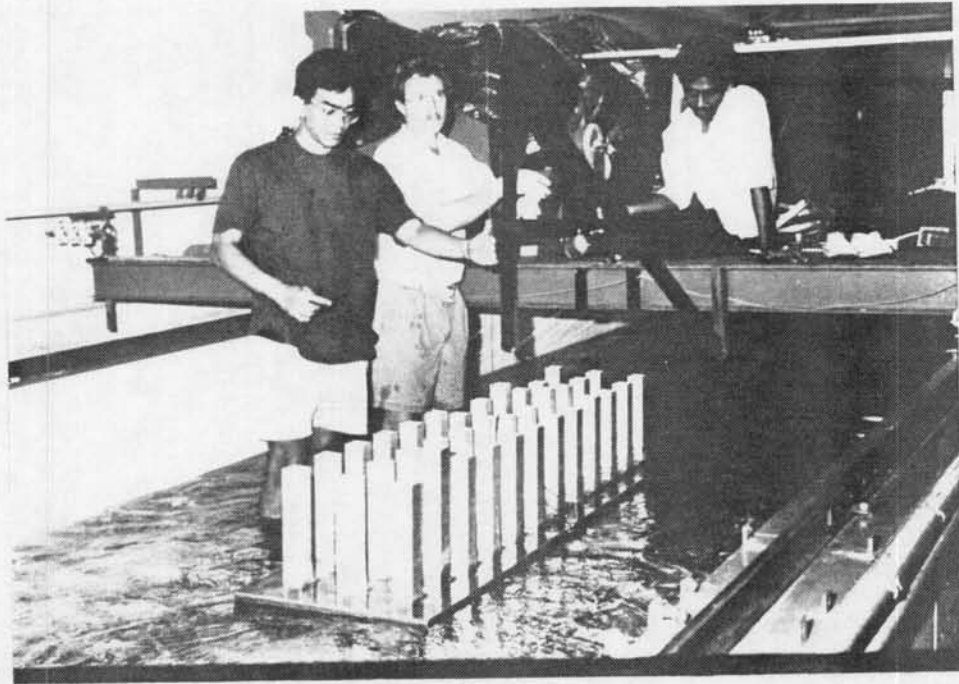


Figure 4.5 Placement of test structure prior to hydrodynamic experiment.

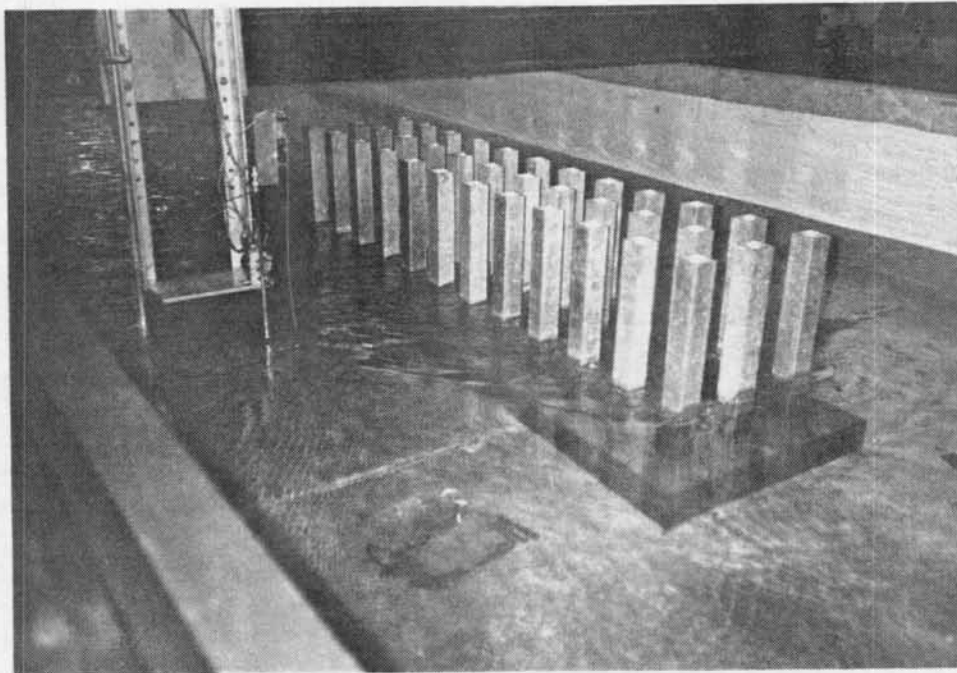


Figure 4.6 Experimental set-up for hydrodynamic study.

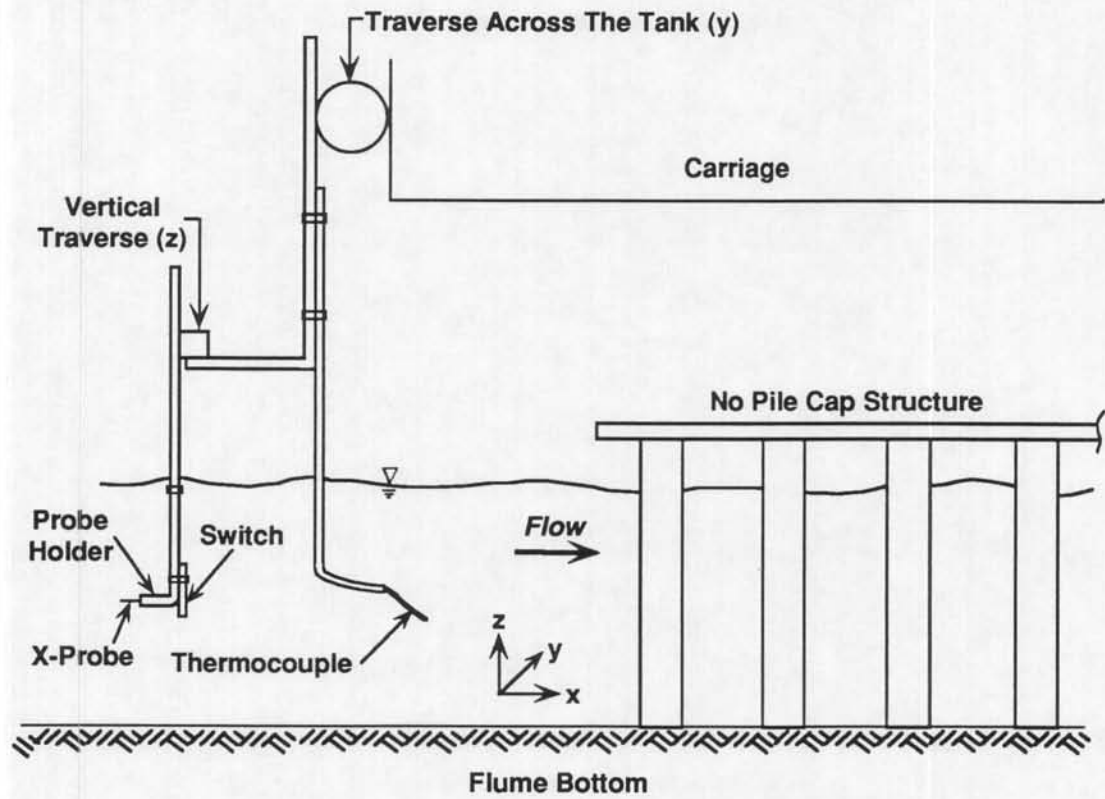


Figure 4.7 Overall set-up of experimental apparatus and instrumentation for hydrodynamic study.

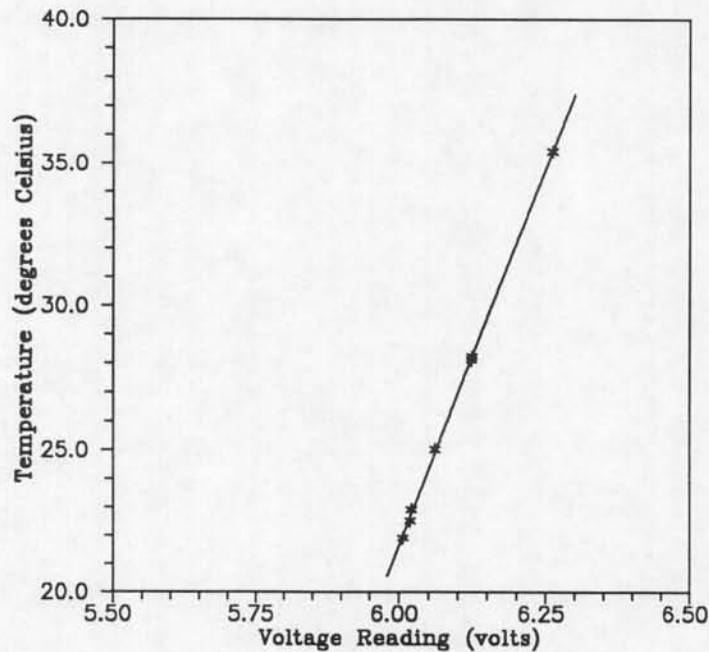


Figure 4.8 Calibration curve for the temperature probe
 $T (^{\circ}\text{C}) = - 445.89 + 102.22V - 4.05V^2$.

at a rate of approximately $0.3^{\circ}\text{C}/\text{hour}$ due to the pump and recirculation. Prior to starting the experiment, the anemometer probe was towed at several velocities through the still water in the flume to obtain a calibration curve for the velocity. A typical velocity versus probe output voltage curve for the X sensor probe is shown in Figure 4.9. After calibration, the pump was started and the flow allowed to stabilize for approximately 45 minutes prior to starting the flow measurements.

The probe was first moved in front of and away from the influence of the structure and the velocity measured at depths ranging from 3 to 187 mm above the bottom. This was used to obtain the undisturbed velocity profile (Figure 4.2). The carriage was then moved along the structure and measurements were taken at the

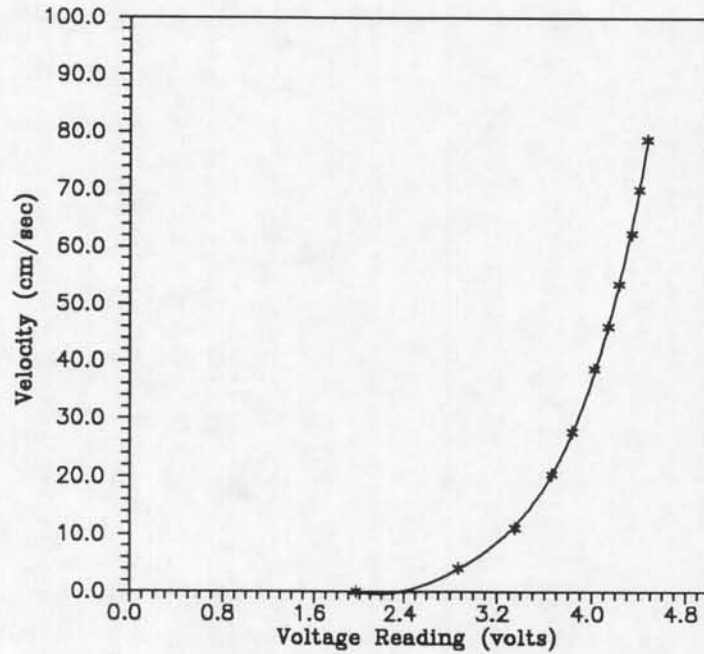


Figure 4.9 Calibration curve for the X sensor probe

$$Vel = -1.86 - 0.33V + 2.05V^2 - 1.01V^3 + 0.15V^4.$$

specified grid points. The grid points are in rows and columns with the rows having constant x and the columns having constant y values. Measurements were made at all grid points in one column prior to moving to the next column, starting with points in front of the structure. Because the temperature in the flume increased at a rate of approximately 0.3 °C/hour, the velocity measurements in front of the structure were used to determine variations in the flow measurements due to changes in the velocity calibration. After completing the measurements at the grid points, the velocities directly behind the structure were measured.

4.3 Data Acquisition

A Metrabyte 16F computer board and ACQWIRE data acquisition software were used to digitize and record the analog signals from the X sensor and temperature probes. Scales were placed along and across the flume and the readings were recorded manually. The vertical position traversing mechanism was controlled by a lap top computer. In addition, a cut off switch attached to the probe support was used for the lowest (3 mm) position (see Figure 4.7). This switch was used to insure that the bottom velocity measurements were made at the same fixed distance above the bed at all locations.

4.3.1 X Sensor Probe

The X sensor probe has 2 perpendicular wires in parallel planes that sense the normal components of the flow in the plane of the wires. The output voltages that are proportional to the velocity components are processed by the ACQWIRE data acquisition software to obtain U (velocity along the tank) and V (velocity across the tank) based on a velocity calibration curve such as that shown in Figure 4.9. Flow and temperature measurements were sampled at a rate of 50 hertz. Due to the change in the average temperature of the water in the flume, the X sensor probe had to be calibrated prior to each set of tests. The two velocity components, U and V can be calculated from the sum and difference of the hot film anemometer output voltages, Volt₁ and Volt₂, as follows:

$$U = \frac{1}{\sqrt{2}} (Volt_1 + Volt_2) \quad (4.4)$$

and

$$V = \frac{1}{\sqrt{2}} (Volt_1 - Volt_2) . \quad (4.5)$$

A typical unfiltered signal is shown in Figure 4.10 and the same signal after filtering is shown in Figure 4.11. Plotted in Figures 4.12 and 4.13 are the power density spectra of U and V for the time series shown in Figures 4.10 and 4.11. The power density spectra of the unfiltered U signal shows a large spike of energy at 10 hertz. This was caused by vortex shedding from the probe holder. Although the noise at 10 hertz for the V signal was not as large as for the U signal, a bandstop, fourth-order Butterworth filter at 10 hertz was applied to both signals.

4.3.2 Temperature Probe

The temperature probe was attached downstream of the X sensor probe to measure the instantaneous temperature fluctuations. Ideally, the temperature probe would be located at the X sensor probe but since the temperature probe was rather large (approximately 4.76 mm in diameter and 101.6 mm long), it was placed far enough downstream so as not to disturb the flow at the X sensor probe. It was located approximately 30.5 cm downstream of the X sensor probe. These water temperature measurements were used in the ACQWIRE data acquisition software to apply a correction to the velocity data after measurement. This correction formula is valid only for small temperature changes and is discussed in Appendix A.

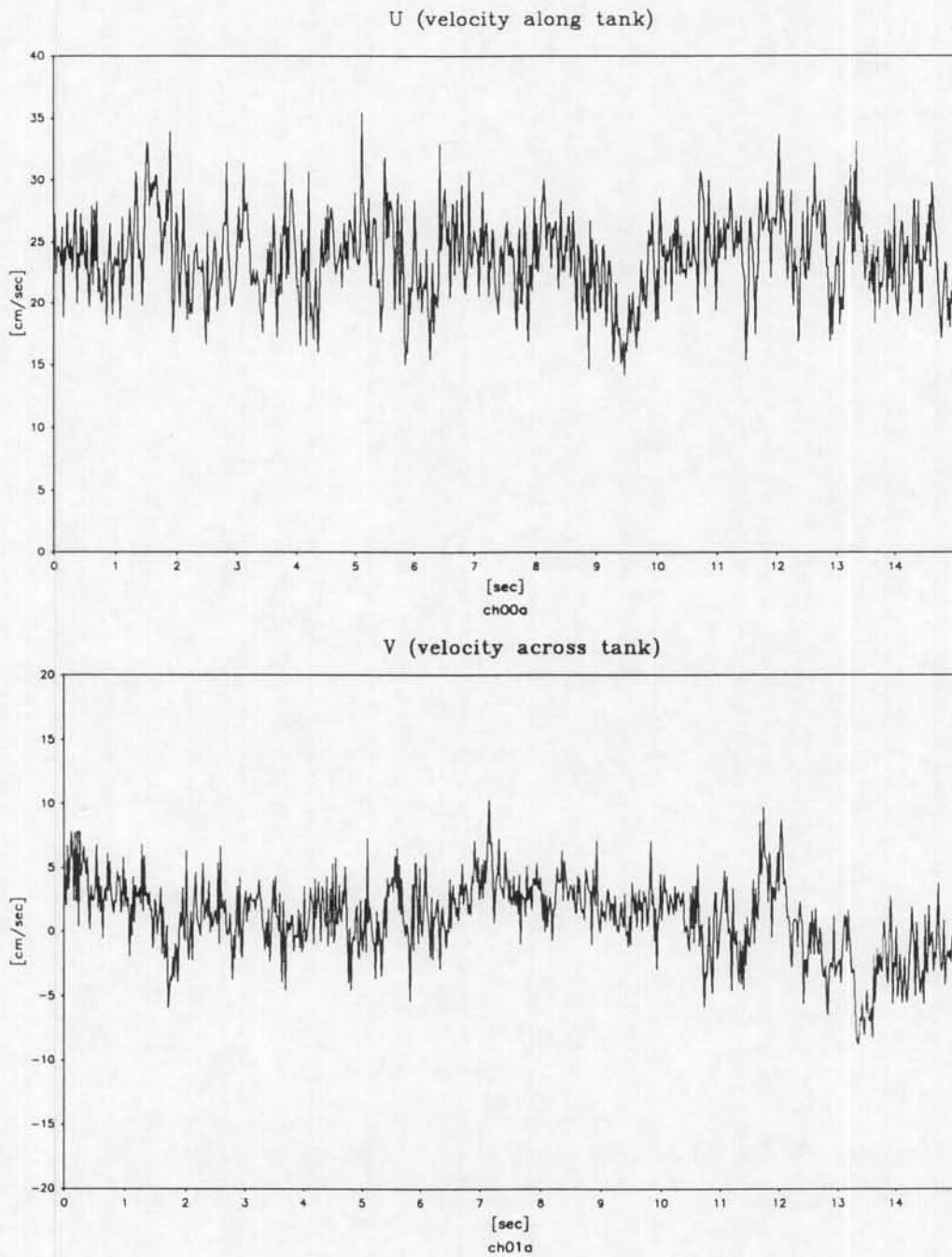


Figure 4.10 Unfiltered U and V velocity components for hydrodynamic Test H-1 at grid point B2.

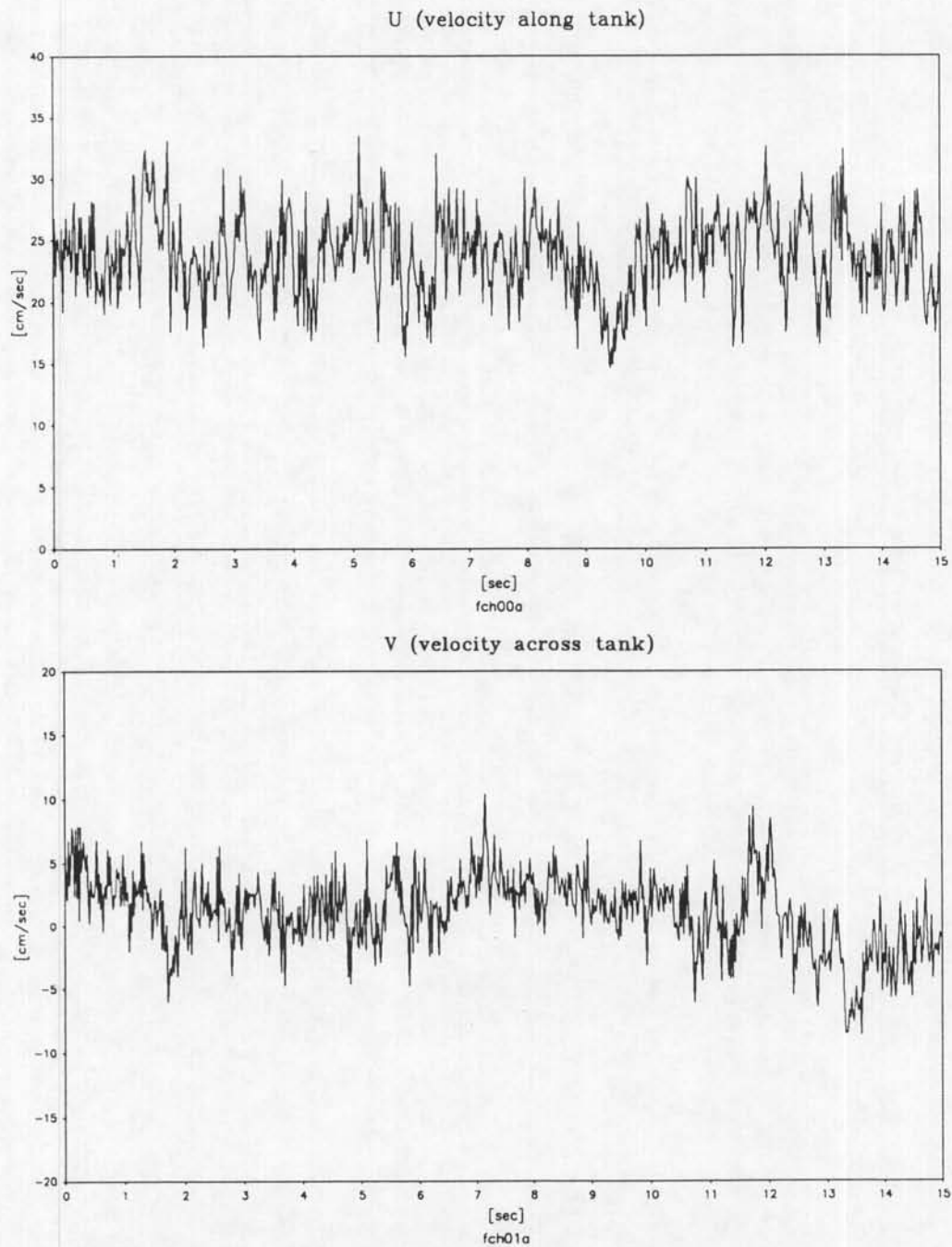
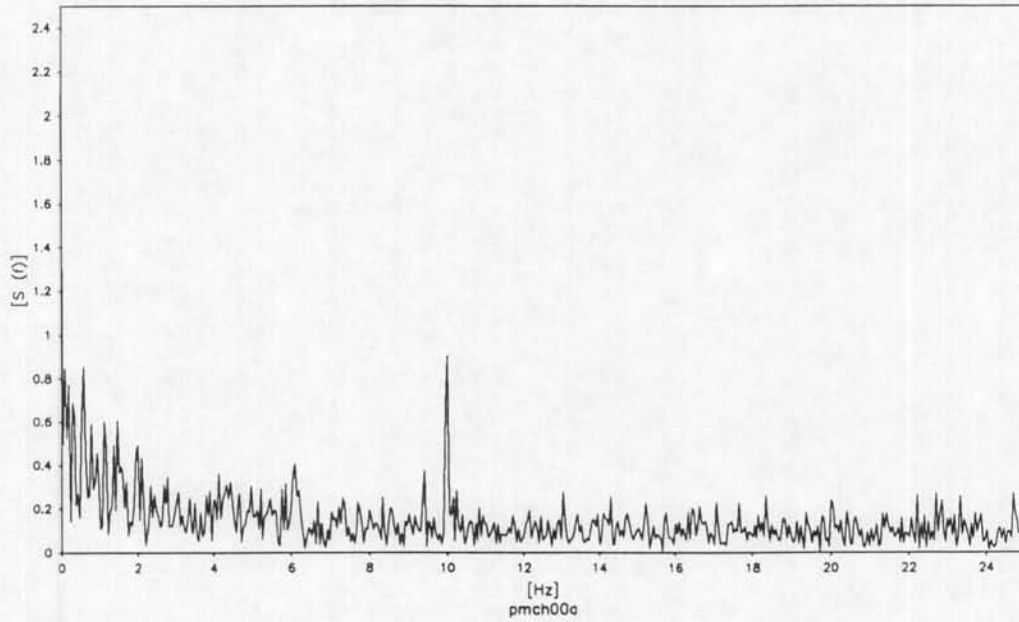


Figure 4.11 Filtered U and V velocity components for hydrodynamic Test H-1 at grid point B2.

Power Density Spectrum of Unfiltered U (velocity along tank)



Power Density Spectrum of Filtered U (velocity along tank)

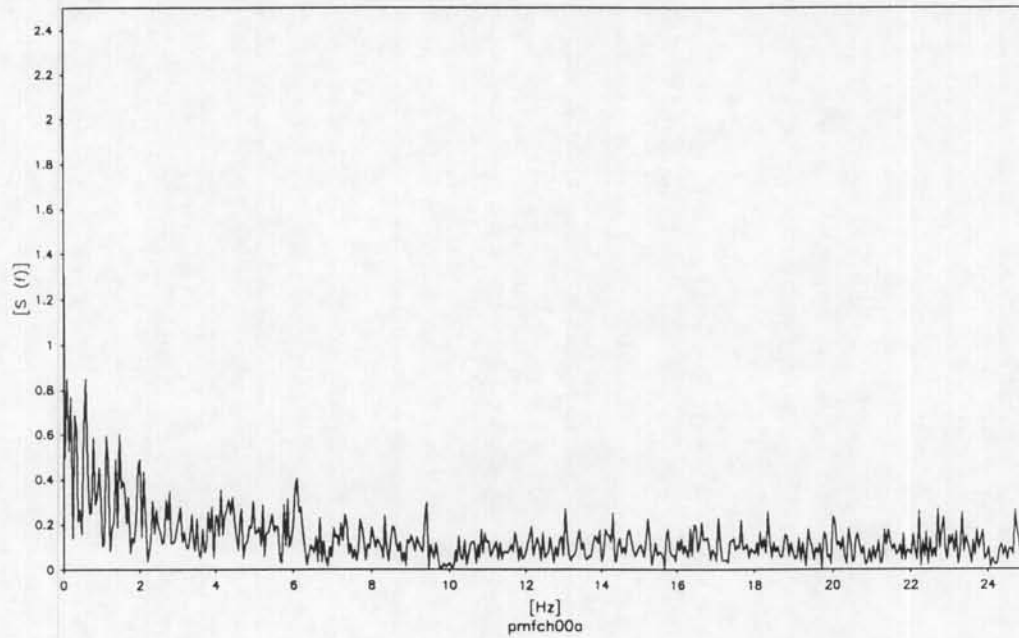
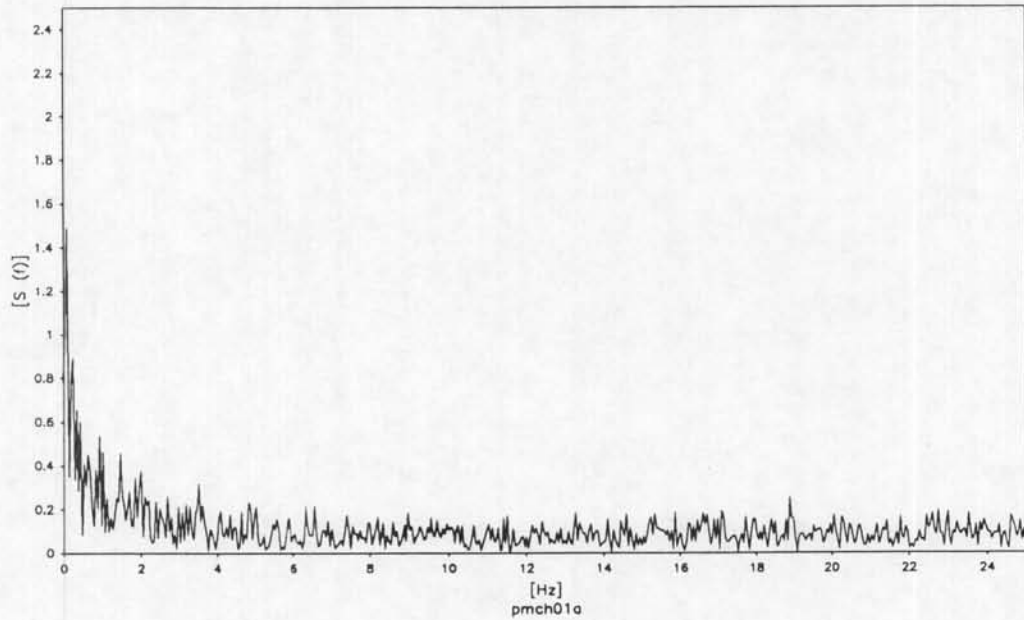


Figure 4.12 Power density spectra of U velocity components in Figures 4.10 and 4.11.

Power Density Spectrum of Unfiltered V (velocity across tank)



Power Density Spectrum of Filtered V (velocity across tank)

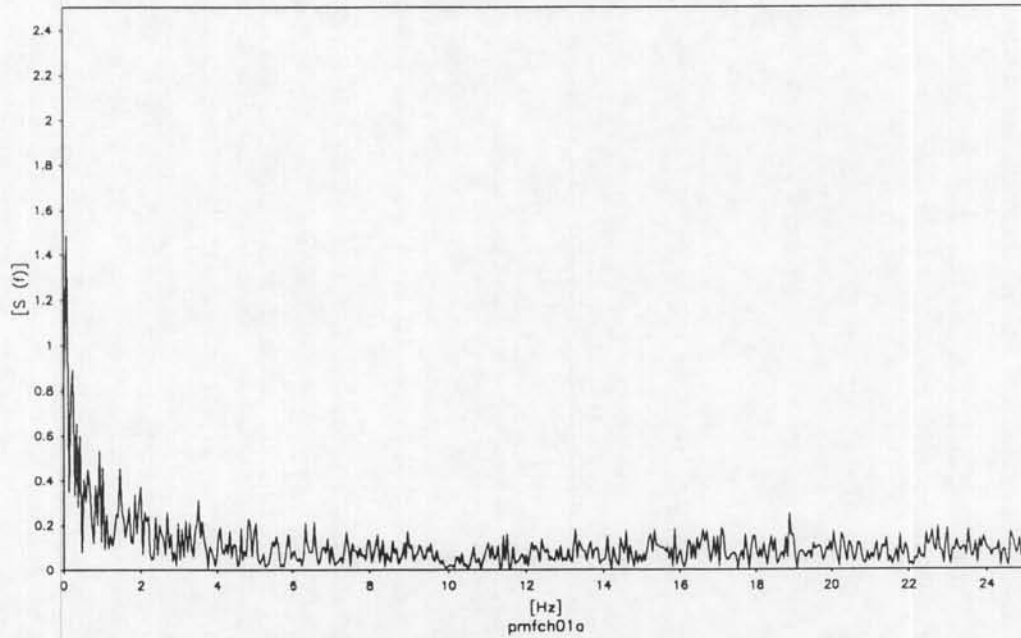


Figure 4.13 Power density spectra of V velocity components in Figures 4.10 and 4.11.

4.4 Data Reduction

In order to compensate for the change in water temperature during the course of the test, curves of the mean velocity and turbulent energy in front of the structure versus time were constructed as shown in Figures 4.14 and 4.15. Since the flow velocity did not vary significantly across the tank, the mean velocity and turbulent energy curves could be applied to the entire test area. This allowed the mean velocity and turbulent energy at each grid point to be non-dimensionalized by the mean velocity and turbulent energy in front of the structure.

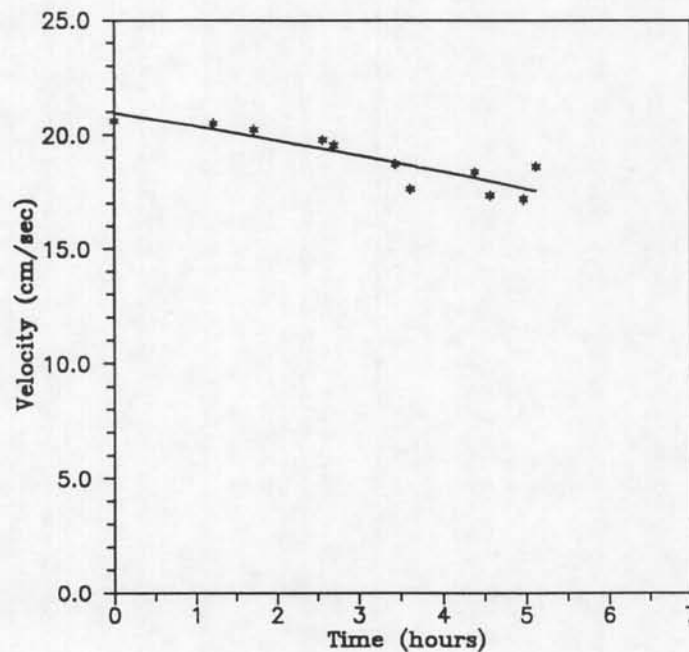


Figure 4.14 Mean velocity in front of structure vs. time
at $x = -150.0$ cm and $z = 3$ mm (test H-1)
 $Vel = 21.551 - 0.863T - 0.150T^2$.

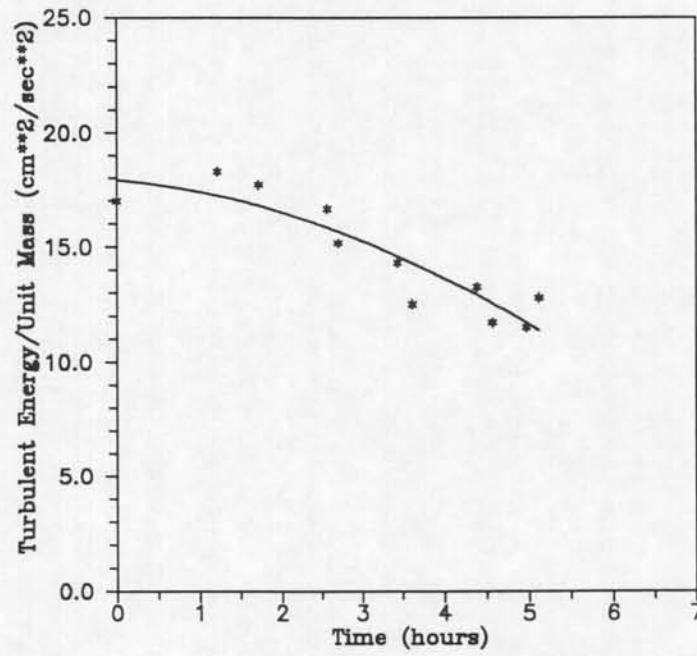


Figure 4.15 Turbulent energy/unit mass in front of structure vs. time
at $x = -150.0$ cm and $z = 3$ mm (Test H-1)
Turb. Energy/Unit Mass = $22.402 - 1.461T - 0.350T^2$.

CHAPTER 5 SCOUR STUDY

5.1 Background

Sediment scour experiments were performed in the same flume and with the same model piers as the hydrodynamic study. The objectives of the scour study were: 1) to provide scour data for calibrating and testing the scour prediction relationship developed as part of the hydrodynamic study and 2) to provide laboratory scour data for multiple pile structures with and without pile caps. Another important aspect of this study was the measurement of the rates of scour.

Instrumentation with the ability to make in situ scour experiments (i.e. measurements of the scour depth as it occurs) were developed. In the past, scour measurements have been very laborious and time consuming. Recent developments in underwater acoustics technology now allow techniques, formerly used only for bottom profiling at prototype depths to be used in the laboratory. The main component of the system used was the Simrad Mesotech 810 echo sounder.

The measurement system that utilizes the Mesotech echo sounder was developed, constructed and tested in the Coastal Engineering Laboratory at the University of Florida. An acoustic pulse sent by the echo sounder reflects off the bottom and the return pulse is sensed by the echo sounder. The time required for the signal to travel to and from the bottom is measured and the distance computed. Returns from particles in suspension also

show up in the signal and must be dealt with as noise. A schematic drawing of the system is shown in Figure 5.1. The bowl which sits just below the surface of the water when measurements are being made serves to minimize the disturbance to the flow (see Figure 5.2).

To allow the echo sounder to send acoustic signals to the bottom, a small window was cut out of the bowl and a vinyl sheet glued over the slot. The acoustic reflection from the vinyl sheet was minimal. The level of water in the bowl was such that the sounder head was always submerged.

The echo sounder was mounted on a frame as shown in Figure 5.1 and a motor was used to rotate the echo sounder and thus the beam towards and away from the structure. The entire depth measuring system was mounted on a carriage that traversed the width of the flume. A small wheel in a track attached to a potentiometer was used to measure the position across the flume and a similar arrangement was used to measure the position of the carriage along the flume. Scales placed along and across the flume were used to calibrate the position potentiometers. The start and ending points for each traverse was recorded in the log book. A data reduction program was then used to transform the output from the echo sounder signal and the position potentiometers to xyz coordinates.

5.2 Sediment

The metal plates covering the recess in the flume were removed and the multiple pile structure was centered in the test area. Sand was then placed around the structure as shown in Figure 5.3. Three different sediment sizes were used in the flume. The

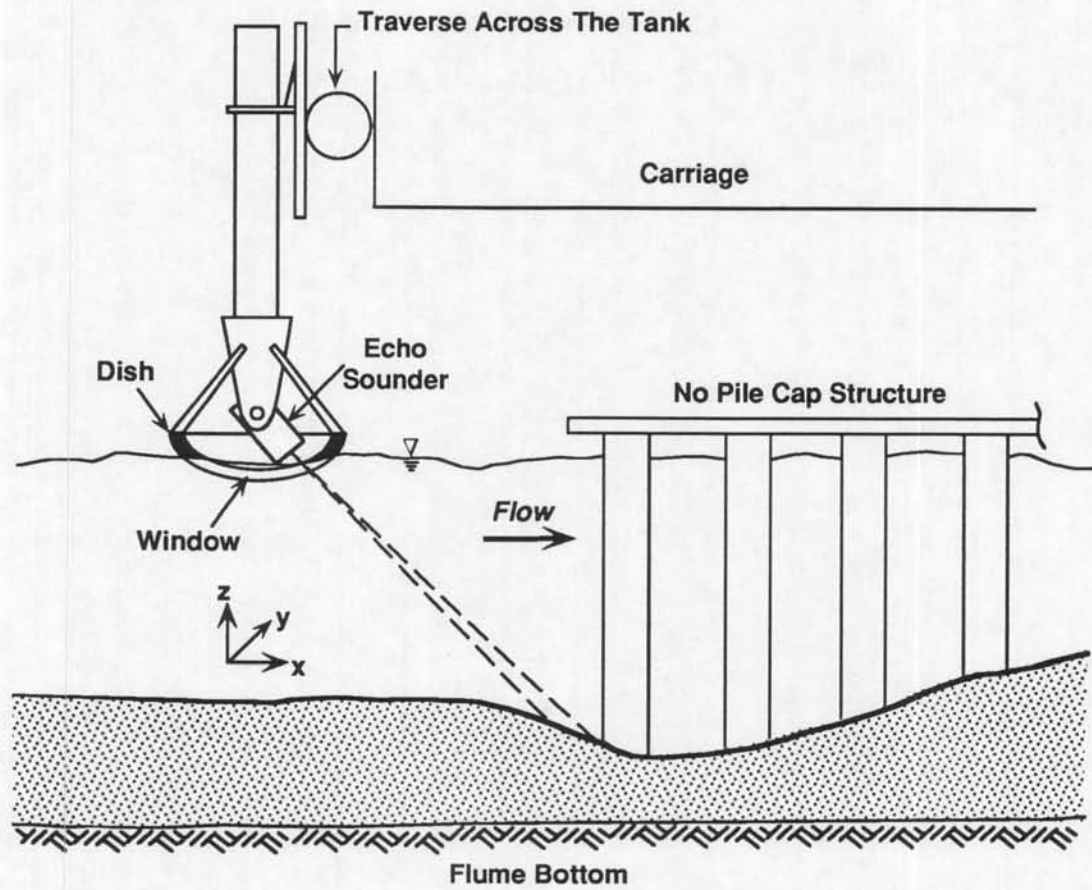


Figure 5.1 Overall set-up of experimental apparatus and instrumentation for scour study.

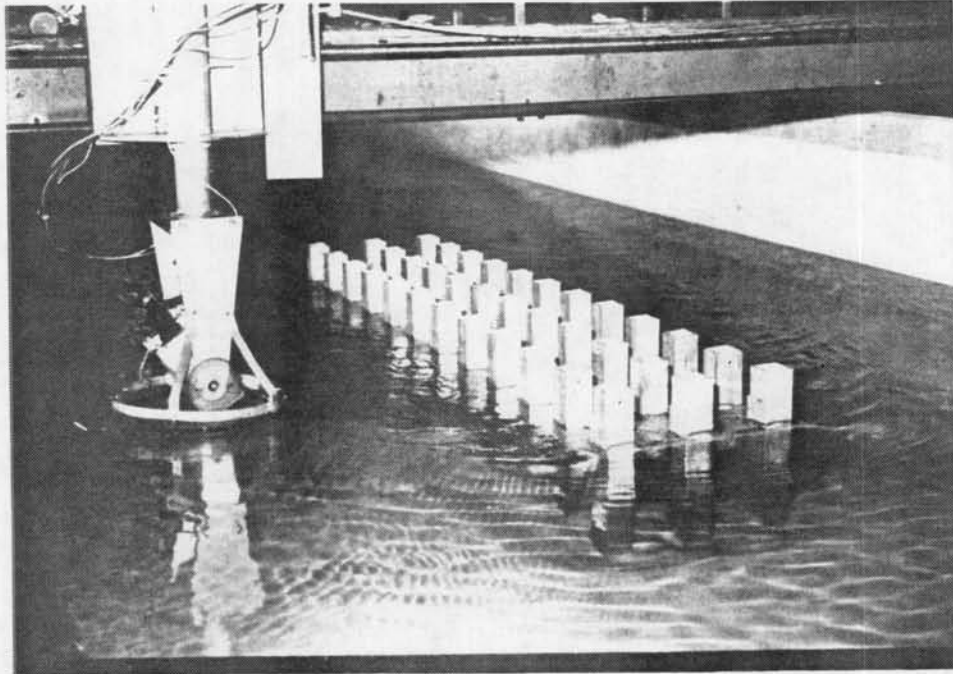


Figure 5.2 Experimental set-up for scour study.

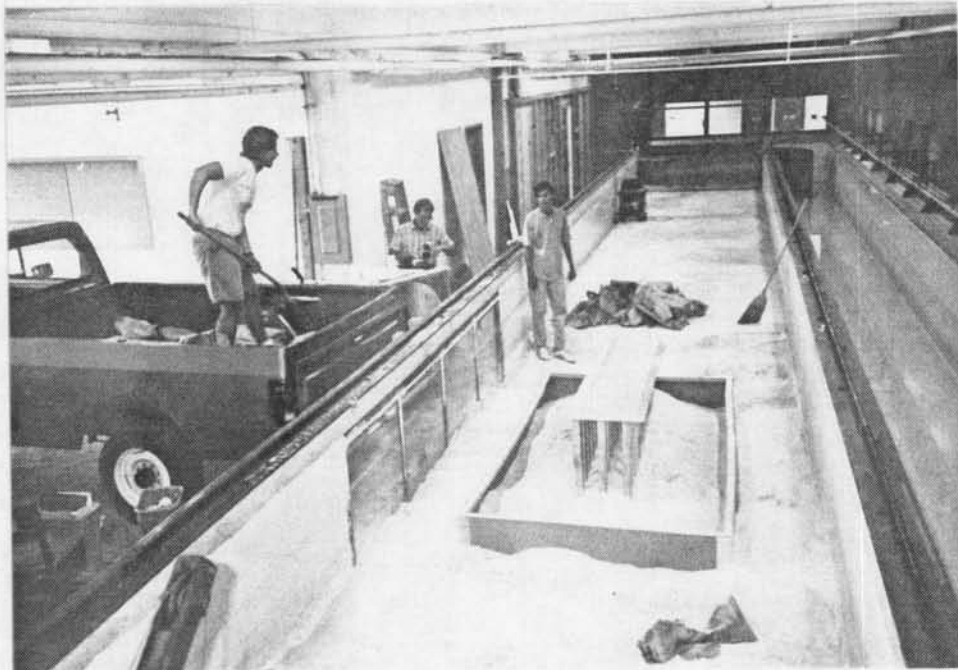


Figure 5.3 Test area of flume showing no pile cap structure and central region near structure.

largest quantity of sand (Category 1) was placed in the regions of the test area where no scour was anticipated. This category had sediment sizes ranging from 0.2 to 0.8 mm. Category 2 consisted of sand that was used to anchor the sand in the first category and had a range of sediment sizes from 0.84 to 2.00 mm. This minimized the amount of fine sand transported down the flume and through the pump. The third category of sand was placed in the region around the structure where scour was anticipated. This category had sediment sizes ranging from 0.42 to 0.84 mm and a median grain size, d_{50} , of 0.60 mm.

5.3 Instrumentation

Before the scour experiments were started, the instrumentation had to be set up and calibrated. The acoustic bed profiling system is based upon the use of an echo sounder operating at 2.25 Mhz. The 2.25 Mhz operating frequency was chosen to give reasonable accuracies at short ranges, as well as to ensure sufficient energy in the reflection from the bed. A 10 μ sec pulse is emitted at a 100 Hz rate. The returned pulse is an analog time/amplitude history of the water column. The travel time of the signal is proportional to the distance to a reflecting object. The amplitude of the pulse at any point in time is a measure of the number, size and density of reflecting particles in the water column. The acoustic signal from the echo sounder was calibrated by positioning a flat metal plate at different elevations below the sounder and the output recorded. A calibration curve for the echo sounder output is given in Figure 5.4.

The angle the echo sounder head makes with the vertical was measured using a ten turn precision potentiometer. A protractor mounted on the side of the unit was used

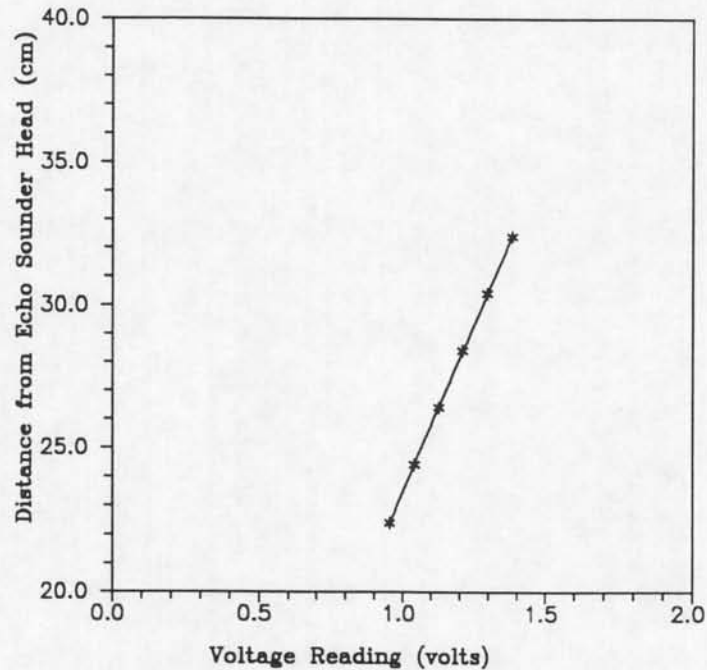


Figure 5.4 Calibration curve for the echo sounder output signal
 $\text{Distance (cm)} = 0.112 + 23.385V$.

in the calibration process. The head was rotated to various angles and the output voltage from the potentiometer recorded. Because of some play in the gears moving the sounder head, a lag between the actual angle and the angle measured was observed. To compensate for this, a lag was added or subtracted from the calibration curve depending on the direction the sounder head was swinging. A plot of the modified calibration curve used is shown in Figure 5.5 along with the actual readings during the calibration process. More details on this subject are given in Appendix B.

5.4 Test Procedures

Prior to each scour test, the sand was compacted with a tamper, smoothed and leveled. After the bottom was leveled, the flume was slowly filled with water to prevent scour during the fill process. Before starting the flow, the bottom was mapped with the

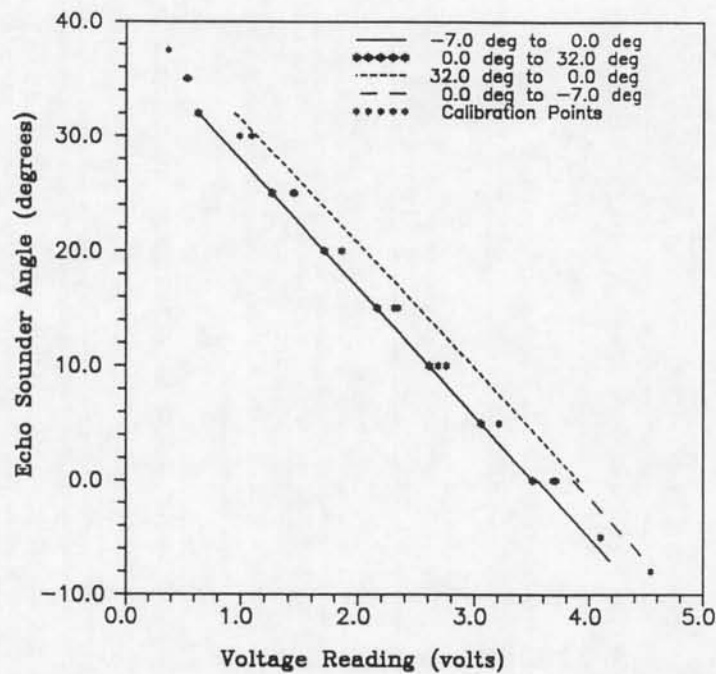


Figure 5.5 Modified calibration curve for echo sounder angle.

echo sounder. This allowed the scour measurements to be compared with the original bottom. After the pump was started, minor flow adjustments had to be made during the first 30 minutes of the test to obtain the desired velocities. Mapping of the bottom began a few minutes after the pump was started and this continued throughout the duration of the test (~ 28 hours). The interval between the scans increased as the rate of scour decreased (from ~ 10 minutes at the start to ~ 90 minutes at the end). After the flow was stopped, the bottom was mapped once more. The water was then drained from the flume and test area and point gauge measurements of the bottom were made.

A local maximum (if not the absolute maximum) in structure-induced scour occurs near the transition from clearwater to live bed conditions. For this reason, the scour (and hydrodynamic) tests were performed just below transition conditions. This was also

done to minimize the amount of suspended sediment transported through the pump. As a result, the amount of sand in suspension was small except immediately adjacent to the piles.

After the scour tests on the multiple pile structures were completed, a decision to conduct two additional experiments was made. These two tests were for a 4 inch cylinder under the same sediment, water depth and flow conditions ($\bar{U} = 0.31$ m/sec) and at an increased flow rate ($\bar{U} = 0.37$ m/sec). The purpose of these tests were to determine if the conditions of the multiple pile tests were close enough to transition (clear water to live bed) that maximum scour was occurring. The first cylinder test (conducted at $\bar{U} = 0.31$ m/sec) produced an ultimate scour depth ratio (d_e/D) of 1.68. The second cylinder test (conducted at $\bar{U} = 0.37$ m/sec) produced an ultimate scour depth ratio of 1.91, 14% larger than that of the first test. The dimensionless scour ratio of 1.91 matches the value obtained by Hannah (1978) for single circular cylinder. This indicates that the flow rates for the pier tests were a bit low. Sand ripples formed away from the structure and sand was transported down the flume for every test conducted indicating a live bed condition, at least for a portion of the sand grains. However, more ripples formed and more sand was transported during the second test with the cylinder were closer to transition for the d_{50} (0.60 mm) sediment. To determine if the 14% increase in scour depths found for the single cylinder could be applied to the multiple pile structure, an additional test was made on the structure with no pile cap at the higher flow rate. As with the cylinder, the scour depth increased approximately 14%. There was some contraction scour during this test making these measurements not as precise as for

the other tests. Thus, it seems appropriate to apply a scour depth correction to the multiple pile test conducted at the lower rate.

Section 5.7 shows that the scour depths are not close to equilibrium except for the first few rows of the structure. At 28 hours, the scour depths at these front rows are approaching equilibrium. Ettema (1976) found that the scour depths at 24 hours are 90% of the equilibrium scour depths. Because of this the scour depth correction and the equilibrium correction is only applied to the front of the structure such that

$$de_e = de_m \frac{1.14}{0.9} \quad (5.1)$$

where

- de_e = estimated equilibrium scour depth and
 de_m = measured scour depth after 28 hours.

5.5 Data Acquisition

A Data Translation DT2801 computer board and GLOBAL LAB data acquisition software were used to digitize and record the analog signals from the echo sounder output and the potentiometer readings at a sampling frequency of 40 hertz.

5.5.1 Echo Sounder

Noise in the acoustic data (Channel CH00) came from reflections from the pile cap and/or piles and suspended sediment. Since the main mechanism for sediment movement was bed load transport, the noise caused by suspended sediment was minimal. The output from the echo sounder was filtered using a lowpass, sixth-order Butterworth

filter with a cutoff frequency of 3 hertz. A plot of the echo sounder output signal before filtering is shown in Figure 5.6. Figure 5.7 shows the same signal after filtering and power spectra for both signals are shown in Figure 5.8.

5.5.2 Potentiometer Readings

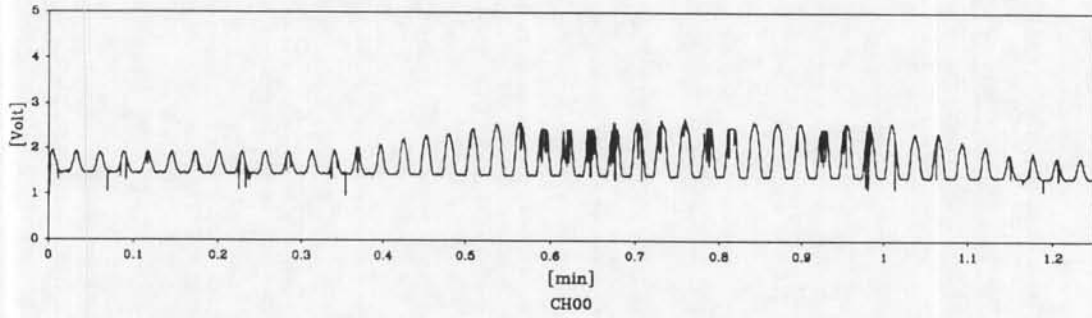
Channel CH01 recorded the output from the potentiometer measuring the position along the flume (x direction) while Channel CH03 was used for the position of the carriage across the flume (y direction). Both output signals were filtered using lowpass, sixth-order Butterworth filters with a cutoff frequency of 0.5 hertz. The noise in Channel CH03 was caused by sudden movements of the manually operated traverse across the flume. The carriage was moved along the flume with a variable speed motor at a slow speed (approximately 2 cm/sec). The smooth motion along the flume minimized the noise in Channel CH01. Figure 5.9 compares the power density spectra of Channel CH03 before and after filtering. As mentioned before, the start and end points of the x and y traverses were recorded in the log book.

The echo sounder angle signal was recorded on Channel CH02 and was filtered using a lowpass, second-order Butterworth filter with a cutoff frequency of 20 hertz. The sounder head was designed to swing from -9° to 35° but only data converted in the range from -7° to 32° were used because of reflection and attenuation of the echo sounder signal at the ends of the swing.

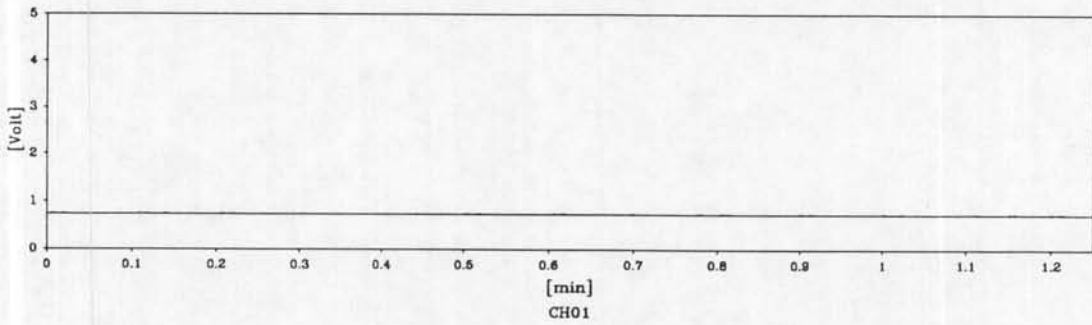
5.6 Data Reduction

A data reduction program was written to convert sediment scour data obtained from the echo sounder and position potentiometers to bottom coordinates in rectangular

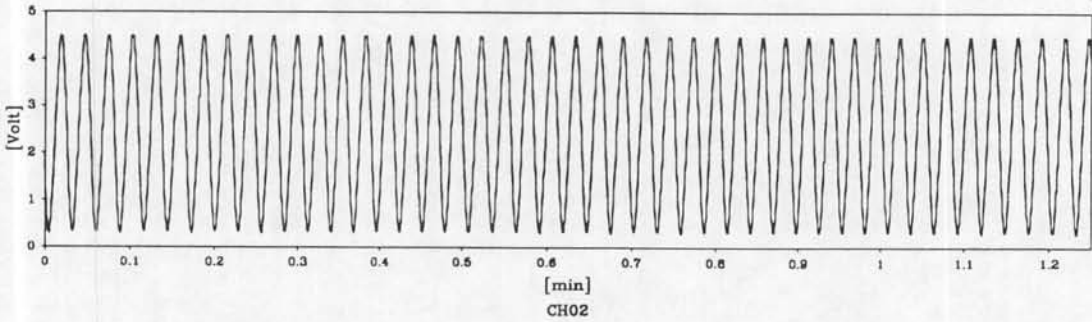
Echo Sounder Output



Position Along Tank



Echo Sounder Angle



Position Across Tank

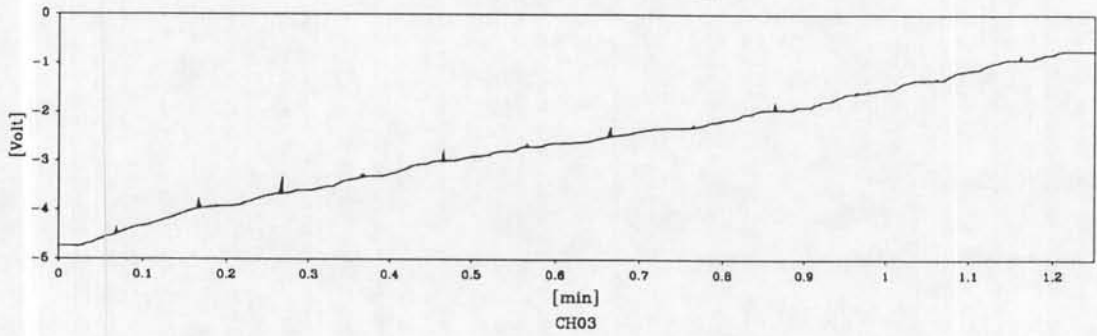
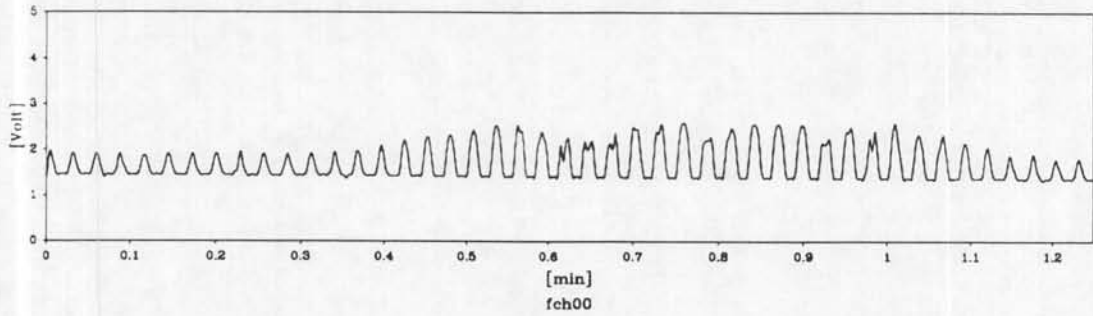
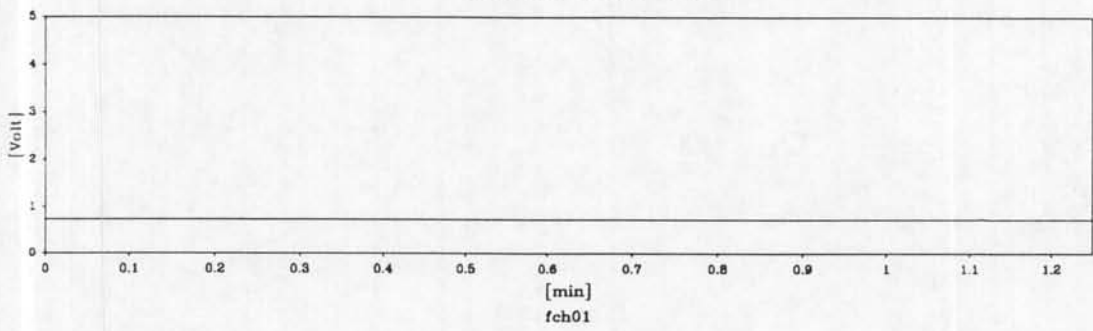


Figure 5.6 Unfiltered output signals after completion of Test S-1.

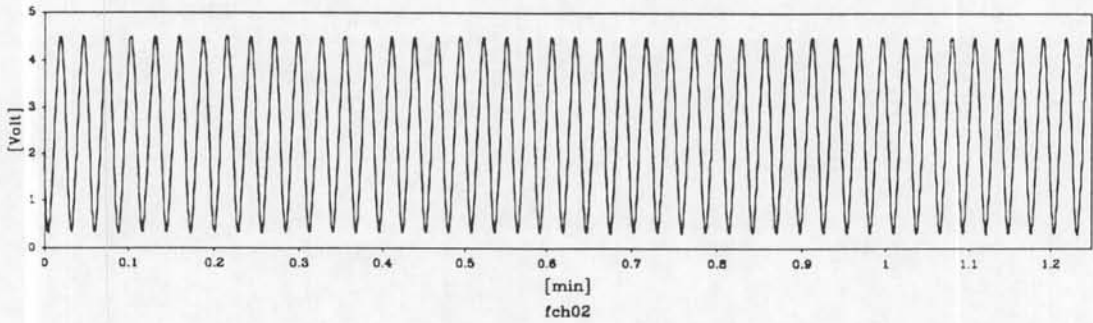
Echo Sounder Output



Position Along Tank



Echo Sounder Angle



Position Across Tank

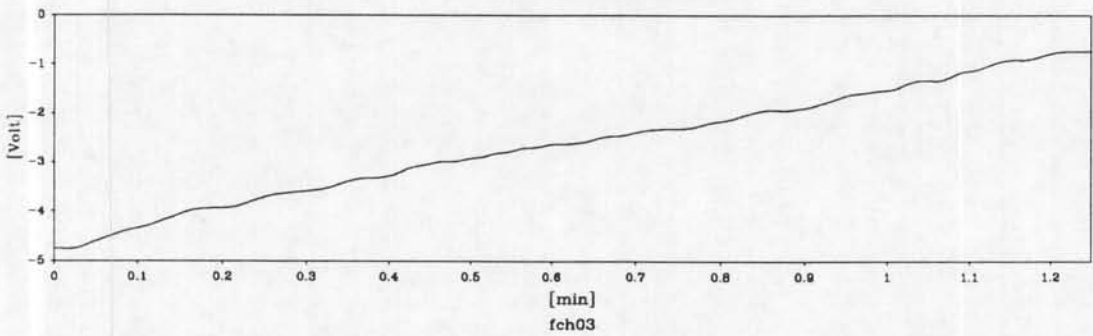


Figure 5.7 Filtered output signals after completion of Test S-1.

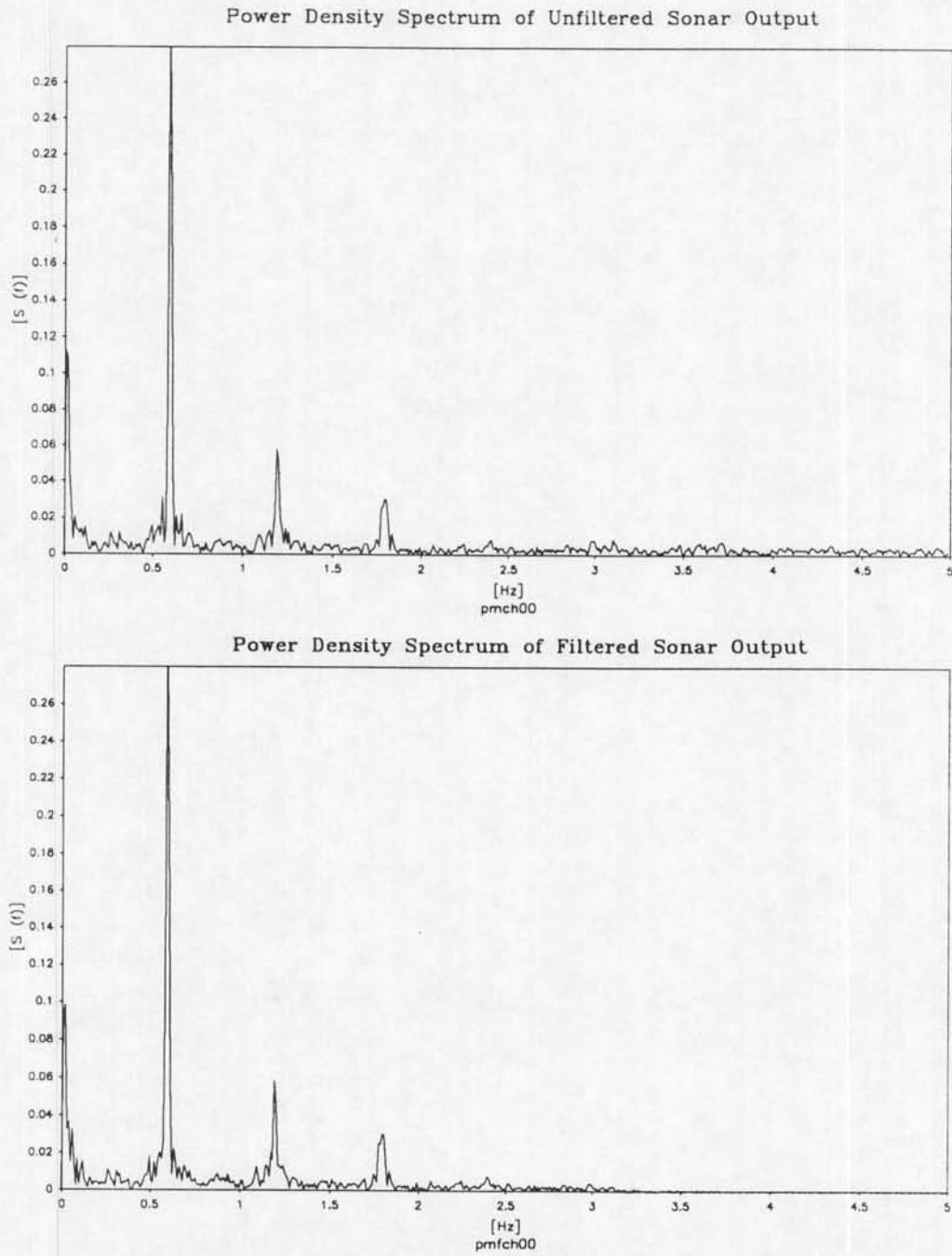


Figure 5.8 Power density spectra of echo sounder output (Channel CH00) in Figures 5.6 and 5.7.

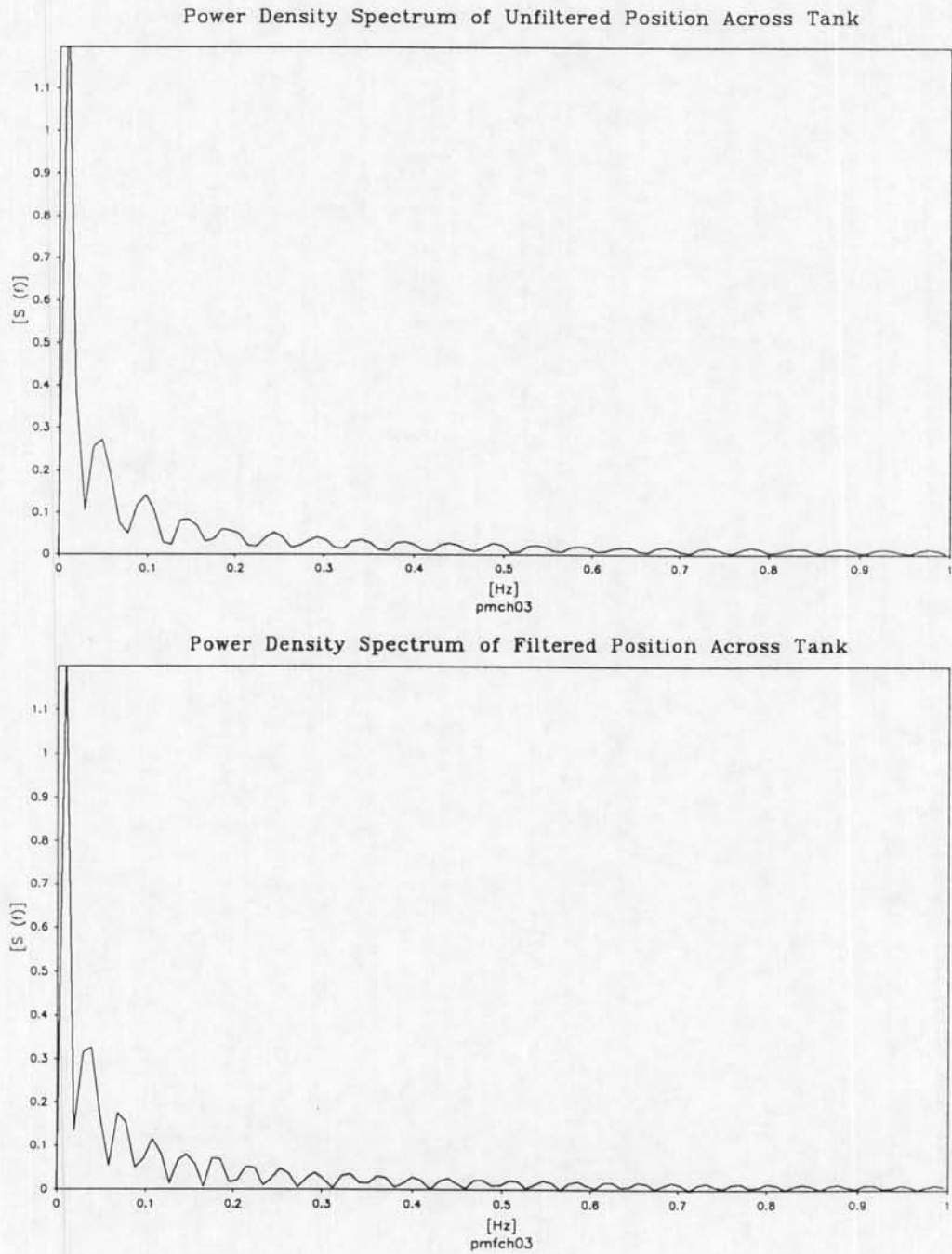


Figure 5.9 Power density spectra of y position potentiometer (Channel CH03) in Figures 5.6 and 5.7.

coordinates (x,y and z). The raw data consisted of 1) voltage proportional to the distance from the echo sounder head to the bottom, 2) voltage proportional to the position of the depth measuring system along the tank (x position), 3) voltage proportional to the angle of inclination of the sounder head (measured from a vertical line with the angle varying from -7° to 32°) and 4) voltage proportional to the position of the depth measuring system across the tank (y position). A detailed explanation of the data reduction process is given in Appendix B. Figure 5.10 is a definition sketch of the measurements needed to convert the raw data to x-y coordinates. The equations used are

$$z = (R + R_o) \cos \Theta - z_o \text{ and}$$

$$d = (R + R_o) \sin \Theta,$$

where

$$R = \text{distance from echo sounder face to bottom,}$$

$$d = \text{radial distance from echo sounder to bottom measurement,}$$

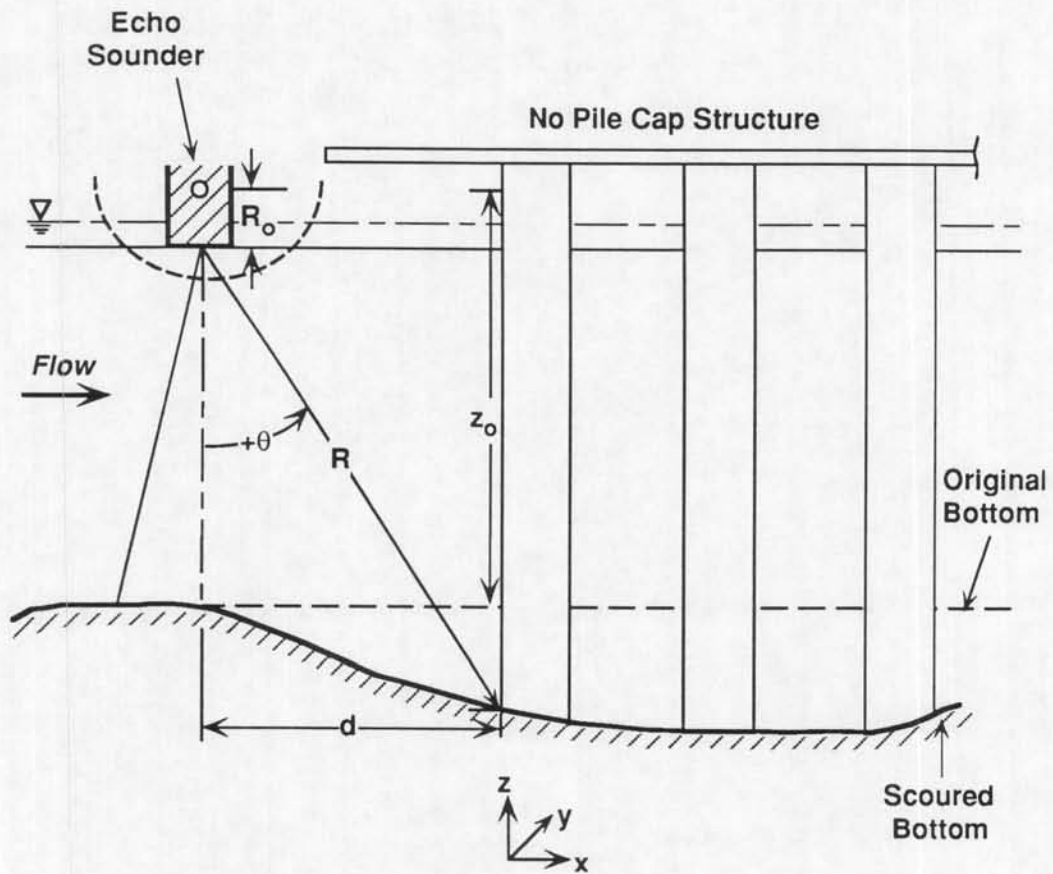
$$z_o = \text{vertical distance from echo sounder pivot to original bottom,}$$

$$R_o = \text{distance from echo sounder pivot to its face and}$$

$$\Theta = \text{angle of echo sounder with vertical axis,}$$

$$(-7^\circ \text{ to } +32^\circ).$$

After the data reduction process, the data were gridded using the surface fit program, SURFER, which was used to interpolate and map the bottom. Figure 5.11 shows the data points used to map out the bottom prior to the test while Figure 5.12 is



The origin of the right hand coordinate system is located at the original bottom on the front outer corner of pile C1.

Positive x is in the direction of flow, *Positive z* is upward and *Positive y* is normal to the flow.

Figure 5.10 Definition sketch showing measurements needed for conversion of raw data to x-y coordinates

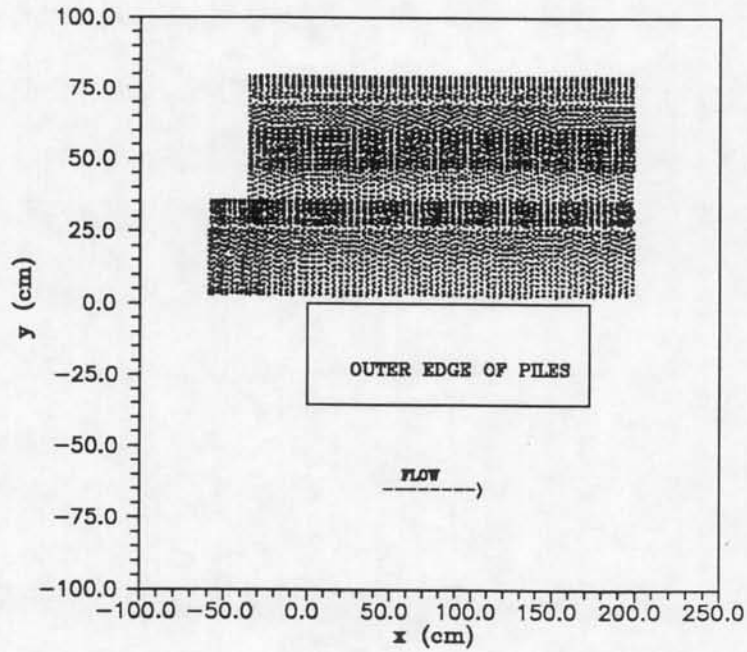


Figure 5.11 Data points before start of scour Test S-1 (No pile cap structure).

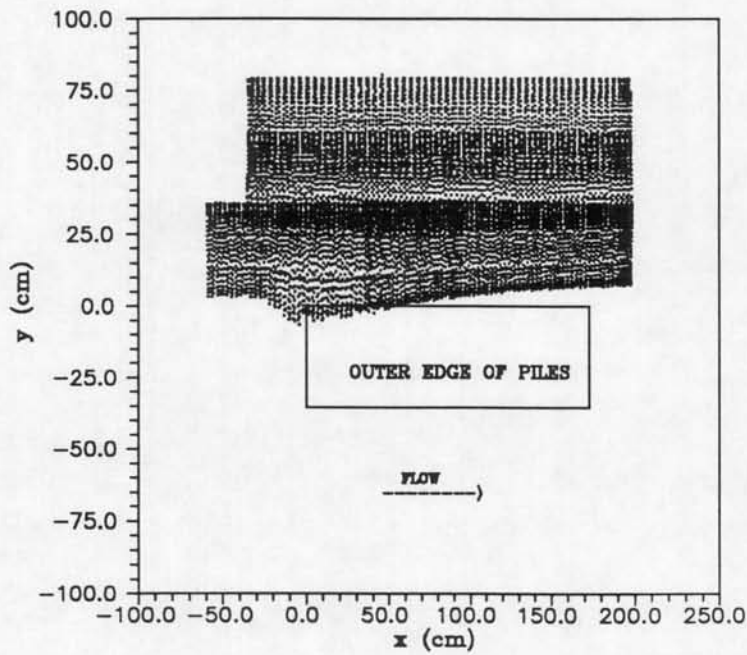


Figure 5.12 Data points after completion of scour Test S-1 (No pile cap structure).

a plot of the data points after the test was completed. The number of data points used to map the bottom was approximately 9,000.

5.7 Time Rate of Scour

Since these experiments were conducted under clear water scour conditions, the scour hole development could be observed visually. As soon as the flow was started, sediment along the structure was put into motion. Due to the clear water scour conditions, there was very little sediment being transported into the control volume surrounding the front row of piles, thus the rate of erosion in this region is large. Further downstream in the structure, there was initially (and for some time) more sediment being transported into the region than was being scoured, thus accretion occurred. Accretion continued until the transport into the region fell below the scour rate. The sediment transport processes were more rapid at first but decreased with time making it very difficult to judge the "maturity" of the scour hole strictly by observation.

Plots of the scour depths versus time at different locations along the structure were, however, very informative (see Figures 5.13 and 5.14). From these figures, it is evident that the local scour depths at rows 1 and 2 were approaching equilibrium after 28 hours. On the other hand, a net scour at the piles in row 6 was just beginning 25 hours into the flow. Figures 5.14 to 5.17 compare the time rate of scour of piles 1, 2 and 6 for the no pile cap structure and the 70° pile cap (top position) structure.

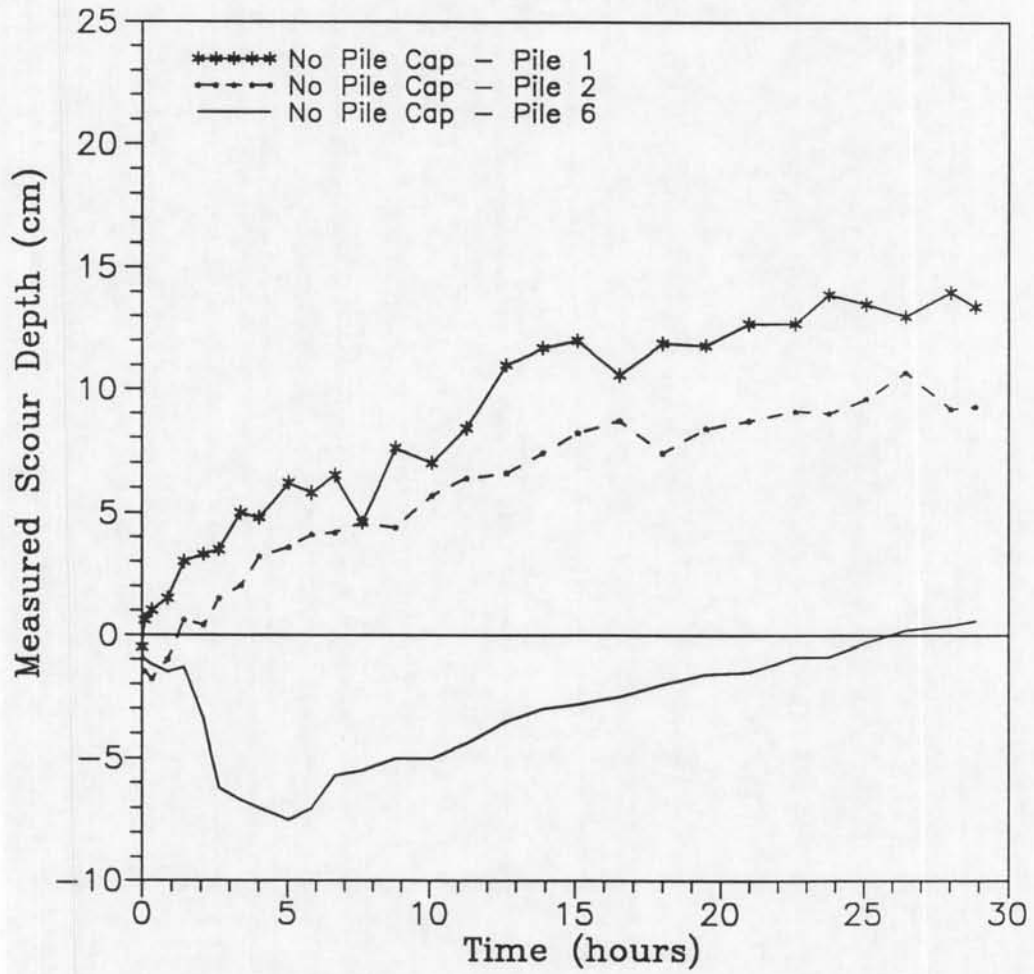


Figure 5.13 Time rate of scour of piles 1,2 and 6 of no pile cap structure.

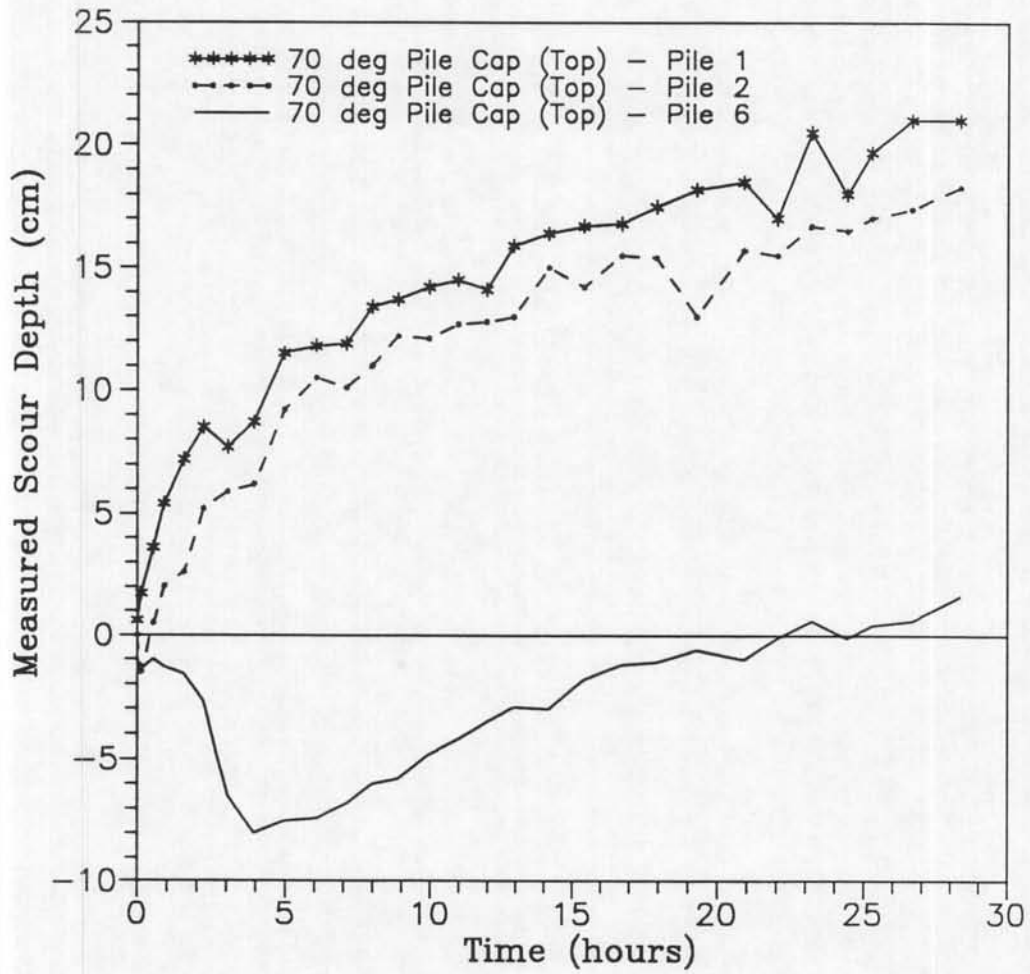


Figure 5.14 Time rate of scour of piles 1,2 and 6 of 70° pile cap (top position) structure.

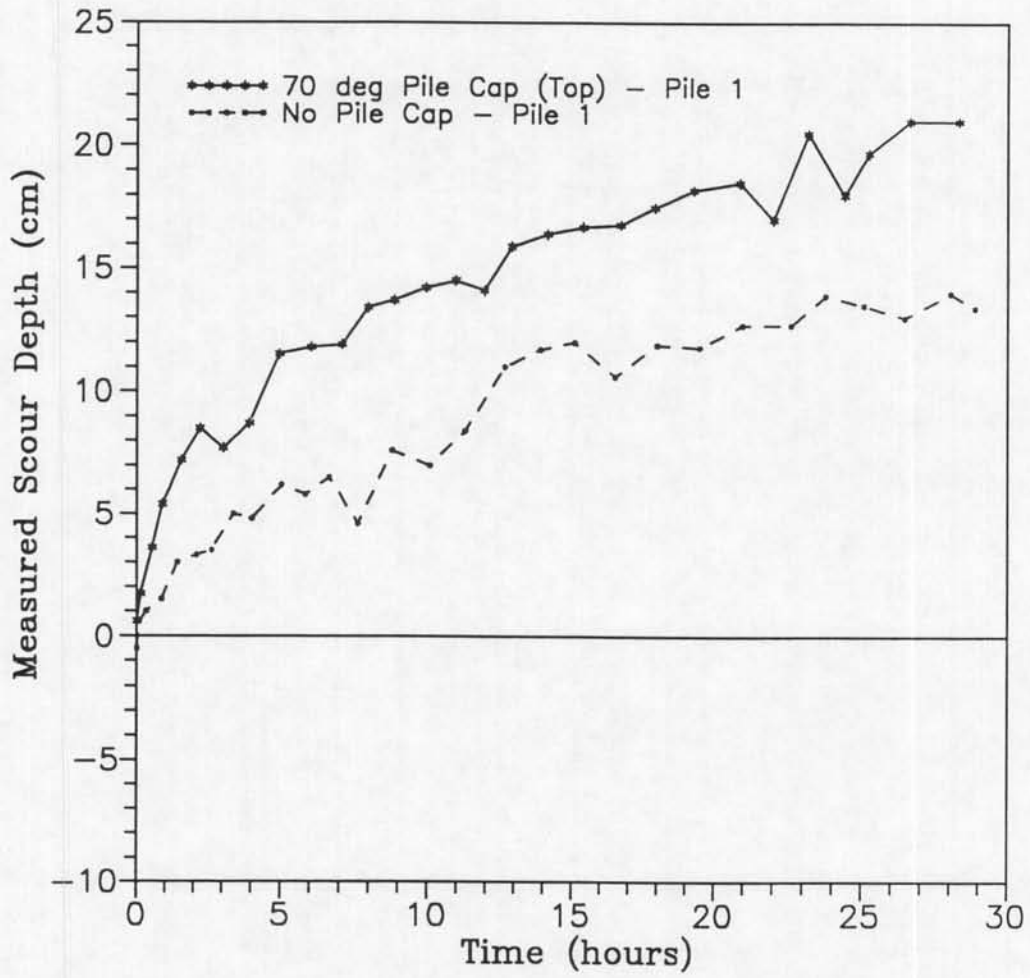


Figure 5.15 Time rate of scour of pile 1.

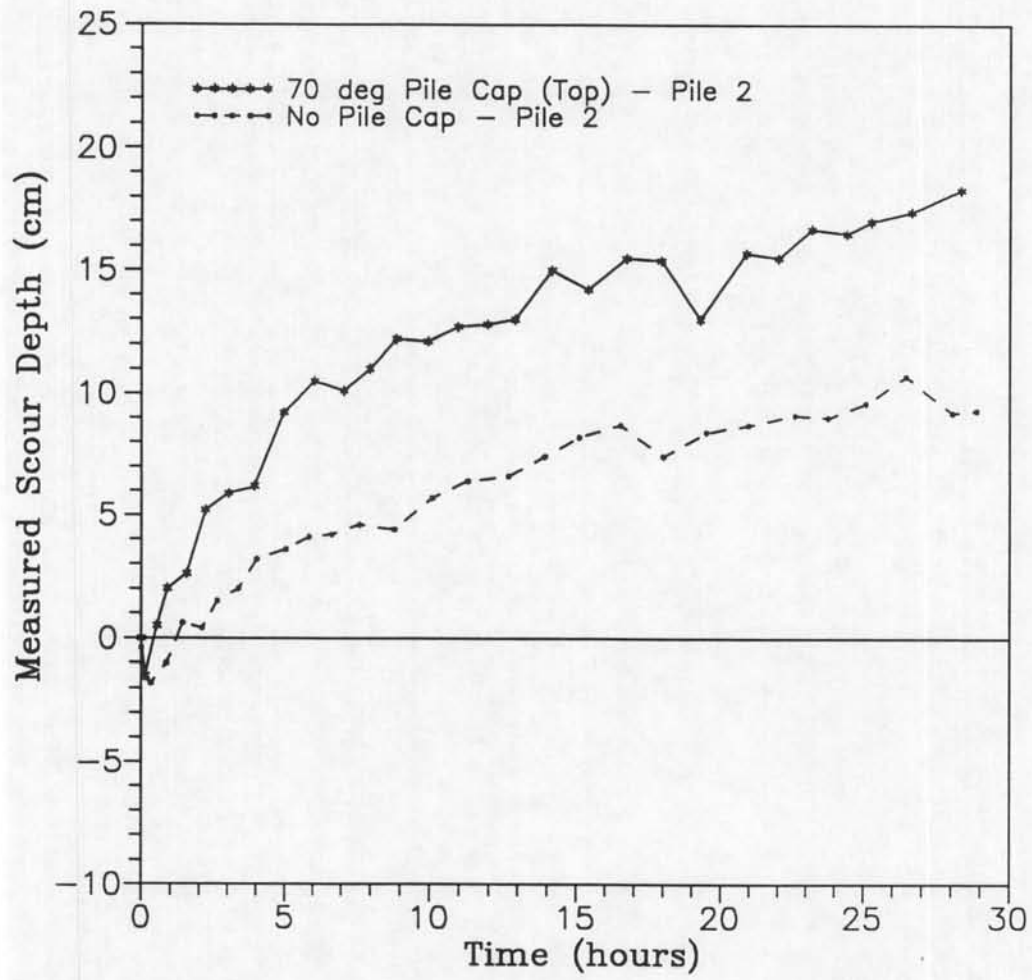


Figure 5.16 Time rate of scour of pile 2.

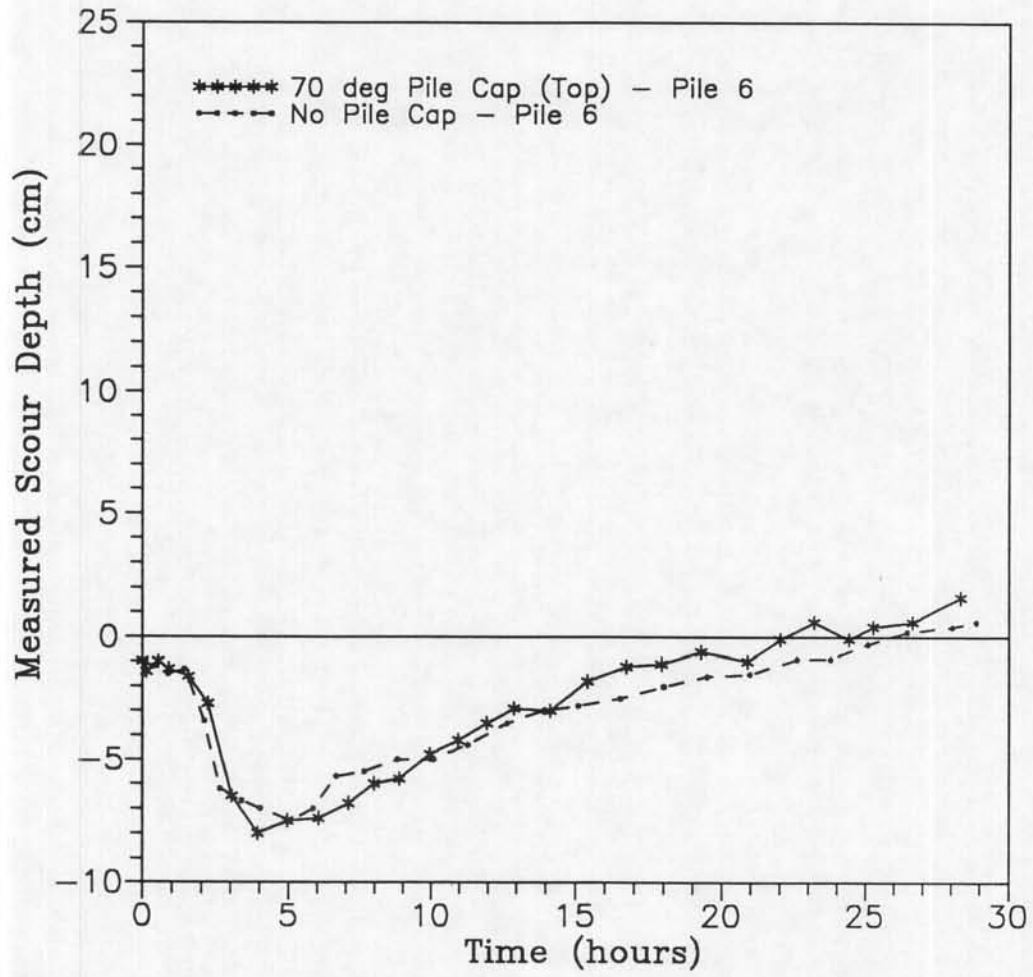


Figure 5.17 Time rate of scour of pile 6.

CHAPTER 6
ANALYSIS OF HYDRODYNAMIC AND SCOUR RESULTS

6.1 Mathematical Model

Preliminary tests indicated that the X sensor probe had to be rotated 90° (such that the filaments were in parallel, horizontal planes) in order for the probe to resolve horizontal variations in the flow direction (see Chapter 4). In this position, the probe measured the two horizontal components of velocity, U and V. It was assumed that the turbulent shear stress is proportional to $\rho(u'^2 + v'^2)$. The total shear stress would then be

$$\tau = \mu \frac{\partial \bar{U}}{\partial z} + a\rho(u'^2 + v'^2), \quad (6.1)$$

where "a" is a dimensionless constant to be determined from measurements in front of (and not influenced by) the structure. The analysis resulted in a value of 0.10 for "a".

The dimensionless shear stress, τ_d , was then computed at each grid point where flow measurements were made. The dimensionless shear stress is the ratio of the shear stress at any point, τ , and the shear stress of the undisturbed flow in front of the structure, τ_o , at $z = 3$ mm. The surface fit program SURFER, was used to interpolate and map the dimensionless shear stress over the study area. SURFER was also used to fit the scour data. The grid laid out over a portion of the area expected to scour is

shown in Figure 4.4. With the existing probe support, hydrodynamic measurements closer than 11.1 cm to the piles could not be made due to the pile cap. This made it necessary to extrapolate the shear stress from the closest grid point to the piles.

In attempting to obtain a functional relationship between the equilibrium scour depth and the shear stress, the following guidelines were used. The relationship should be as simple as possible and be directed at the specific problem at hand. That is, it should be directed at equilibrium scour depths at the transition from clear water to live bed conditions thus eliminating the need to introduce sediment properties, etc. The thought being that this relationship could be extended to include a broader range of conditions at a later date. In light of the above, the following form was selected,

$$de = f(\tau), \quad (6.2)$$

where

de = equilibrium scour depth,

$$f(\tau) = b \left(\frac{\tau - \tau_o}{\tau_o} \right)^c = b (\tau_d - 1)^c, \quad (6.3)$$

$$\tau_d = \frac{\tau}{\tau_o} \quad (6.4)$$

and b and c are empirical coefficients.

Since the increase in bottom shear stress caused by the different multiple pile structures was the only parameter changing during the hydrodynamic experiments, the coefficients b and c were determined by a least squares best fit between the predicted and estimated equilibrium scour depths at a section at the front of the pier. The estimated equilibrium bottom elevation is the measured bottom elevation at 28 hours extrapolated to equilibrium and adjusted for the velocity being below the transition between live bed and clear water conditions. The coefficients are considered constant for the range of conditions considered here. For a more general formulation, the coefficients will undoubtedly be dependent on some of the quantities held constant during these experiments. Various sediment transport equations have been developed using the critical shear stress, τ_c and/or bed shear stress, τ_s . The shear stresses in these equations were raised to powers varying from 0.33 to 3 (see Table 2.1).

The first step in evaluating the coefficients was to assign a value for c . Using the dimensionless shear stress, τ_d , and the measured scour depth at grid point A3, a value for b was computed. Grid point A3 (see Figure 4.4) was selected because the time rate of scour curves in Figures 5.8 and 5.9 indicate that this area is close to its equilibrium scour depth. Grid point A2 was not chosen because τ_d is lower there than at A3. The reason being that point A2 is far enough forward that the flow at that point is less influenced by the structure. The values obtained for b and c are 4.62 cm and 0.5 respectively.

SURFER was then used to create a finer grid of the estimated shear stresses and the corresponding scour depths at these grid points were computed using Equation 6.3.

One constraint on the computed equilibrium scour depths was that the scour depth between two adjacent grid points could not change more than that allowed by the sediment angle of repose, 32° (Melville and Raudkivi, 1977). The predicted equilibrium scour depth is the larger between the scour depth based on the dimensionless shear stress and the scour depth which satisfies the sediment angle of repose.

6.2 Mathematical Model Results

To simplify the presentation of the results, bottom elevations instead of predicted and measured scour depths are presented. Bottom elevation, z , and scour depth, d_e , are related by $z = -d_e$. Figures 6.1 to 6.12 show τ_d , the measured bottom elevation after a 28 hour scour test, the estimated and predicted equilibrium bottom elevations for the no pile cap and the 70° pile cap (top position) structures. The results indicate that the predicted equilibrium bottom elevations are closer to the measured bottom elevations towards the front of the structure. Figure 6.13 shows the results at row 3 ($x = 40$ cm) for the 70° pile cap (bottom position) structure. The predicted equilibrium bottom elevation is actually less than that measured. A possible explanation for this is that the flow-structure configuration which was used for the hydrodynamic measurements significantly changed as the scour hole developed. As the scour hole developed, a new turbulence generating mechanism (the piles) came into effect. That is, the computed bottom elevation in Figure 6.13 is for a structure with a pile cap that extends down through the bottom.

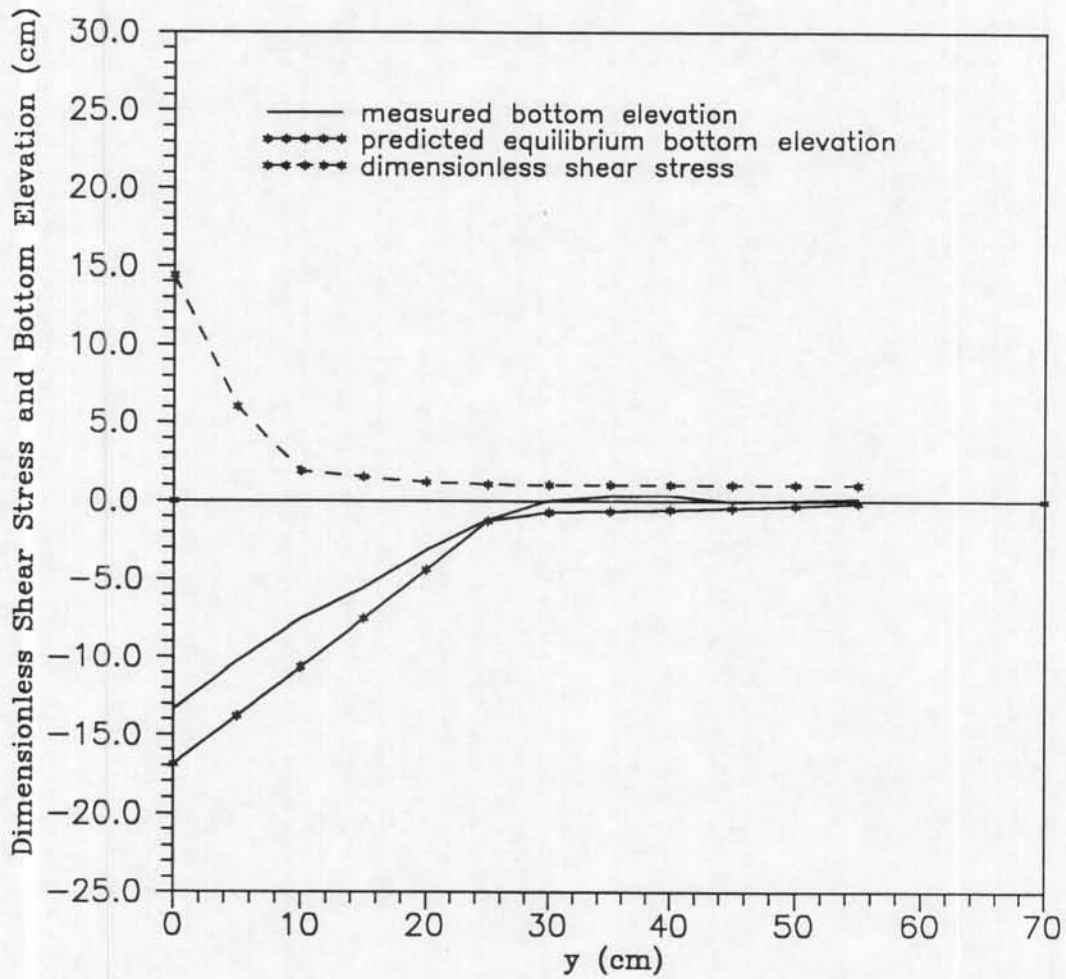


Figure 6.1 Comparison of measured bottom elevation, predicted equilibrium bottom elevation and dimensionless shear stress for the no pile cap structure (row 2 : $x = 10$ cm).

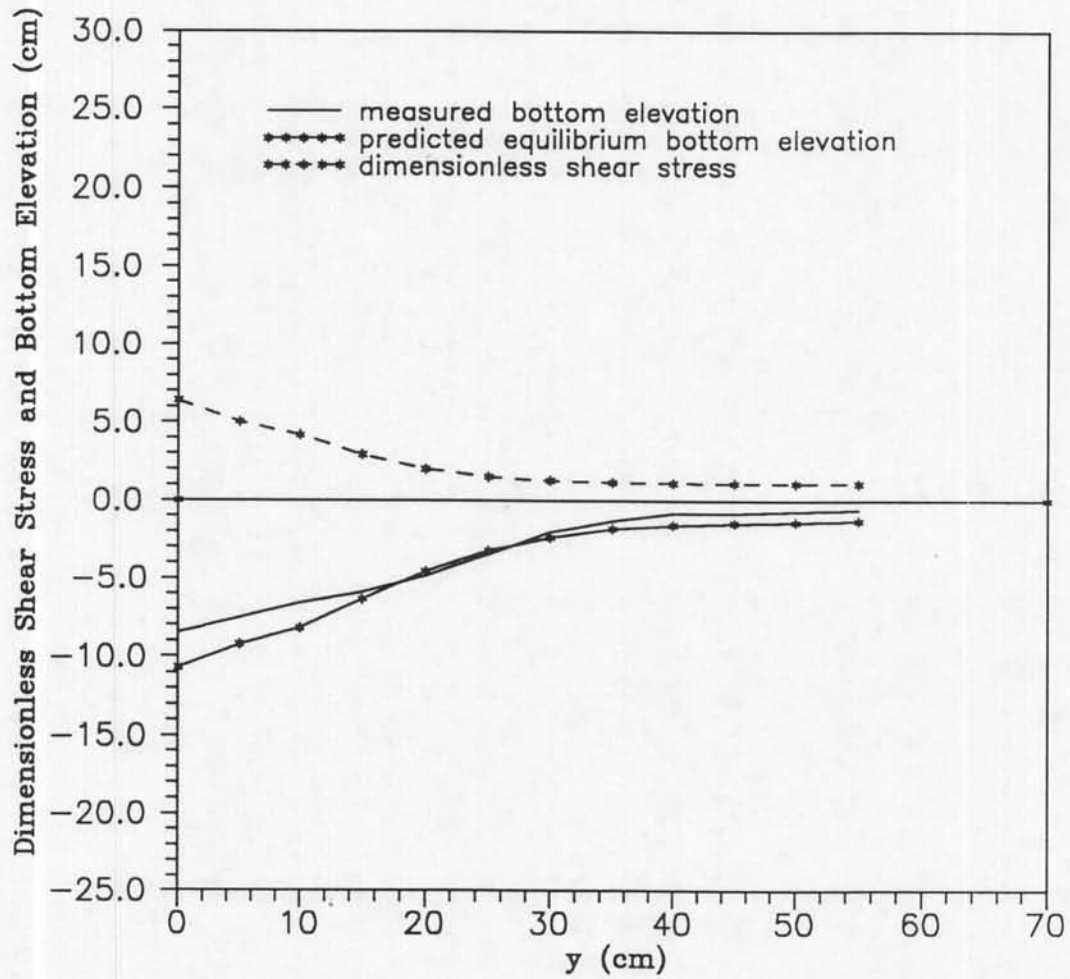


Figure 6.2 Comparison of measured bottom elevation, predicted equilibrium bottom elevation and dimensionless shear stress for the no pile cap structure (row 3 : $x = 40$ cm).

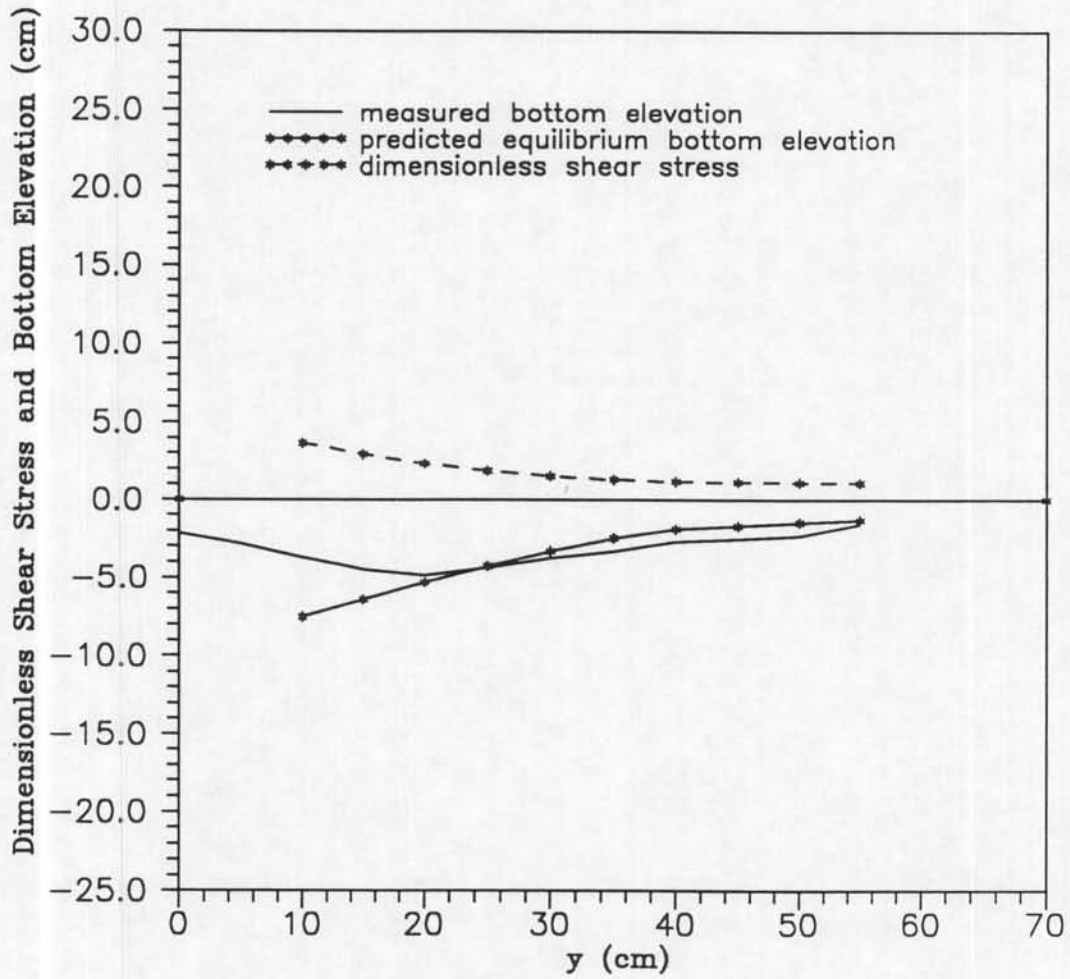


Figure 6.3 Comparison of measured bottom elevation, predicted equilibrium bottom elevation and dimensionless shear stress for the no pile cap structure (row 4 : $x = 70$ cm).

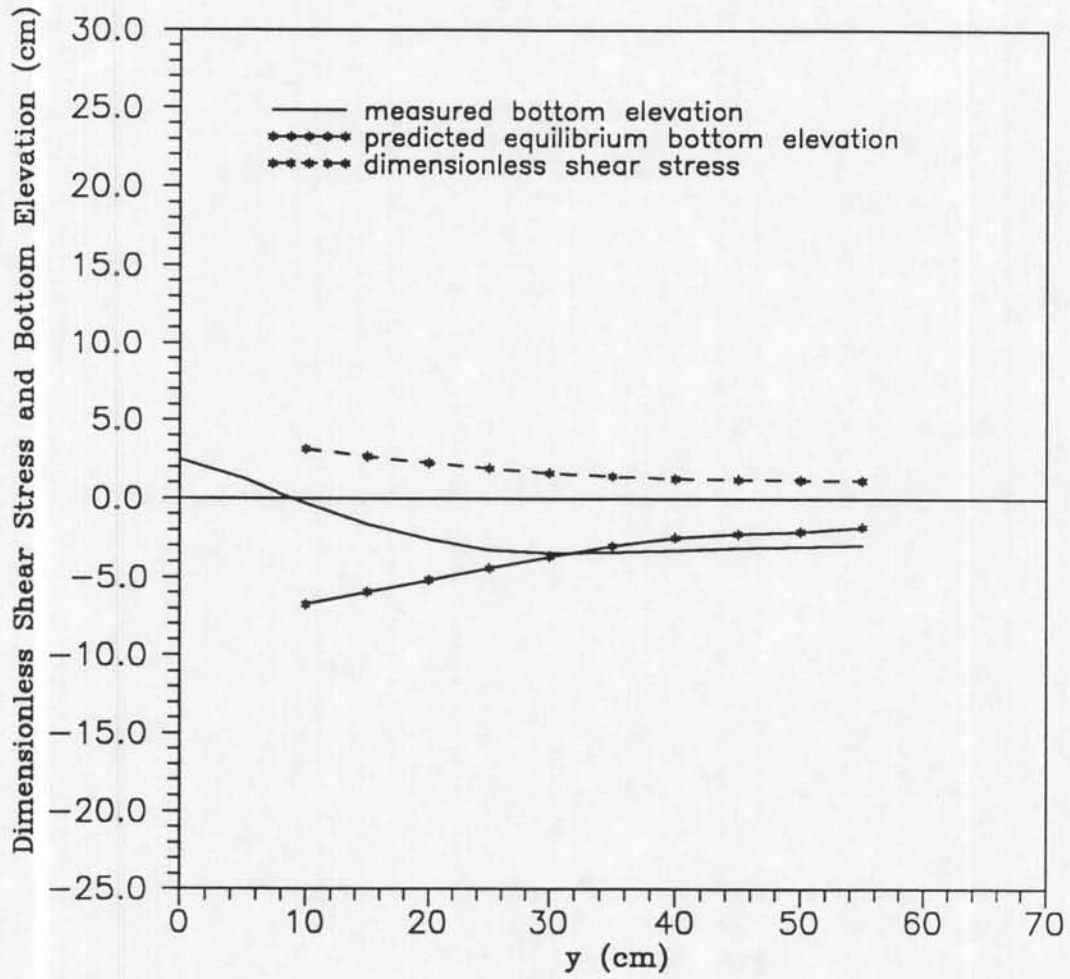


Figure 6.4 Comparison of measured bottom elevation, predicted equilibrium bottom elevation and dimensionless shear stress for the no pile cap structure (row 5 : $x = 100$ cm).

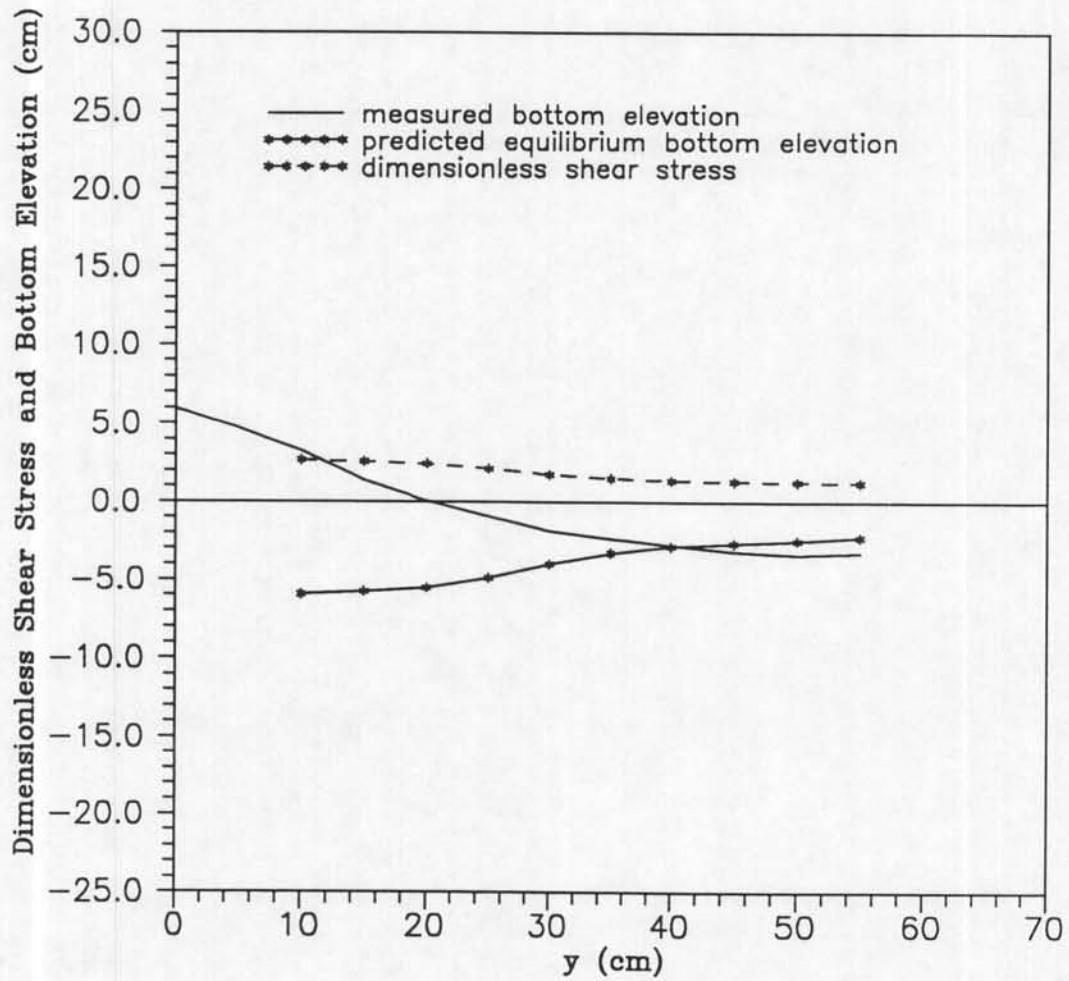


Figure 6.5 Comparison of measured bottom elevation, predicted equilibrium bottom elevation and dimensionless shear stress for the no pile cap structure (row 6 : $x = 130$ cm).

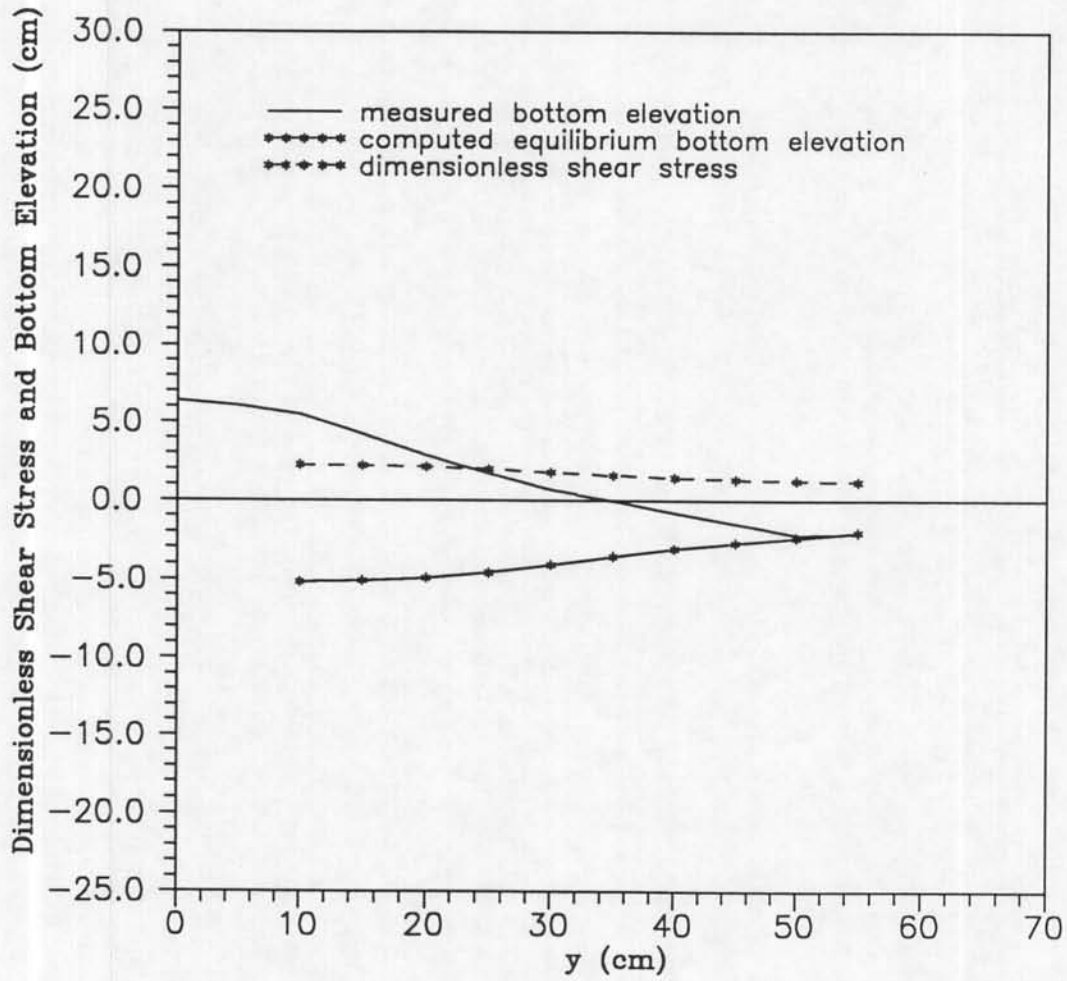


Figure 6.6 Comparison of measured bottom elevation, predicted equilibrium bottom elevation and dimensionless shear stress for the no pile cap structure (row 7 : $x = 160$ cm).

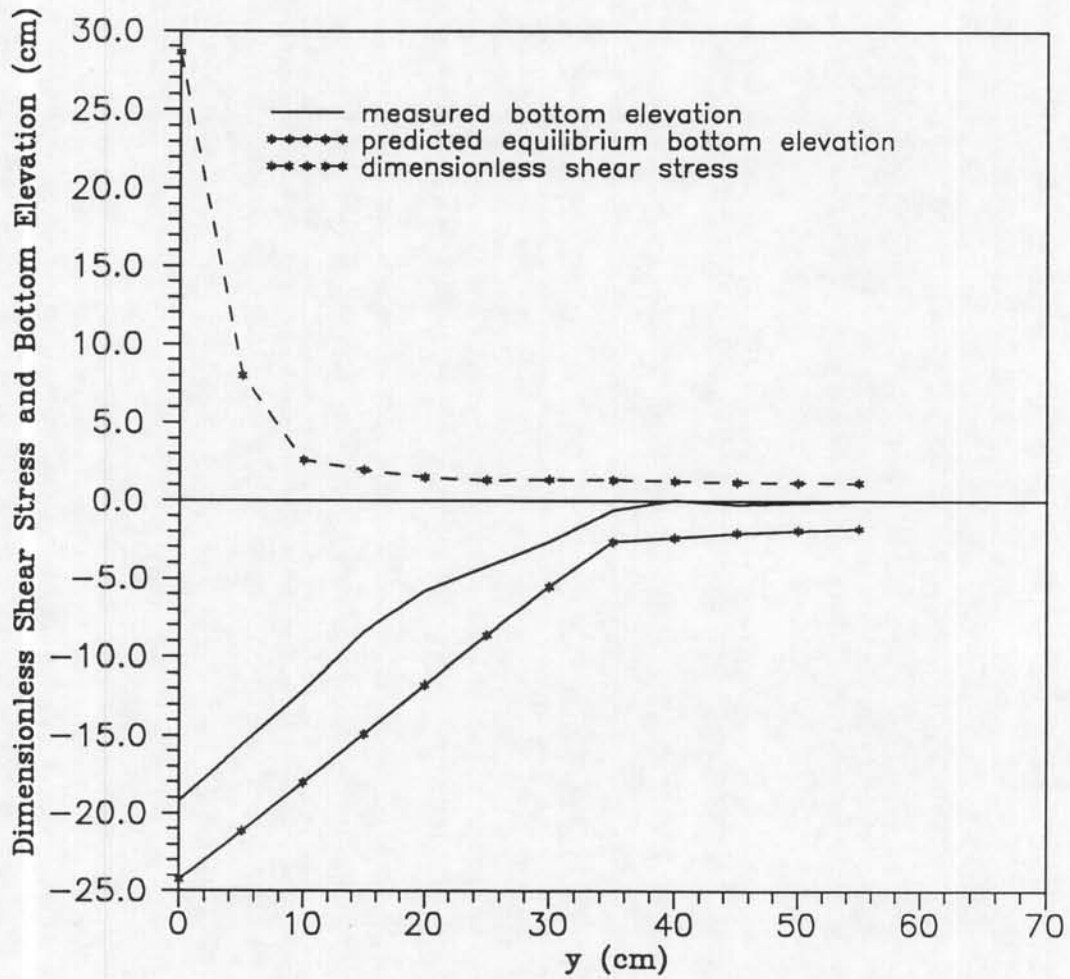


Figure 6.7 Comparison of measured bottom elevation, predicted equilibrium bottom elevation and dimensionless shear stress for the 70° pile cap structure (row 2 : $x = 10$ cm).

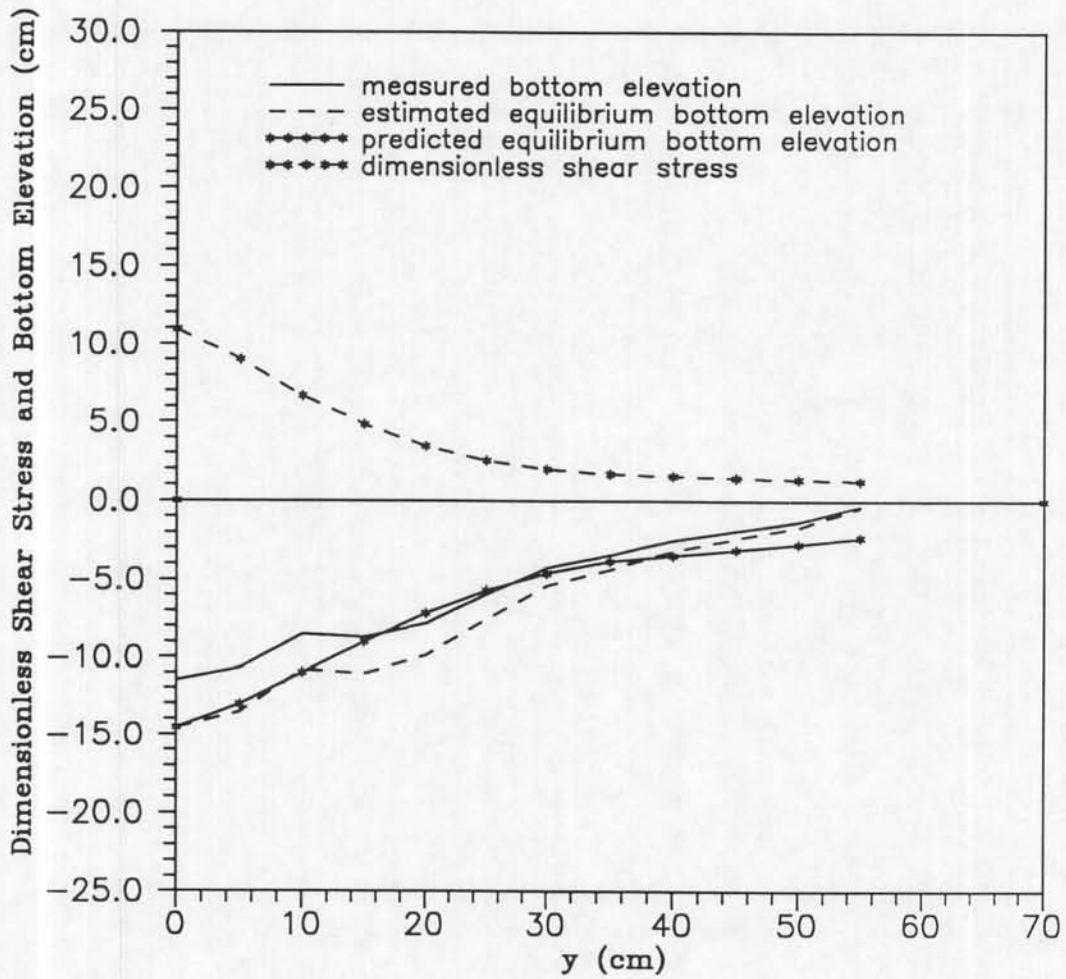


Figure 6.8 Comparison of measured bottom elevation, estimated and predicted equilibrium bottom elevations and dimensionless shear stress for the 70° pile cap (top) structure (row 3 : $x = 40$ cm).

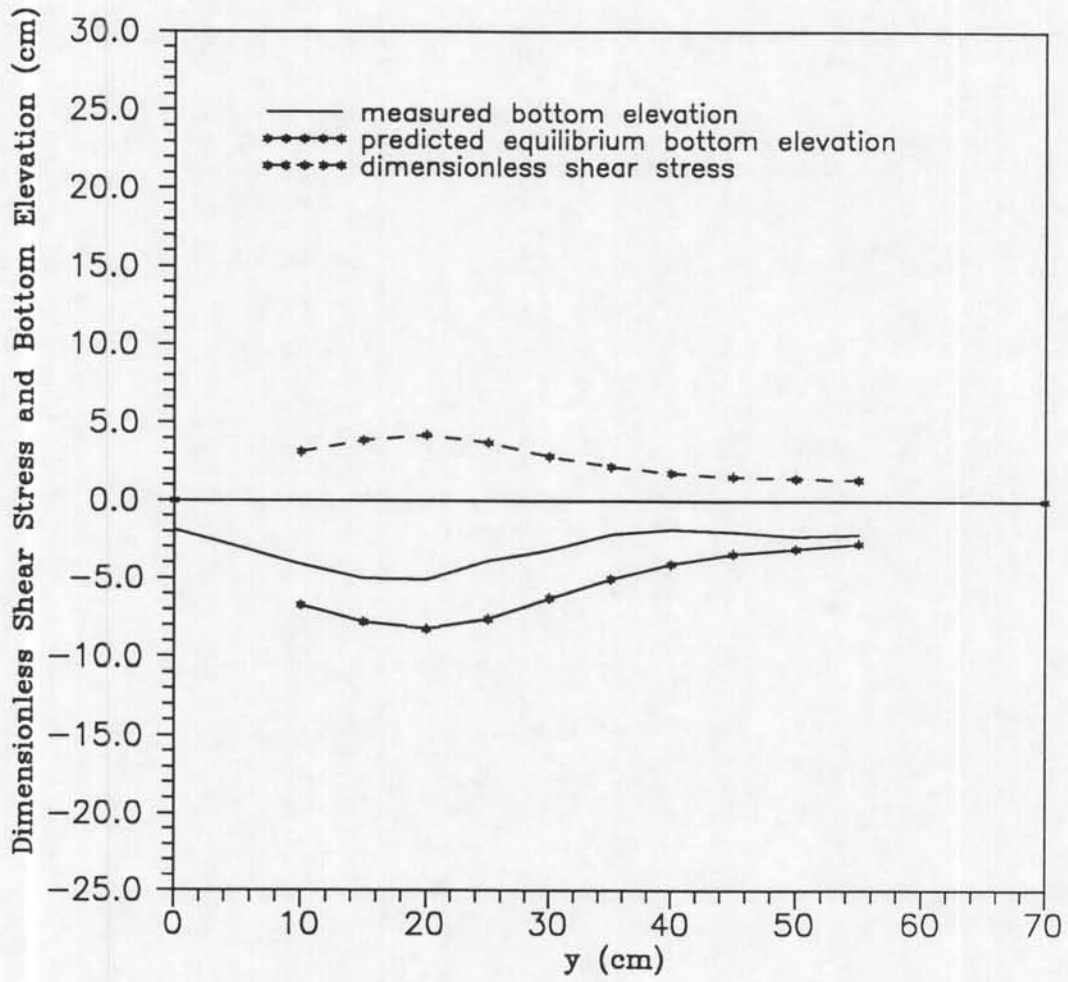


Figure 6.9 Comparison of measured bottom elevation, predicted equilibrium bottom elevation and dimensionless shear stress for the 70° pile cap (top) structure (row 4 : $x = 70$ cm).

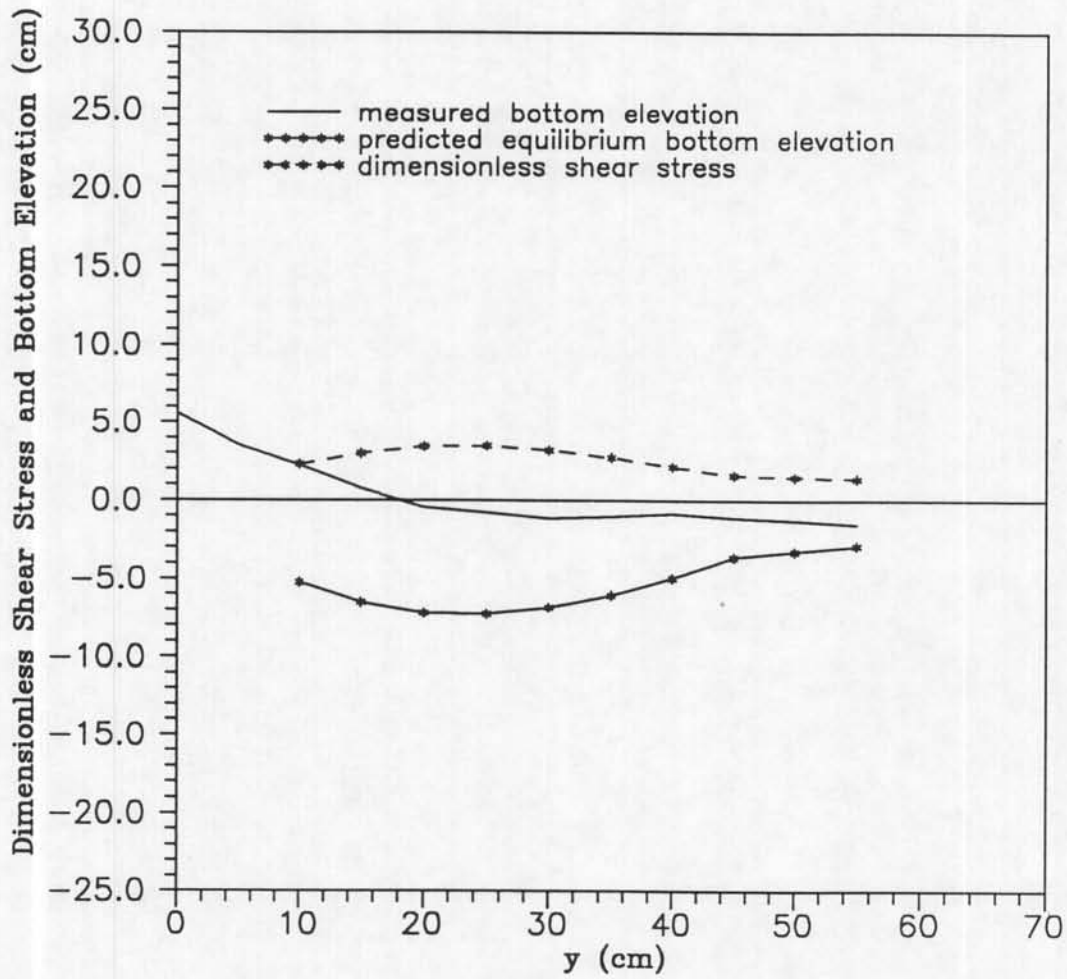


Figure 6.10 Comparison of measured bottom elevation, predicted equilibrium bottom elevation and dimensionless shear stress for the 70° pile cap (top) structure (row 5 : $x = 100$ cm).

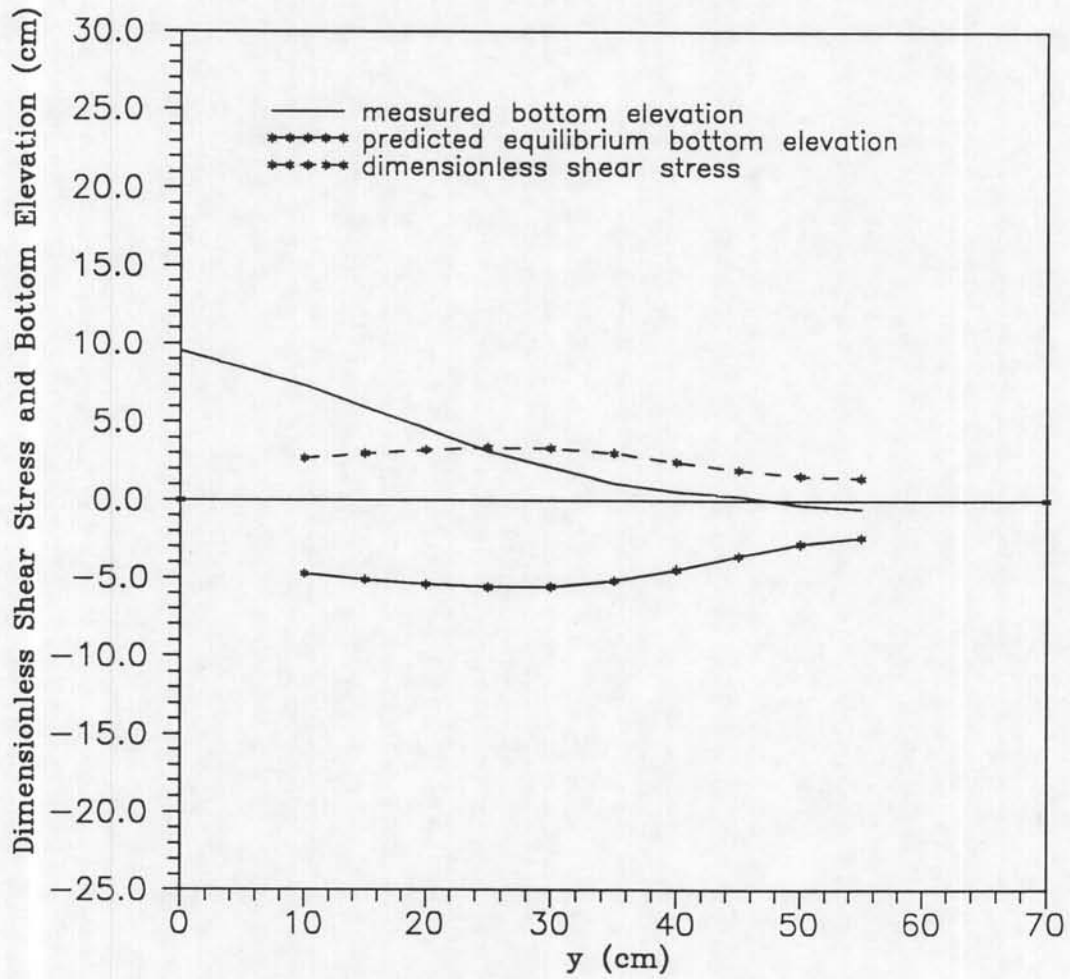


Figure 6.11 Comparison of measured bottom elevation, predicted equilibrium bottom elevation and dimensionless shear stress for the 70° pile cap (top) structure (row 6 : $x = 130$ cm).

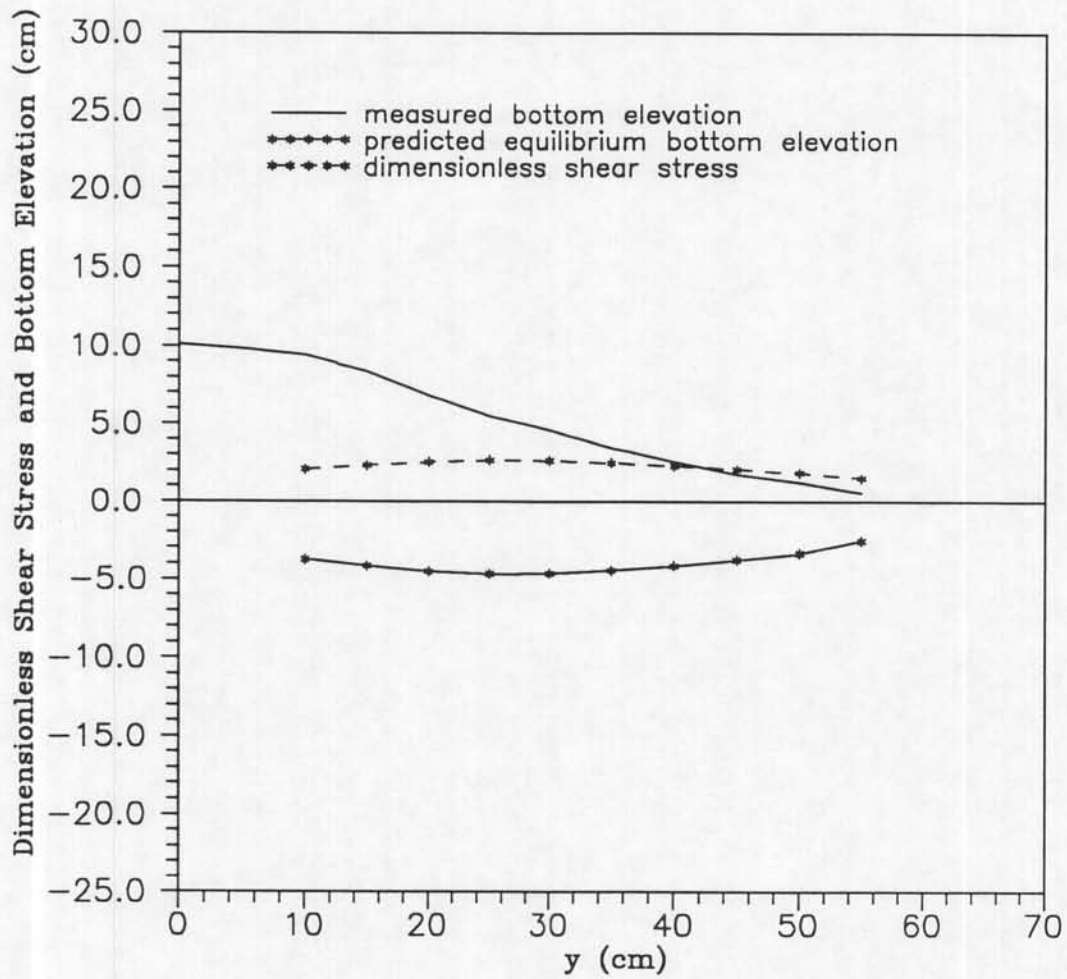


Figure 6.12 Comparison of measured bottom elevation, predicted equilibrium bottom elevation and dimensionless shear stress for the 70° pile cap (top) structure (row 7 : $x = 160$ cm).

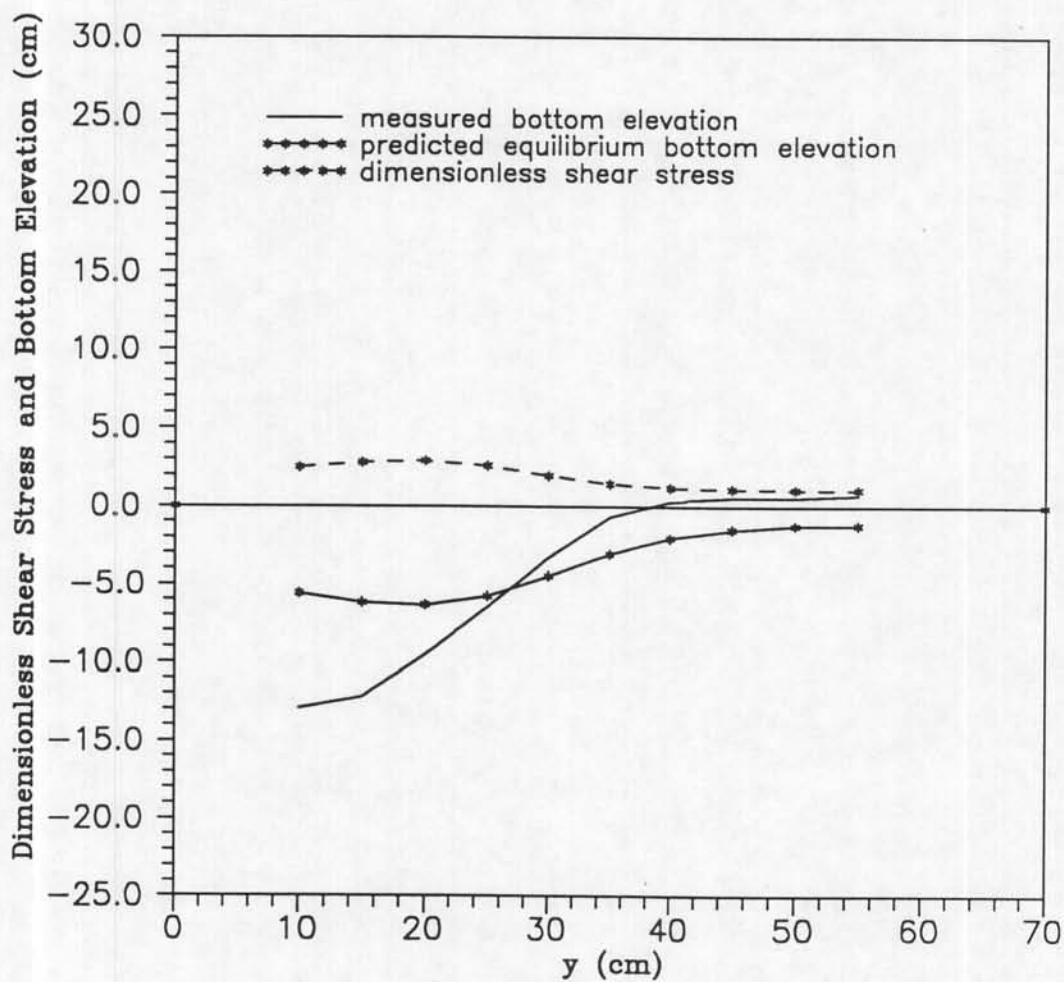


Figure 6.13 Comparison of measured bottom elevation, predicted equilibrium bottom elevation and dimensionless shear stress for the 70° pile cap - bottom (row 3 : $x = 40$ cm).

CHAPTER 7 RESULTS AND CONCLUSIONS

7.1 Results

The primary objective of this study was to determine if equilibrium local scour depths can be predicted from near-bottom flow measurements over the fixed bed near a multiple pile structure. The first step was to measure flow parameters over a portion of the area where scour was anticipated. These measurements were then used to estimate the bottom shear stress over this area. A simple relationship between equilibrium local scour and pre-scoured bottom shear stress was postulated. The coefficients in the formulation were evaluated using measured scour depths extrapolated to equilibrium. In its present form, this relationship is restricted to predicting equilibrium scour depths at the transition from clear water to live bed conditions. Future plans include extending this formula to a broader range of conditions.

The scour depths predicted by this formula seem reasonable and are consistent with extrapolations of scour time series plots. Both the predicted scour depths and the time history plots for various pile rows indicate that the time to reach equilibrium increases dramatically as the distance from the front of the structure increases. The rate of scour around the piles on the leading edge appears to be close to that for a single pile structure, i.e. after 24 hours the scour depth is approximately 90% of the ultimate

(equilibrium) depth. Further downstream, the scour appears to be much less mature at the end of 24 hours and the rates seem to be decreasing.

Figures 5.8 and 5.9 show that piles 1 and 2 of the no pile cap and 70° pile cap (top position) structures approached equilibrium local scour depths at the end of the scour tests (i.e. 28 hours after the start). On the other hand, pile 6, which was located approximately halfway down the structure, was just beginning to scour below the original bottom after 25 hours.

If the relationship developed here (or a similar expression) proves to be valid for a wide range of conditions, the time and cost savings in evaluating design scour depths for complex bridge piers could be significant.

Figures 7.1 and 7.2 are contours of dimensionless shear stress around the no pile cap and 70° pile cap (top position) structures. Figures 7.3 and 7.5 are the measured bottom elevations over the same area. Figures 7.4 and 7.6 are contours of the computed equilibrium bottom elevations (of the area where hydrodynamic flow measurements were made) based on the dimensionless shear stresses in Figures 7.1 and 7.2. These figures show that the predicted equilibrium bottom elevations are deeper than the measured values throughout the area but the difference is greater toward the back of the structure. This is one indication that the scour is much closer to equilibrium near the front of the structure.

The predicted equilibrium bottom elevations do not match the measured bottom elevations for the cases where the pile cap was initially resting on the bottom. This

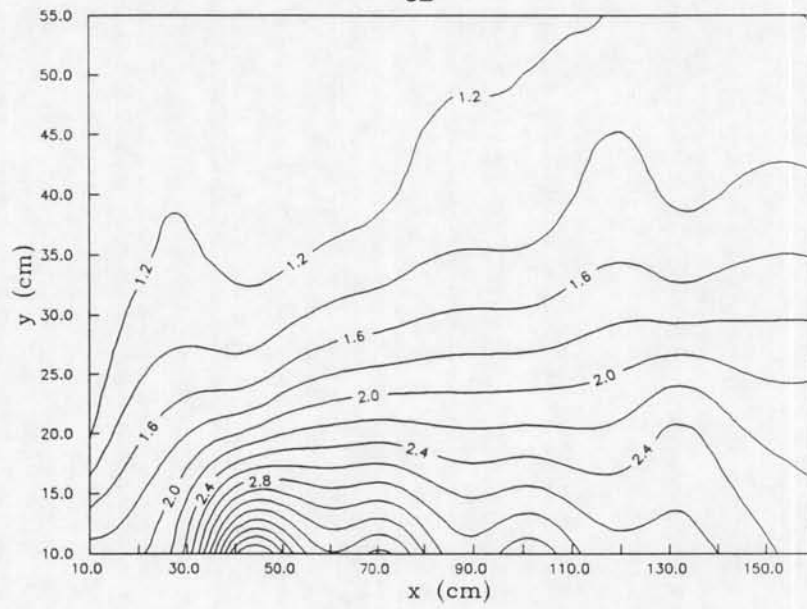


Figure 7.1 Contours of dimensionless shear stress, τ_d , around no pile cap structure.

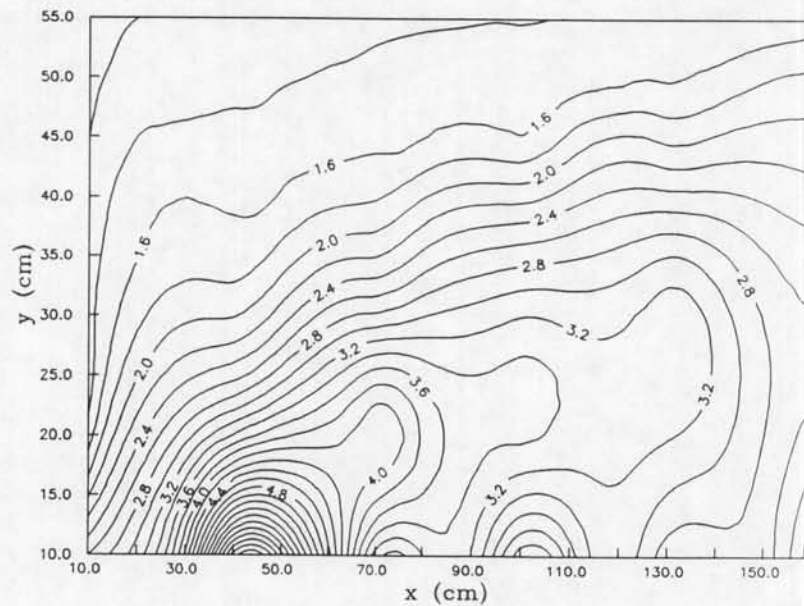


Figure 7.2 Contours of dimensionless shear stress, τ_d , around 70° pile cap (top position) structure.

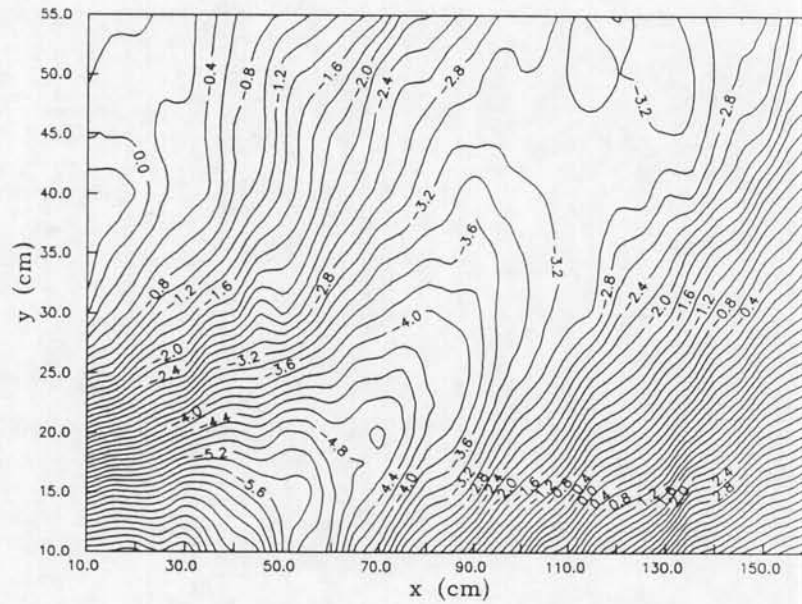


Figure 7.3 Contours of measured bottom elevation around no pile cap structure after completion of the scour test.

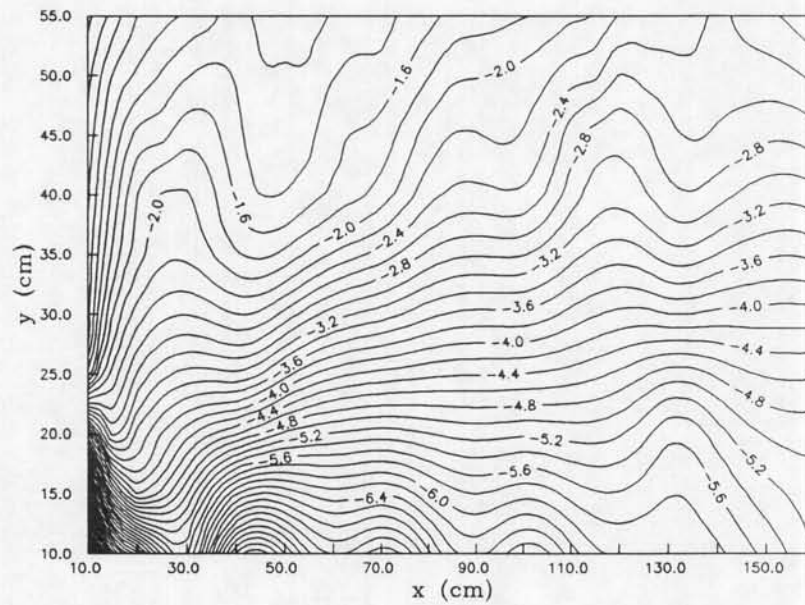


Figure 7.4 Contours of predicted equilibrium bottom elevation around no pile cap structure.

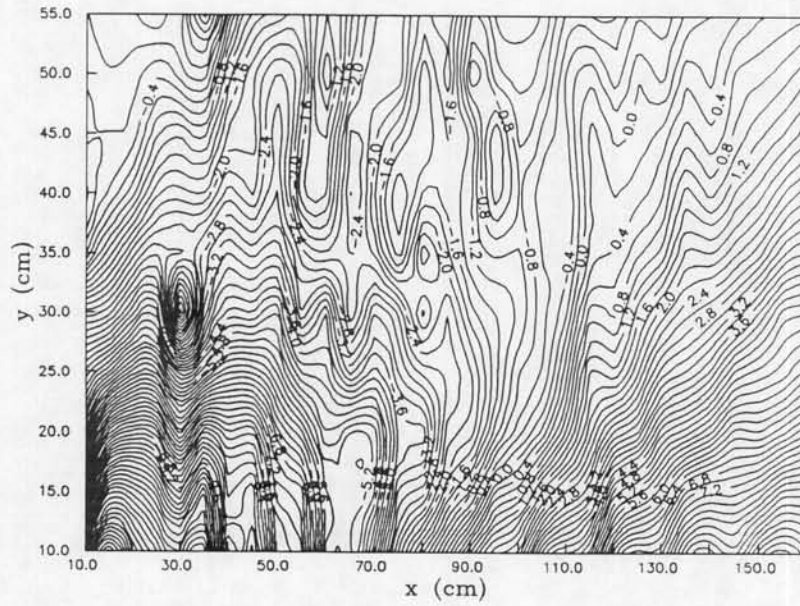


Figure 7.5 Contours of measured bottom elevation around 70° pile cap (top position) structure after completion of the scour test.

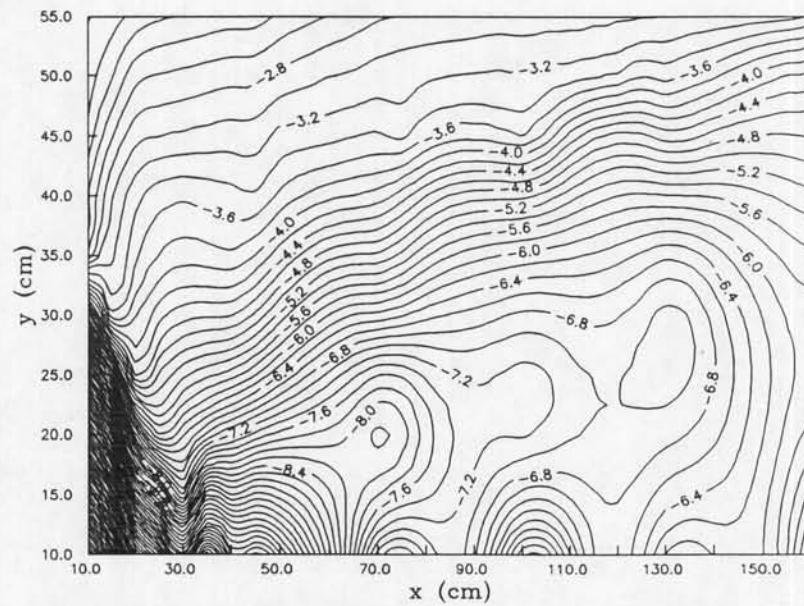


Figure 7.6 Contours of predicted equilibrium bottom elevation around 70° pile cap (top position) structure.

however, is to be expected since the structure shape near the bottom changes abruptly with the development of the scour hole. The scour predictions are better suited for a structure with a pile cap that starts 12.7 cm above the bottom and penetrates deep below the bottom. The scour test results for the case where the pile cap rests on the bottom as shown in Figure 7.7 should not be compared with the hydrodynamic test for that structure for the above stated reasons. Figure 7.8 shows the same structure after the scour test. It is apparent that the development of the scour hole has significantly changed the flow-structure configuration. Figures 7.9 and 7.10 show the 70° pile cap (top position) structure before and after the scour test.

Flow measurements closer to the structure are clearly needed. As stated earlier, time and cost constraints prevented the necessary modifications to the constant temperature X sensor probe support to allow these measurements. Such measurements will be included in future studies. One possible improvement would be to use flush mounted shear stress probes in the vicinity of the structure where flows are highly unsteady and the shear stresses are large.

7.2 Conclusions

1. The prediction of equilibrium scour depths from pre-scoured bottom shear stress measurements appears to be feasible based on the results of this study. Additional tests are needed where shear stresses closer to the structure are measured. Some longer duration scour experiments are also needed to better document equilibrium scour depths.

2. The formulation developed in this study cannot predict the equilibrium scour depths around a structure if the flow-structure configuration used for the hydrodynamic study significantly changes as the scour hole develops.
3. The time rate of scour of different pile rows of the structure vary significantly. The front area of the structure may approach equilibrium scour depths after 28 hours but beyond this point the time to equilibrium will be much longer. Longer duration scour tests are needed to quantify these times.

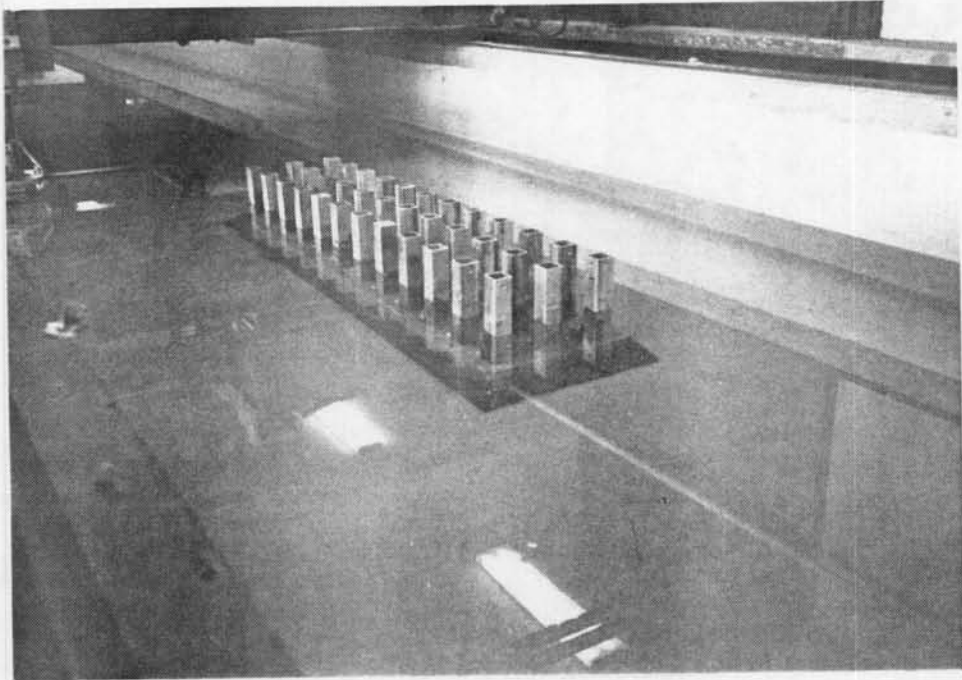


Figure 7.7 70° pile cap (bottom position) structure before the scour test.

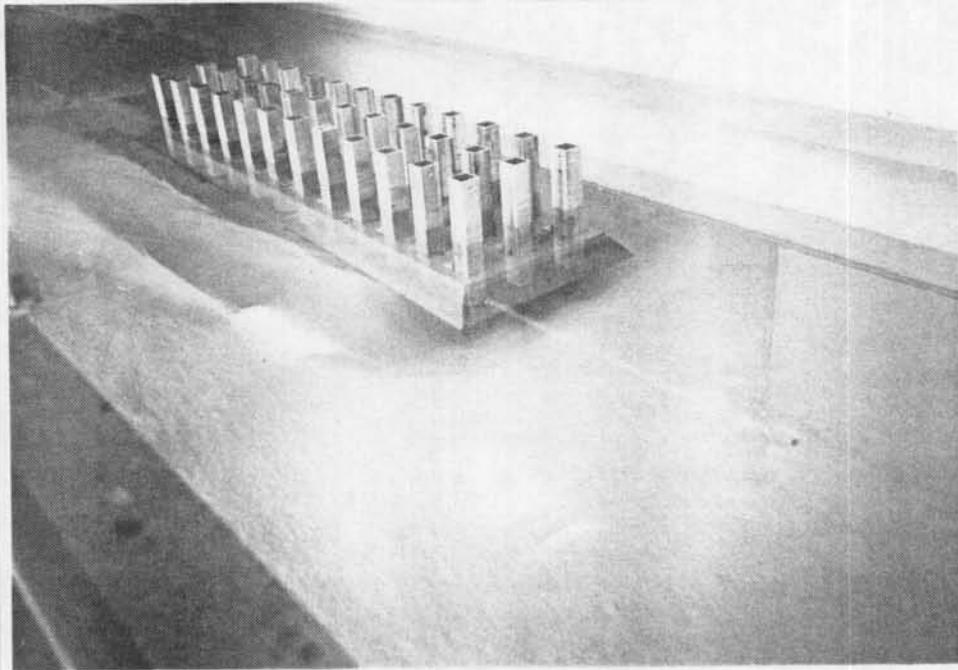


Figure 7.8 70° pile cap (bottom position) structure after completion of the scour test.

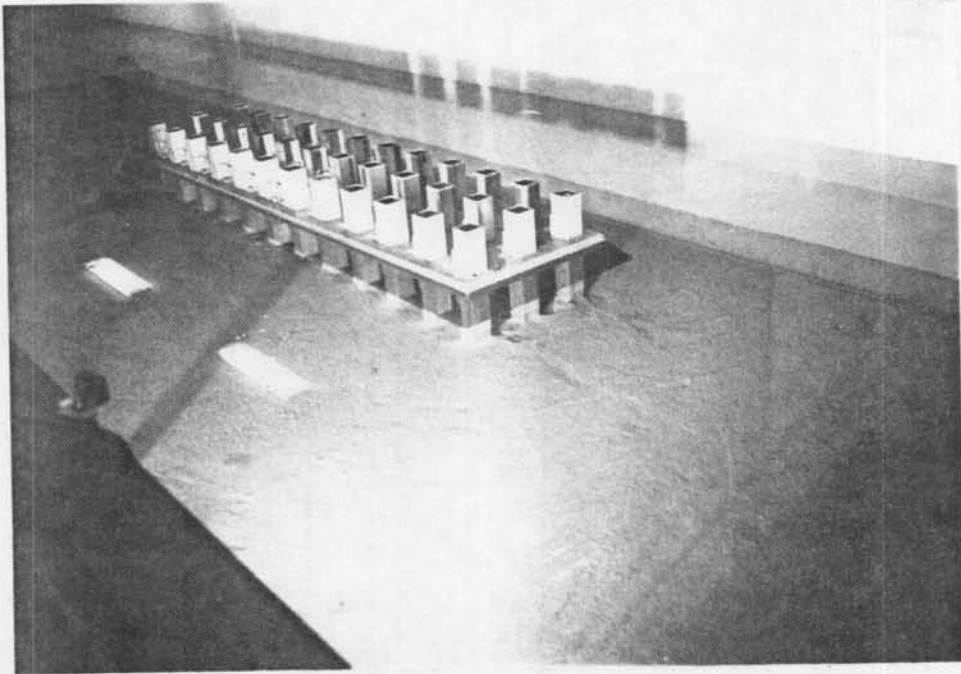


Figure 7.9 70° pile cap (top position) structure before the scour test.

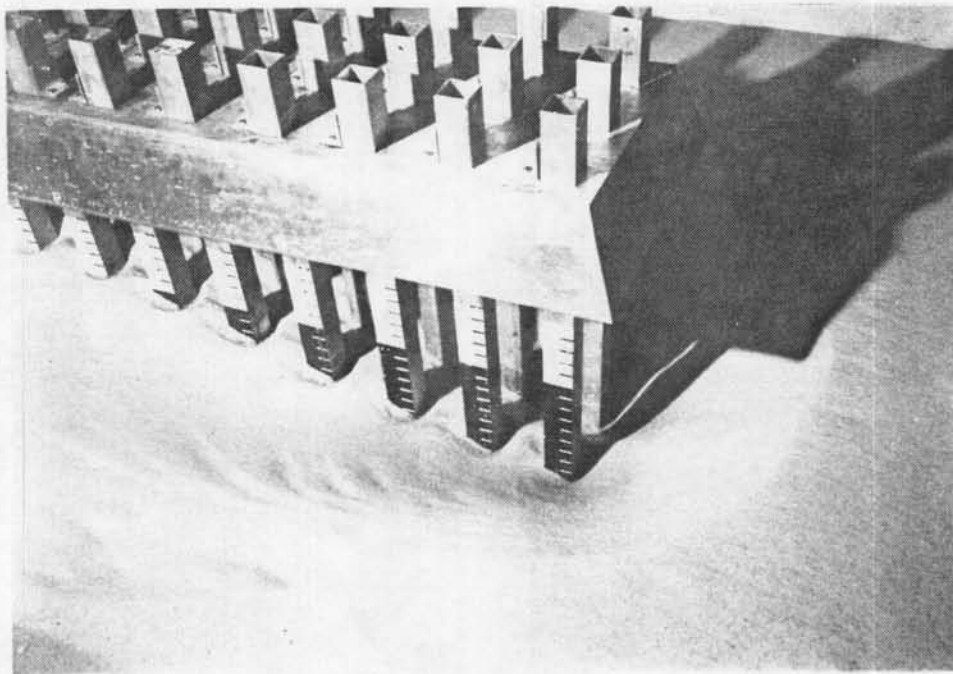


Figure 7.10 70° pile cap (top position) structure after completion of the scour test.

APPENDIX A HYDRODYNAMIC STUDY

This appendix includes information about the instrumentation used in the hydrodynamic study. This consists of a constant temperature anemometer, an x sensor probe and a temperature probe. Also included in this appendix, are the results of preliminary flow measurements conducted prior to the hydrodynamic experiments.

A.1 Instrumentation

Table A.1 Constant temperature anemometer technical data.

Dantec 56C01 CTA Unit - Serial No. 905B0121 688 Dantec 56C17 CTA Bridge - Serial No. 905C0171 1447 and 1435	
Top Resistance	20 Ω
Bridge Ratio	1 : 20
Sensor Resistance Range	3 - 30 Ω
Resistance Measuring Sensitivity	0.1 Ω/V
Probe Cable Length	5 m
Amplifier Shape	Film
Temperature Range	+5 to +40 $^{\circ}C$

Table A.2 X sensor probe technical data.

Dantec R61 Probe - Serial No. 9055R0611		
	Wire 1	Wire 2
Sensor Resistance at 20 $^{\circ}C$	6.96 Ω	6.10 Ω
Probe Lead Resistance	0.60 Ω	0.60 Ω
Coefficient of Resistance	0.39 %/ $^{\circ}C$	0.40 %/ $^{\circ}C$
Overheat Ratio	0.045	0.045
Cable Resistance	0.14 Ω	0.04 Ω

Table A.3 Temperature probe technical data.

Analog Devices AC2626-J4 Temperature Probe Serial No. 2461 9161	
Accuracy	0.125 °C max @ 25 °C
Temperature Range	-55 °C to +140 °C
Voltage Supply	+4 V to +30 V
Output	1 μ A/K
Length	101.6 mm
Diameter	4.76 mm

A.2 Temperature Correction

The ACQWIRE data acquisition software applies a correction to the measured raw voltages and is valid for small temperature changes such that the physical parameters of the fluid can still be assumed to be constant. This temperature adjustment is shown below,

$$V_{bo} = V_b \left(1 - \frac{\alpha \delta T}{a} \right)^{-0.5}, \quad (\text{A.1})$$

where

V_{bo} = bridge voltage at ambient fluid temperature T_o ,

V_b = bridge voltage at temperature T ,

α = temperature coefficient of resistance

(property of probe provided by manufacturer),

- a = overheat ratio $(R_h - R_{co})/R_{co}$,
 R_{co} = cold sensor resistance at T_o ,
 R_h = hot sensor resistance,
 T_o = calibration fluid temperature (i.e. ambient temperature) and
 T = fluid temperature during measurement.

A.3 Vortex Shedding from Probe Holder

Alternate vortex shedding in the wake region of the flow around the x sensor probe support induced a response that influenced the flow measurements. The traversing mechanism and probe support were more rigid in the x direction than the y direction thus the response was greater in the y direction. The response is evident in the power density spectrum of U shown in Figure 4.12. Note the spike in the spectrum at 10 hertz. If the Strouhal Number, S_t , is assumed to be 0.2 for smooth cylinders, the vortex shedding frequency, f_v , can be computed as follows:

$$f_v = \frac{S_t U}{d} . \quad (\text{A.2})$$

- If U = 30.0 cm/sec and
 d = 0.6 cm,
 then f_v = 10 hertz.

This made it necessary to filter the velocity measurements with a bandstop, fourth-order Butterworth filter at 10 hertz. Pre and post filtered time series and energy density spectrum are shown in Figures 4.10 to 4.13.

A.4 Preliminary Flow Measurements

Several flow measurements were taken prior to the hydrodynamic study to determine the different parameters that may affect the results. It was necessary to determine the limitations of the x sensor probe and the characteristics of the flume. The results of these tests are presented and discussed in this section.

1. Time variation of mean velocity

The sampling duration had to be longer than the lowest frequency component of the flow. The sampling rate used was 50 hertz and a plot of mean velocity versus number of data points sampled (i.e. the duration of the record) is shown in Figure A.1. Variations in the mean velocity appear to cease at about 8192 samples so this duration record was selected for all tests.

2. Spatial variation of mean velocity parallel and normal to the pile cap

The grid points chosen for the flow measurements were based on the results of mean velocity measurements parallel and normal to the 70° pile cap (top position) structure. The x sensor probe was placed as close as possible to the structure and measurements taken at $z = 3$ mm between pile 1 and 2, pile 2 and 3, pile 3 and 4 and so forth. Figure A.2 shows the variation of the ratio of the mean velocity next to the structure and the mean velocity in front of and away from the influence of the structure, as the probe was moved along the structure. The results show that by taking measurements between every other pile (e.g. pile 1 and 2, pile 3 and 4 etc.), the velocity field along the structure can be mapped. Figure A.3 shows the variation of the mean velocity across the tank as

the probe was moved away from the structure. The probe was positioned at $x = 10.2$ cm and $z = 3$ mm and the y position of the probe was varied. The coordinates of the grid points used during the hydrodynamic experiments are listed in Table C.1.

3. Variation of mean velocity at the same location

The probe was positioned in front of and away from the influence of the structure and three consecutive mean velocity measurements were taken at the same location ($x = -150$ cm; $y = 8.2$ cm; and $z = 3$ mm). Table A.4 shows that the mean velocity can fluctuate up to 2.5% even without the influence of the structure.

4. Variation of mean velocity across the tank

The probe was once again moved in front of the structure ($x = -150$ cm and $z = 12.8$ cm) and flow measurements were taken as the probe was moved away from the center of the tank. Table A.5 shows that the flow was fully developed across the tank in the test area.

5. X sensor probe cosine response

Preliminary tests using a flow vane and streamers were conducted to determine the changes in horizontal flow direction as a function of time near the structure. This showed that the flow direction varied up to $\pm 15^\circ$ from the mean. To determine if the x sensor probe (filaments in the vertical direction) could resolve the horizontal flow direction changes, the probe was placed in front of and away from the influence of the structure and the mean velocity measured with

the probe at various angles to the flow. Column 2 in Table A.6 shows that the velocity component in the x direction, U , measured by the probe increased as the probe was rotated away from the mean flow direction. The correct cosine response of the x sensor probe is listed in column 3. Turning the probe on its side (filaments in the horizontal direction) improved the ability of the probe to resolve changes in the horizontal flow direction. With the probe in the horizontal position, the U and V velocity components can be measured. Table A.7 lists the measured resultant velocity, $\sqrt{U^2 + V^2}$ (column 2). This value should, of course, remain constant as the probe is rotated (column 3). The results show that the measured velocity when the probe is at 15° to the flow is 1.3% less than the measured velocity when the probe is at 0° . This is within the range of fluctuations of the mean velocity at the same location as shown in Table A.4

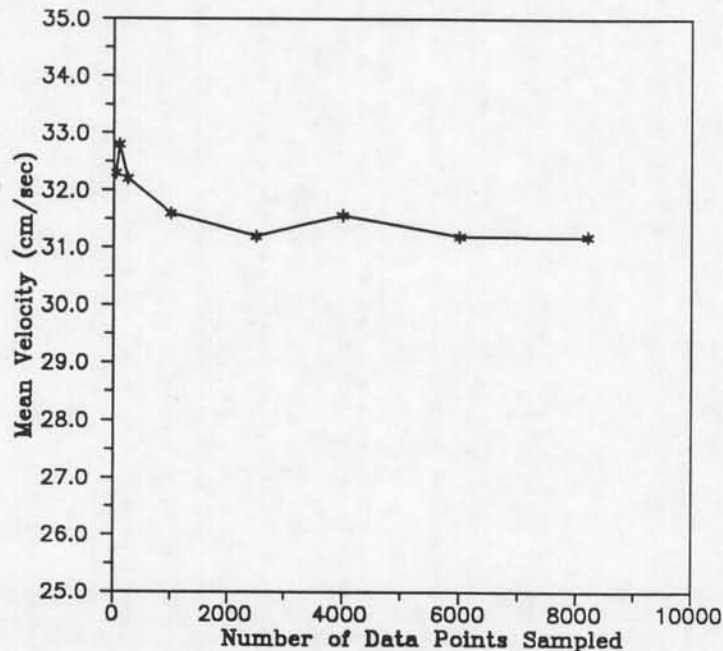


Figure A.1 Mean velocity vs number of data points sampled
($x = 10.2$ cm; $y = 11.1$ cm and $z = 3$ mm).

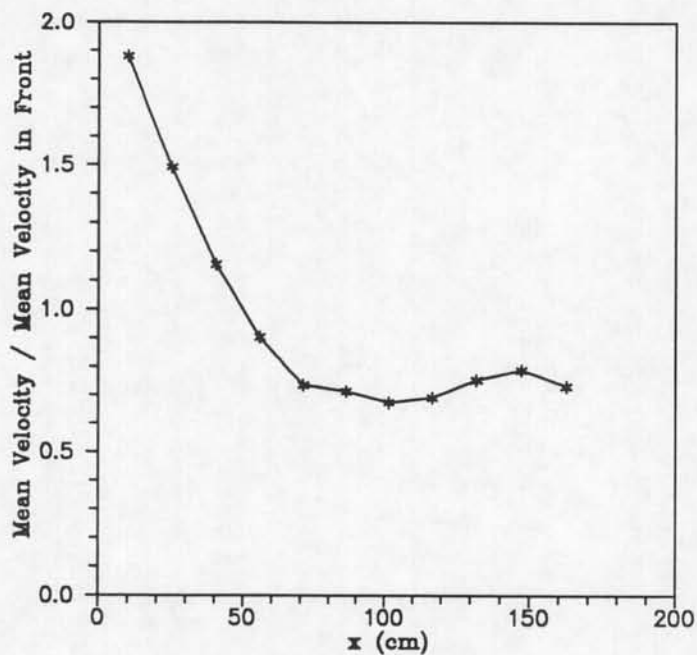


Figure A.2 Variation of mean velocity parallel to the 70° pile cap (top position) structure at $y = 11.1$ cm and $z = 3$ mm.

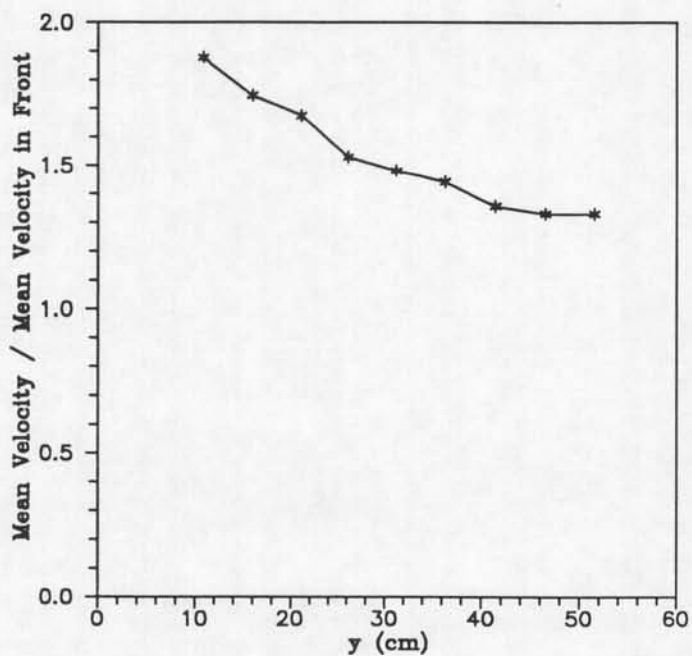


Figure A.3 Variation of mean velocity normal to the 70° pile cap (top position) structure at $x = 10.2$ cm and $z = 3$ mm.

Table A.4 Variation of mean velocity with time at the same location
($x = -150.0$ cm; $y = 8.2$ cm and $z = 3$ mm).

Test Number	Mean Velocity (cm/sec)
1	23.8
2	23.3
3	23.2

Table A.5 Variation of mean velocity across the tank in front of and away from
the influence of the structure ($x = -150.0$ cm and $z = 12.8$ cm).

Test Number	Mean Velocity (cm/sec)	y (cm)
1	36.3	-10.5
2	37.2	9.5
3	37.1	31.7
4	36.5	59.5

Table A.6 X sensor probe cosine response - probe vertical
 (x = -150.0 cm; y = 44.4 cm and z = 3 mm).

Flow Skew Angle	U_{measured} (cm/sec)	U_{correct} (cm/sec)
0	22.98	22.98
7.5	23.15	22.79
15	23.34	22.20

Table A.7 X sensor probe cosine response - probe horizontal
 (x = -150.0 cm; y = 21.1 cm and z = 3 mm).

Angle	Vel_{measured} (cm/sec)	Vel_{correct} (cm/sec)
0	21.03	21.03
15	20.74	21.03
30	19.52	21.03

APPENDIX B SCOUR STUDY

This appendix includes additional information about some of the instrumentation used in the scour experiments. The primary instrument is the echo sounder used for measuring in situ bottom profiles. Also included in this appendix, are detailed information about the sediment used in the tests.

B.1 Instrumentation

Table B.1 Echo sounder technical data.

Simrad Mesotech 810 Serial No. 9866	
Transmitter	
Transmitter	4 selectable pulse lengths and 2 selectable power levels
Operating Frequency	2.25 MHz
Output Power	200 Watts max
Beam width	0.8 degrees
Receiver	
Maximum Range	2.6 m
Repetition Rate	100 Hz
Assumed Sound Velocity	1475 m/sec
Output Frequency	455 Hz
Miscellaneous	
Temperature	Operating: -10 to +40 °C
Dimensions	8.9 cm square x 20.3 cm long

The acoustic bed profiling system is based upon the use of an echo sounder operating at 2.25 Mhz. The 2.25 Mhz operating frequency was chosen to give reasonable accuracies at short ranges, as well as to ensure sufficient energy in the reflection from the bed. A 10 μ sec pulse is emitted at a 100 Hz rate. The returned pulse is an analog time/amplitude history of the water column. The travel time of the signal is proportional to the distance to a reflecting object. The amplitude of the pulse at any point in time is a measure of the number, size and density of reflecting particles

in the water column. The specifications of the echo sounder are listed above in Table B.1.

B.2 Echo Sounder Head Angle Calibration

The echo sounder head angle is the inclination of the echo sounder head relative to a vertical line. Figure 5.1 is a definition sketch of the echo sounder depth measuring system. A protractor was mounted on the side of the sounder head to measure this angle. The sounder head was calibrated by moving the head to different angles and recording the output from the potentiometer. Figure B.1 shows the relationship between the echo sounder angle and the output voltage from the potentiometer and a best fit line is plotted through the data points. The equation of this line is:

$$\Theta \text{ (degrees)} = 41.10 - 11.16 V . \quad (\text{B.1})$$

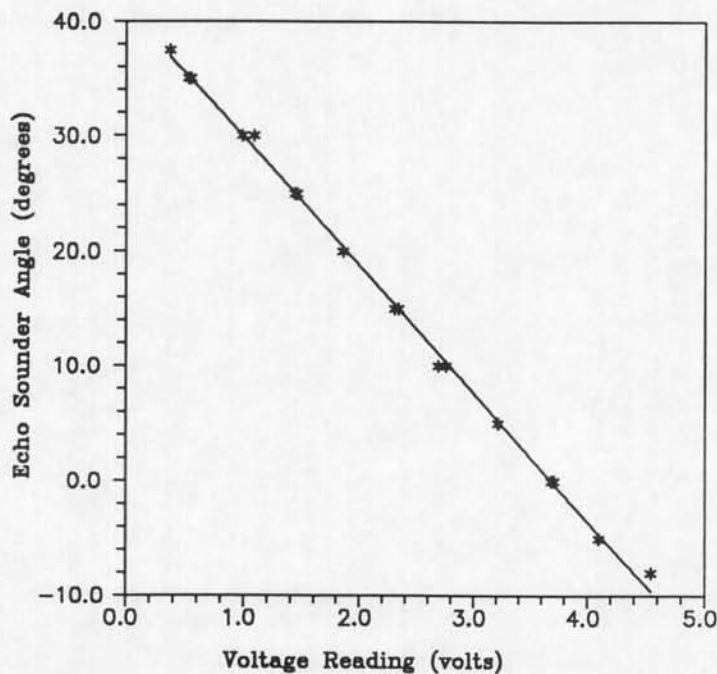


Figure B.1 Calibration curve for the echo sounder head angle.

The echo sounder was then tested on a flat bottom and the bottom mapped by the echo sounder is shown in Figure B.2. The figure shows deviations of up to ± 10 mm from the flat bottom. A closer examination of the echo sounder mechanism showed that there was some play in the gears driving the sounder head. This resulted in a difference in the sounder head angle being recorded by the position potentiometer and the actual angle. This made it necessary to add a correction to the echo sounder angle calibration curve. Since the deviations from the flat bottom were largest at the ends of the swing of the sounder head, the angle readings were limited to the range -7° to 32° . The modified calibration curves are listed below.

For the swing from -7° to 0° ,

$$\Theta \text{ (degrees)} = 39.60 - 11.16 V, \quad (\text{B.2})$$

for the swing from 0° to 32° ,

$$\Theta \text{ (degrees)} = 39.102 - 11.16 V, \quad (\text{B.3})$$

for the swing from 32° to 0° ,

$$\Theta \text{ (degrees)} = 42.60 - 11.16 V \quad (\text{B.4})$$

and for the swing from 0° to -7° ,

$$\Theta \text{ (degrees)} = 43.10 - 11.16 V. \quad (\text{B.5})$$

The modified calibration curves for the echo sounder head angle and the original calibration points are plotted on Figure B.3 and the bottom mapped in Figure B.2 is shown in Figure B.4 using the modified calibration curves. The deviations from the flat bottom were reduced to ± 4 mm.

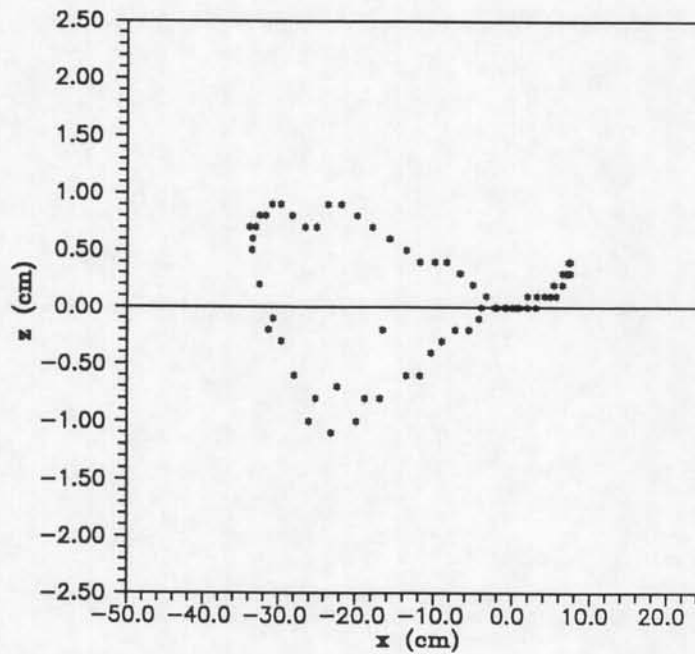


Figure B.2 Profile of flat bottom using original calibration curve.

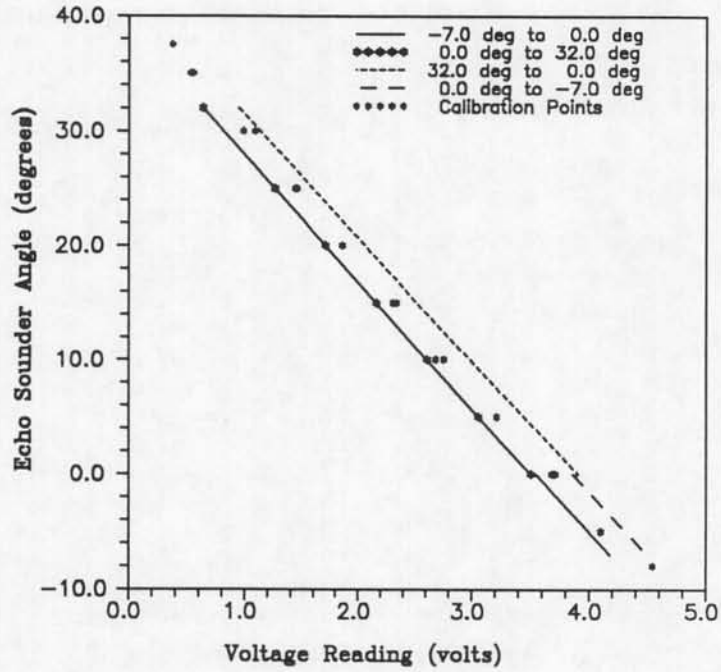


Figure B.3 Modified calibration curves of the echo sounder head angle.

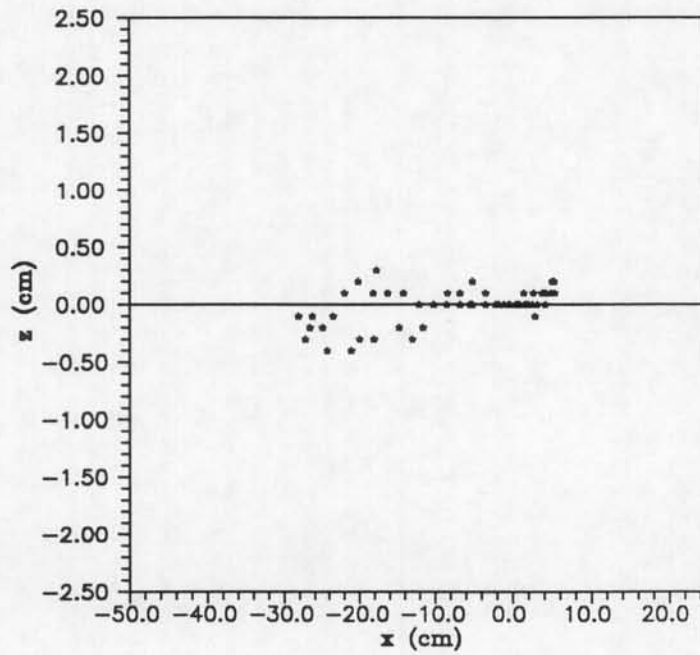


Figure B.4 Profile of flat bottom using modified calibration curves.

B.3 Sediment

The sediment used in the test area was divided into three categories according to grain size distribution. The largest quantity (category 1) was as purchased and contained sizes ranging from 0.2 to 0.8 mm (see Figure B.5). This sand was placed in regions of the test area where scour was not anticipated. The second category contained grain size diameters ranging from 0.84 to 2.00 mm (see Figure B.6). This sand was used to cap and anchor the sand in category 1. The cap was approximately 2 inches in depth. The third category had the grain size distribution shown in Figure B.7 and had diameters ranging from 0.42 to 0.84 mm. This sand occupied the central region of the test area. Figure C.3 shows the partition used in separating the central region during the sand placement process.

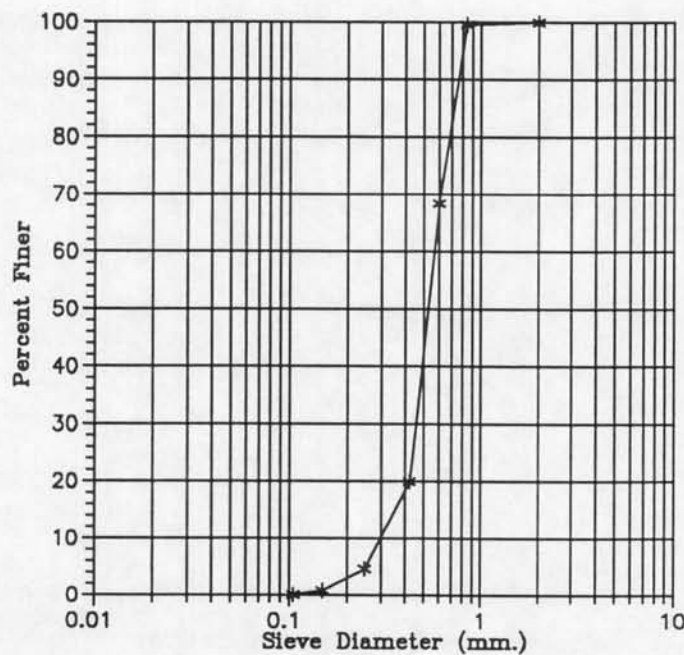


Figure B.5 Sediment size distribution for Category 1 sand (away from structure).

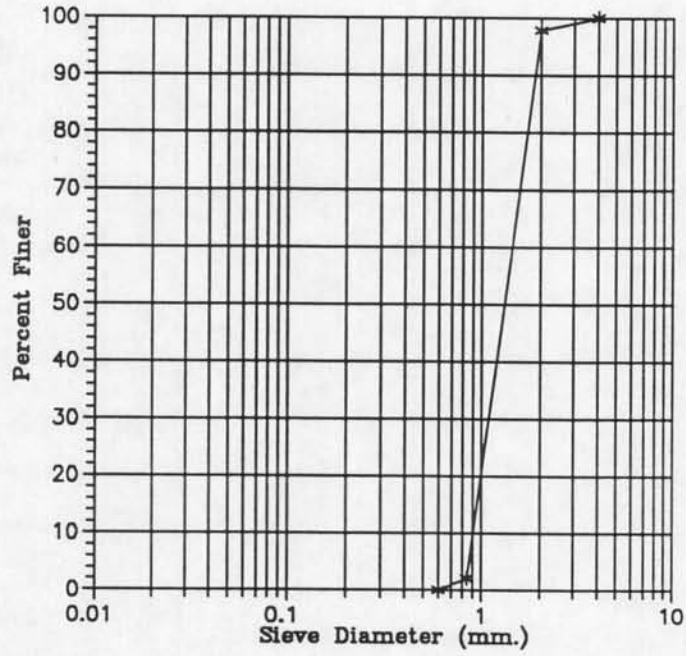


Figure B.6 Sediment size distribution for Category 2 sand (anchoring layer).

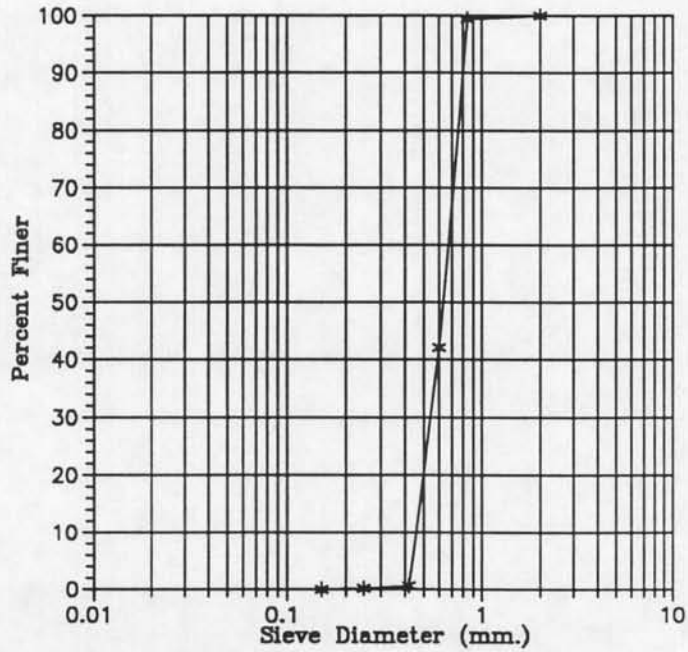


Figure B.7 Sediment size distribution for Category 3 sand (around structure).

APPENDIX C DETAILED RESULTS

In this appendix, the results of both the hydrodynamic and the scour studies are presented. The grid points defined in Table C.1 are shown in Figure 4.4.

Table C.1 Values of x and y at grid points of hydrodynamic study.

Grid Point	x (cm)	y (cm)
A1	-150.0	11.1
A2	10.2	11.1
A3	42.6	11.1
A4	71.2	11.1
A5	101.6	11.1
A6	132.1	11.1
A7	164.6	11.1
B1	-150.0	21.1
B2	10.2	21.1
B3	42.6	21.1
B4	71.2	21.1
B5	101.6	21.1
B6	132.1	21.1
B7	164.6	21.1
C1	-150.0	31.2
C2	10.2	31.2
C3	42.6	31.2
C4	71.2	31.2
C5	101.6	31.2
C6	132.1	31.2
C7	164.6	31.2

Table C.1--continued

Grid Point	x (cm)	y (cm)
D1	-150.0	44.4
D2	10.2	44.4
D3	42.6	44.4
D4	71.2	44.4
D5	101.6	44.4
D6	132.6	44.4
D7	164.6	44.4
E1	-150.0	60.7
E2	10.2	60.7
E4	71.2	60.7
E6	132.6	60.7

Table C.2 Results of hydrodynamic Test H-1.

Structure = No Pile Cap (0° to flow)
 μ = $0.801 \times 10^{-3} \text{ N}\cdot\text{sec}/\text{m}^2$
 ρ = $995.7 \text{ kg}/\text{m}^3$

Grid Point	Velocity (cm/sec)	Turbulent Energy/ Unit Mass (cm^2/sec^2)	τ_v N/m^2	τ_t N/m^2	τ N/m^2	$\frac{\tau}{\tau_o}$
A1	20.63	16.98	0.055	0.169	0.224	0.957
A2	30.05	32.72	0.080	0.326	0.406	1.733
A3	29.17	80.70	0.078	0.804	0.881	3.763
A4	23.24	71.85	0.062	0.715	0.777	3.319
A5	21.64	62.94	0.058	0.627	0.684	2.922
A6	22.07	55.70	0.059	0.555	0.614	2.619
A7	15.81	47.08	0.042	0.469	0.511	2.182
A1	21.21	18.96	0.057	0.189	0.245	1.048
B1	21.24	18.83	0.057	0.187	0.244	1.043
B2	27.69	19.43	0.074	0.193	0.267	1.142
B3	28.58	35.48	0.076	0.353	0.430	1.834
B4	26.08	44.65	0.070	0.445	0.514	2.195
B5	25.52	44.25	0.068	0.441	0.509	2.172
B6	26.75	50.07	0.071	0.499	0.570	2.433
B7	21.83	45.24	0.058	0.451	0.509	2.172
B1	21.34	18.71	0.057	0.186	0.243	1.039
C1	21.19	17.41	0.057	0.173	0.230	0.982
C2	24.90	17.35	0.066	0.173	0.239	1.021
C3	25.27	22.23	0.067	0.221	0.289	1.233

Table C.2--continued

Grid Point	Velocity (cm/sec)	Turbulent Energy/ Unit Mass (cm ² /sec ²)	τ_v N/m ²	τ_t N/m ²	τ N/m ²	$\frac{\tau}{\tau_o}$
C4	24.90	27.39	0.067	0.273	0.339	1.448
C5	24.84	30.28	0.066	0.301	0.368	1.570
C6	25.84	31.88	0.069	0.317	0.386	1.650
C7	22.41	33.67	0.060	0.335	0.395	1.687
C1	20.87	17.63	0.056	0.176	0.231	0.987
D1	19.95	16.13	0.053	0.161	0.214	0.913
D2	23.32	16.10	0.062	0.160	0.223	0.950
D3	22.97	20.09	0.061	0.200	0.261	1.116
D4	23.41	20.41	0.063	0.203	0.266	1.134
D5	23.68	22.43	0.063	0.223	0.287	1.223
D6	24.90	24.34	0.066	0.242	0.309	1.319
D7	23.24	24.86	0.062	0.248	0.310	1.322
D1	21.22	18.26	0.057	0.182	0.238	1.018
E1	20.33	17.07	0.054	0.170	0.224	0.957
E2	23.16	17.00	0.062	0.169	0.231	0.987
E4	24.21	19.09	0.065	0.190	0.255	1.087
E6	23.61	20.69	0.063	0.206	0.269	1.149
E1	20.48	17.71	0.055	0.176	0.231	0.986
A1	22.02	19.29	0.059	0.192	0.251	1.071

Estimated Shear Stress Away from Influence of Structure

Grid Point = A1 (x = -150.0 cm; y = 11.1 cm; z = 0.3 cm)

$$\tau_o = \tau_{vo} + \tau_{to} = 0.234 \text{ N/m}^2$$

$$\tau_{vo} = \mu \frac{du}{dy} = 0.056 \text{ N/m}^2$$

$$\tau_{to} = a\rho(u'^2 + v'^2) = 0.178 \text{ N/m}^2 \quad (a = 0.10)$$

Table C.3 Results of hydrodynamic Test H-2.

Structure = 70° Pile Cap - Top Position (0° to flow)
 μ = $0.801 \times 10^{-3} \text{ N} \cdot \text{sec}/\text{m}^2$
 ρ = $995.7 \text{ kg}/\text{m}^3$

Grid Point	Velocity (cm/sec)	Turbulent Energy/ Unit Mass (cm ² /sec ²)	τ_v (N/m ²)	τ_t (N/m ²)	τ (N/m ²)	$\frac{\tau}{\tau_o}$
A1	18.32	13.56	0.049	0.135	0.184	0.811
A2	35.22	43.56	0.094	0.434	0.528	2.329
A3	21.50	131.69	0.057	1.311	1.369	6.038
A4	13.70	72.00	0.037	0.717	0.753	3.324
A5	12.88	54.73	0.034	0.545	0.579	2.556
A6	13.34	59.43	0.036	0.592	0.627	2.768
A7	10.33	39.85	0.028	0.397	0.424	1.872
A1	19.66	17.74	0.052	0.177	0.229	1.011
B1	19.49	17.44	0.052	0.174	0.226	0.996
B2	28.53	24.96	0.076	0.249	0.325	1.432
B3	28.36	66.05	0.076	0.658	0.733	3.236
B4	24.20	91.22	0.065	0.908	0.973	4.292
B5	20.07	74.75	0.054	0.744	0.798	3.520
B6	20.17	68.20	0.054	0.679	0.733	3.234
B7	16.18	54.11	0.043	0.539	0.582	2.567
B1	19.34	17.68	0.052	0.176	0.228	1.005
C1	18.21	17.61	0.049	0.175	0.224	0.988
C2	27.46	23.53	0.073	0.234	0.308	1.357
C3	25.92	36.50	0.069	0.363	0.433	1.909

Table C.3--continued

Grid Point	Velocity (cm/sec)	Turbulent Energy/ Unit Mass (cm ² /sec ²)	τ_v N/m ²	τ_t N/m ²	τ N/m ²	$\frac{\tau}{\tau_o}$
C4	24.14	52.71	0.064	0.525	0.589	2.600
D1	18.66	16.79	0.050	0.167	0.217	0.958
D2	26.18	21.44	0.070	0.213	0.283	1.250
D3	25.34	27.90	0.068	0.278	0.345	1.524
D4	23.39	28.74	0.062	0.286	0.349	1.538
D5	23.10	32.39	0.062	0.323	0.384	1.695
D6	24.20	39.30	0.065	0.391	0.456	2.012
D7	22.58	41.04	0.060	0.409	0.469	2.069
D1	19.64	18.72	0.052	0.186	0.239	1.054
E1	18.50	15.57	0.049	0.155	0.204	0.902
E2	24.46	19.69	0.065	0.196	0.261	1.153
E4	24.55	24.05	0.066	0.239	0.305	1.346
E6	22.89	26.40	0.061	0.263	0.324	1.430
E1	18.12	17.24	0.048	0.172	0.220	0.971
A1	18.73	16.78	0.050	0.167	0.217	0.958
B1	19.40	18.67	0.052	0.186	0.238	1.049
C1	19.56	18.63	0.052	0.185	0.238	1.049

Estimated Shear Stress Away from Influence of Structure

Grid Point = A1 (x = -150.0 cm; y = 11.1 cm; z = 0.3 cm)

$$\tau_o = \tau_{vo} + \tau_{to} = 0.227 \text{ N/m}^2$$

$$\tau_{vo} = \mu \frac{du}{dy} = 0.051 \text{ N/m}^2$$

$$\tau_{to} = a\rho(u'^2 + v'^2) = 0.176 \text{ N/m}^2 \quad (a = 0.10)$$

Table C.4 Results of hydrodynamic Test H-3.

Structure = 70° Pile Cap - Bottom Position (0° to flow)
 μ = $0.822 \times 10^{-3} \text{ N} \cdot \text{sec}/\text{m}^2$
 ρ = $996.0 \text{ kg}/\text{m}^3$

Grid Point	Velocity (cm/sec)	Turbulent Energy/ Unit Mass (cm ² /sec ²)	τ_v N/m ²	τ_t N/m ²	τ N/m ²	$\frac{\tau}{\tau_o}$
A1	20.18	20.61	0.055	0.205	0.261	0.924
A2	17.51	69.19	0.048	0.689	0.737	2.612
A3	25.03	62.24	0.069	0.620	0.688	2.440
A4	21.67	55.89	0.059	0.557	0.616	2.183
A5	20.55	55.22	0.056	0.550	0.606	2.149
A6	22.02	48.13	0.060	0.479	0.540	1.913
A7	17.19	40.41	0.047	0.402	0.450	1.593
A1	23.27	24.03	0.064	0.239	0.303	1.074
B1	22.40	24.22	0.061	0.241	0.303	1.073
B2	34.05	72.10	0.093	0.718	0.811	2.876
B3	31.13	63.85	0.085	0.636	0.721	2.556
B4	27.80	50.26	0.076	0.501	0.577	2.044
B5	26.16	47.87	0.072	0.477	0.548	1.944
B6	26.73	45.24	0.073	0.451	0.524	1.856
B7	22.88	46.92	0.063	0.467	0.530	1.878
B1	21.86	22.28	0.060	0.222	0.282	0.999
C1	21.50	22.61	0.059	0.225	0.284	1.007
C2	30.53	41.39	0.084	0.412	0.496	1.757
C3	31.96	50.43	0.088	0.502	0.590	2.091

Table C.4--continued

Grid Point	Velocity (cm/sec)	Turbulent Energy/ Unit Mass (cm ² /sec ²)	τ_v N/m ²	τ_t N/m ²	τ N/m ²	$\frac{\tau}{\tau_o}$
C4	28.56	43.78	0.078	0.436	0.514	1.823
C5	27.76	44.54	0.076	0.444	0.520	1.842
C6	28.37	43.75	0.078	0.436	0.513	1.820
C7	24.97	41.52	0.068	0.414	0.482	1.708
C1	21.62	24.21	0.059	0.241	0.300	1.065
D1	19.92	19.75	0.055	0.197	0.251	0.891
D2	27.63	23.92	0.076	0.238	0.314	1.113
D3	27.07	33.94	0.074	0.338	0.412	1.461
D4	27.11	36.12	0.074	0.360	0.434	1.538
D5	26.27	36.97	0.072	0.368	0.440	1.560
D6	27.39	35.66	0.075	0.355	0.430	1.525
D7	25.82	34.66	0.071	0.345	0.416	1.474
D1	20.18	18.54	0.055	0.185	0.240	0.850
E1	17.08	14.09	0.047	0.140	0.187	0.663
E2	23.97	16.54	0.066	0.165	0.230	0.817
E4	25.20	19.71	0.069	0.196	0.265	0.940
E6	23.80	20.07	0.065	0.200	0.265	0.940
E1	16.17	12.63	0.044	0.126	0.170	0.603
A1	22.73	25.11	0.062	0.250	0.312	1.107
B1	21.86	22.63	0.060	0.225	0.285	1.011

Estimated Shear Stress Away from Influence of Structure

Grid Point = A1 (x = -150.0 cm; y = 11.1 cm; z = 0.3 cm)

$$\begin{aligned} \tau_o &= \tau_{vo} + \tau_{to} &= 0.282 \text{ N/m}^2 \\ \tau_{vo} &= \mu \frac{du}{dy} &= 0.059 \text{ N/m}^2 \\ \tau_{to} &= a\rho(u'^2 + v'^2) &= 0.223 \text{ N/m}^2 \quad (a = 0.10) \end{aligned}$$

Table C.5 Predicted and measured bottom elevations for scour Test S-1 (no pile cap structure).

x (cm)	y (cm)	Measured Bottom Elevation after 28 hours (cm)	τ_d	Computed Equil. Bottom Elevation based on τ_d (cm)	Computed Equil. Bottom Elevation based on angle of repose (cm)	Predicted Equil. Bottom Elevation (cm)
10	0	-13.37	14.40	-16.91	-16.91	-16.91
10	5	-10.27	6.00	-10.33	-13.79	-13.79
10	10	-7.55	1.89	-4.36	-10.66	-10.66
10	15	-5.53	1.51	-3.29	-7.54	-7.54
10	20	-3.13	1.18	-1.96	-4.42	-4.42
10	25	-1.18	1.04	-0.95	-1.29	-1.29
10	30	0.02	1.02	-0.71	1.83	-0.71
10	35	0.32	1.02	-0.65	2.41	-0.65
10	40	0.35	1.02	-0.57	2.47	-0.57
10	45	-0.03	1.01	-0.46	2.55	-0.46
10	50	0.02	1.01	-0.33	2.66	-0.33
10	55	0.15	1.00	-0.15	2.79	-0.15

Table C.5--continued

x (cm)	y (cm)	Measured Bottom Elevation after 28 hours (cm)	τ_d	Computed Equil. Bottom Elevation based on τ_d (cm)	Computed Equil. Bottom Elevation based on angle of repose (cm)	Predicted Equil. Bottom Elevation (cm)
40	0	-8.46	6.37	-10.71	-10.71	-10.71
40	5	-7.56	5.00	-9.24	-7.58	-9.24
40	10	-6.60	4.16	-8.22	-6.11	-8.22
40	15	-5.90	2.90	-6.37	-5.10	-6.37
40	20	-4.85	1.98	-4.57	-3.25	-4.57
40	25	-3.47	1.49	-3.24	-1.45	-3.24
40	30	-2.02	1.27	-2.41	0.12	-2.41
40	35	-1.32	1.16	-1.83	0.71	-1.83
40	40	-0.84	1.12	-1.58	1.29	-1.58
40	45	-0.83	1.10	-1.46	1.54	-1.46
40	50	-0.71	1.09	-1.39	1.66	-1.39
40	55	-0.60	1.08	-1.31	1.73	-1.31

Table C.5--continued

x (cm)	y (cm)	Measured Bottom Elevation after 28 hours (cm)	τ_d	Computed Equil. Bottom Elevation based on τ_d (cm)	Computed Equil. Bottom Elevation based on angle of repose (cm)	Predicted Equil. Bottom Elevation (cm)
70	0	-2.15				
70	5	-2.85				
70	10	-3.72	3.65	-7.52	-7.52	-7.52
70	15	-4.50	2.92	-6.40	-4.40	-6.40
70	20	-4.85	2.32	-5.30	-3.28	-5.30
70	25	-4.35	1.85	-4.26	-2.18	-4.26
70	30	-3.77	1.51	-3.30	-1.13	-3.30
70	35	-3.31	1.29	-2.48	-0.18	-2.48
70	40	-2.70	1.17	-1.89	0.64	-1.89
70	45	-2.53	1.33	-1.69	1.23	-1.69
70	50	-2.34	1.10	-1.46	1.43	-1.46
70	55	-1.56	1.08	-1.31	1.66	-1.31

Table C.5--continued

x (cm)	y (cm)	Measured Bottom Elevation after 28 hours (cm)	τ_d	Computed Equil. Bottom Elevation based on τ_d (cm)	Computed Equil. Bottom Elevation based on angle of repose (cm)	Predicted Equil. Bottom Elevation (cm)
100	0	2.60				
100	5	1.21				
100	10	-0.32	3.13	-6.75	-6.75	-6.75
100	15	-1.62	2.65	-5.94	-3.63	-5.94
100	20	-2.56	2.25	-5.17	-2.82	-5.17
100	25	-3.26	1.91	-4.41	-2.05	-4.41
100	30	-3.44	1.63	-3.66	-1.29	-3.66
100	35	-3.40	1.42	-2.99	-0.54	-2.99
100	40	-3.27	1.28	-2.44	-0.13	-2.44
100	45	-3.08	1.23	-2.22	0.68	-2.22
100	50	-3.01	1.20	-2.07	0.90	-2.07
100	55	-2.93	1.15	-1.79	1.05	-1.79

Table C.5--continued

x (cm)	y (cm)	Measured Bottom Elevation after 28 hours (cm)	τ_d	Computed Equil. Bottom Elevation based on τ_d (cm)	Computed Equil. Bottom Elevation based on angle of repose (cm)	Predicted Equil. Bottom Elevation (cm)
130	0	5.96				
130	5	4.66				
130	10	3.24	2.67	-5.97	-5.97	-5.97
130	15	1.40	2.57	-5.79	-2.85	-5.79
130	20	0.04	2.44	-5.55	-2.66	-5.55
130	25	-0.95	2.13	-4.90	-2.42	-4.90
130	30	-1.89	1.75	-4.00	-1.78	-4.00
130	35	-2.36	1.51	-3.29	-0.88	-3.29
130	40	-2.78	1.38	-2.86	-0.17	-2.86
130	45	-3.19	1.33	-2.66	0.26	-2.66
130	50	-3.40	1.29	-2.49	0.46	-2.49
130	55	-3.27	1.24	-2.26	0.63	-2.26

Table C.5--continued

x (cm)	y (cm)	Measured Bottom Elevation after 28 hours (cm)	τ_d	Computed Equil. Bottom Elevation based on τ_d (cm)	Computed Equil. Bottom Elevation based on angle of repose (cm)	Predicted Equil. Bottom Elevation (cm)
160	0	6.34				
160	5	6.04				
160	10	5.51	2.26	-5.18	-5.18	-5.18
160	15	4.23	2.22	-5.09	-2.06	-5.09
160	20	2.85	2.14	-4.93	-1.97	-4.93
160	25	1.71	1.98	-4.58	-1.81	-4.58
160	30	0.68	1.78	-4.08	-1.46	-4.08
160	35	-0.05	1.59	-3.54	-0.96	-3.54
160	40	-0.80	1.44	-3.07	-0.42	-3.07
160	45	-1.47	1.34	-2.69	0.05	-2.69
160	50	-2.16	1.26	-2.35	0.43	-2.35
160	55	-2.10	1.19	-2.01	0.77	-2.01

Table C.6 Predicted and measured bottom elevations for scour Test S-2 (70° pile cap structure - top position).

x (cm)	y (cm)	Measured Bottom Elevation after 28 hours (cm)	τ_d	Computed Equil. Bottom Elevation based on τ_d (cm)	Computed Equil. Bottom Elevation based on angle of repose (cm)	Predicted Equil. Bottom Elevation (cm)
10	0	-19.18	28.60	-24.27	-24.27	-24.27
10	5	-15.58	8.00	-12.22	-21.15	-21.15
10	10	-12.15	2.59	-5.83	-18.02	-18.02
10	15	-8.43	1.98	-4.57	-14.90	-14.90
10	20	-5.78	1.49	-3.22	-11.77	-11.77
10	25	-4.25	1.31	-2.59	-8.65	-8.65
10	30	-2.67	1.35	-2.72	-5.53	-5.53
10	35	-0.60	1.33	-2.66	-2.41	-2.66
10	40	0.04	1.27	-2.39	0.46	-2.39
10	45	-0.27	1.20	-2.07	0.73	-2.07
10	50	-0.14	1.17	-1.91	1.05	-1.91
10	55	-0.02	1.15	-1.79	1.21	-1.79

Table C.6--continued

x (cm)	y (cm)	Measured Bottom Elevation after 28 hours (cm)	τ_d	Computed Equil. Bottom Elevation based on τ_d (cm)	Computed Equil. Bottom Elevation based on angle of repose (cm)	Predicted Equil. Bottom Elevation (cm)
40	0	-11.50	10.92	-14.55	-14.55	-14.55
40	5	-10.70	9.00	-13.07	-11.42	-13.07
40	10	-8.54	6.67	-11.00	-9.95	-11.00
40	15	-8.73	4.81	-9.02	-7.88	-9.02
40	20	-7.81	3.41	-7.18	-5.90	-7.18
40	25	-5.96	2.53	-5.71	-4.06	-5.71
40	30	-4.25	1.99	-4.59	-2.59	-4.59
40	35	-3.43	1.69	-3.84	-1.47	-3.84
40	40	-2.51	1.57	-3.47	-0.72	-3.47
40	45	-1.87	1.45	-3.10	-0.35	-3.10
40	50	-1.30	1.35	-2.73	0.02	-2.73
40	55	-0.33	1.35	-2.31	0.39	-2.31

Table C.6--continued

x (cm)	y (cm)	Measured Bottom Elevation after 28 hours (cm)	τ_d	Computed Equil. Bottom Elevation based on τ_d (cm)	Computed Equil. Bottom Elevation based on angle of repose (cm)	Predicted Equil. Bottom Elevation (cm)
70	0	-1.87				
70	5	-2.97				
70	10	-4.11	3.12	-6.73	-6.73	-6.73
70	15	-5.02	3.86	-7.81	-3.61	-7.81
70	20	-5.12	4.19	-8.26	-4.69	-8.26
70	25	-3.89	3.71	-7.60	-5.14	-7.60
70	30	-3.19	2.84	-6.26	-4.48	-6.26
70	35	-2.18	2.19	-5.04	-3.14	-5.04
70	40	-1.82	1.78	-4.09	-1.92	-4.09
70	45	-2.02	1.55	-3.43	-0.97	-3.43
70	50	-2.31	1.45	-3.10	-0.31	-3.10
70	55	-2.18	1.36	-2.77	0.02	-2.77

Table C.6--continued

x (cm)	y (cm)	Measured Bottom Elevation after 28 hours (cm)	τ_d	Computed Equil. Bottom Elevation based on τ_d (cm)	Computed Equil. Bottom Elevation based on angle of repose (cm)	Predicted Equil. Bottom Elevation (cm)
100	0	5.59				
100	5	3.49				
100	10	2.25	2.29	-5.24	-5.24	-5.24
100	15	0.76	3.00	-6.53	-2.11	-6.53
100	20	-0.46	3.44	-7.22	-3.41	-7.22
100	25	-0.80	3.48	-7.27	-4.10	-7.27
100	30	-1.15	3.20	-6.85	-4.15	-6.85
100	35	-1.03	2.73	-6.07	-3.73	-6.07
100	40	-0.83	2.15	-4.96	-2.95	-4.96
100	45	-1.09	1.61	-3.61	-1.84	-3.61
100	50	-1.27	1.49	-3.23	-0.49	-3.23
100	55	-1.50	1.39	-2.88	-0.11	-2.88

Table C.6--continued

x (cm)	y (cm)	Measured Bottom Elevation after 28 hours (cm)	τ_d	Computed Equil. Bottom Elevation based on τ_d (cm)	Computed Equil. Bottom Elevation based on angle of repose (cm)	Predicted Equil. Bottom Elevation (cm)
130	0	9.55				
130	5	8.45				
130	10	7.32	2.68	-5.99	-5.99	-5.99
130	15	5.96	2.98	-6.51	-2.87	-6.51
130	20	4.56	3.21	-6.87	-3.39	-6.87
130	25	3.12	3.36	-7.09	-3.75	-7.09
130	30	2.11	3.34	-7.06	-3.97	-7.06
130	35	1.09	3.01	-6.56	-3.94	-6.56
130	40	0.59	2.48	-5.62	-3.44	-5.62
130	45	0.29	1.95	-4.50	-2.50	-4.50
130	50	-0.27	1.58	-3.52	-1.38	-3.52
130	55	-0.52	1.43	-3.01	-0.40	-3.01

Table C.6--continued

x (cm)	y (cm)	Measured Bottom Elevation after 28 hours (cm)	τ_d	Computed Equil. Bottom Elevation based on τ_d (cm)	Computed Equil. Bottom Elevation based on angle of repose (cm)	Predicted Equil. Bottom Elevation (cm)
160	0	10.10				
160	5	9.80				
160	10	9.42	2.07	-4.77	-4.77	-4.77
160	15	8.36	2.31	-5.29	-1.65	-5.29
160	20	6.81	2.53	-5.72	-2.17	-5.72
160	25	5.50	2.65	-5.93	-2.60	-5.93
160	30	4.62	2.62	-5.87	-2.81	-5.87
160	35	3.46	2.49	-5.64	-2.75	-5.64
160	40	2.56	2.29	-5.26	-2.52	-5.23
160	45	1.75	2.07	-4.78	-2.14	-4.78
160	50	1.20	1.86	-4.28	-1.66	-4.29
160	55	0.58	1.49	-3.23	-1.16	-3.23

Table C.7 Predicted and measured bottom elevations for scour Test S-3 (70° pile cap structure - bottom position).

x (cm)	y (cm)	Measured Bottom Elevation after 28 hours (cm)	τ_d	Computed Equil. Bottom Elevation based on τ_d (cm)	Computed Equil. Bottom Elevation based on angle of repose (cm)	Predicted Equil. Bottom Elevation (cm)
10	0					
10	5					
10	10	-12.96	2.47	-5.61	-5.61	-5.61
10	15	-12.21	2.80	-6.19	-2.45	-6.19
10	20	-9.53	2.89	-6.35	-3.07	-6.35
10	25	-6.50	2.57	-5.79	-3.23	-5.79
10	30	-3.32	1.94	-4.48	-2.67	-4.48
10	35	-0.70	1.44	-3.07	-1.36	-3.07
10	40	0.32	1.20	-2.04	0.05	-2.04
10	45	0.56	1.11	-1.50	1.08	-1.50
10	50	0.57	1.07	-1.23	1.62	-1.23
10	55	0.71	1.07	-1.21	1.89	-1.21

REFERENCE LIST

- Brown, C.B. (1950) "Sediment Transportation," in Engineering Hydraulics, H. Rouse, Ed. Wiley, New York, 145-180.
- Carstens, T. and H.R. Sharma (1975) "Local Scour Around Large Obstructions," Proc. of the Intl. Assoc. for Hydraulic Research, 16th Cong., Vol. 2, Sub. B, 251-262.
- Chang, F.M., D.B. Simons and E.V. Richardson (1967) "Total Bed-Material Discharge in Alluvial Channels," Proc. of the Intl. Assoc. for Hydraulic Research, 12th Cong., Vol. 1, Sub A, 131-140.
- Du Boys, M.P. (1879) "Le Rhone et les Rivieres a lit Affouillable," Mem. Doc. Ann. Ponts Chausses, Ser. 5, Vol. 18, 141-195.
- Ettema, R. (1976) Influence of Bed Material Gradation on Local Scour, School of Engineering Report No. 124, University of Auckland, Auckland, New Zealand, 48 p.
- Garde, R.J. and M.L. Albertson (1958) Discussion of "The Total Sediment Load in Streams," by E.M. Laursen, J. of Hydraulic Division, Vol. 84, No.6, 1856-1864.
- Goldstein, R.J. (1983) Fluid Mechanics Measurements, Hemisphere Publishing Company, New York, 630 p.
- Hannah, C.R. (1978) Scour at Pile Groups, Master of Engineering Thesis at the University of Canterbury, Christchurch, New Zealand, 92 p.
- Hjorth, P. (1974) Lokal Erosion kring Bropelare och Rorledninggar, Institutionen for Vattenbyggnad, Tekniska Hogskolan i Lund, Bulletin Serie A nr. 30, 49 p.
- Jones, J.S. (1989) "Laboratory Studies of the Effects of Footings and Pile Groups on Bridge Pier Scour," Proc. of the Bridge Scour Symp., Washington D.C., Oct. 17-19, 340-360.
- Jones, J.S., R.T. Kilgore and M.P. Mistichelli (1992) "Effects of Footing Location on Bridge Pier Scour," J. of Hydraulic Engineering, Vol. 118, No.2, 280-290.

- Jones, J.S., S.M. Stein and R.T. Kilgore (1990) Lab Report for the Acosta Bridge Scour Study, Pub. No. FHWA-RD-89-114, Federal Highway Administration, Mclean, Virginia, 89 p.
- Melville, B.W. and A.J. Raudkivi (1977) "Flow Characteristics in Local Scour at Bridge Piers," J. of Hydraulic Research, Vol. 15, No.4, 373-380.
- O'Brien, M.P. and B.D. Rindlaub (1934) "Transportation of Bed-Load by Streams," Transactions of the American Geophysical Union, 15th Annual Meeting, Berkeley, California, June 20-21, 593-603.
- Raudkivi, A.J. (1976) Loose Boundary Hydraulics, 2nd ed., Pergamon Press, New York, p. 36.
- Shen, H.W., V.R. Schneider and S.S. Karaki (1966) Mechanics of Local Scour, Colorado State University, Civil Engineering Dept., Fort Collins, Colorado, Pub. No. CER66HWS22, 56p.
- Sheppard, D.M. and A.W. Niedoroda (1992) Structure-Induced Sediment Scour, Local Scour Bounds & Assessments of Global Scour, Final Report to Florida Dept. of Natural Resources, UPN No. 90100412, University of Florida, Gainesville, 84 p.
- Sheppard, D.M. and A.W. Niedoroda (1990) Local Structure-Induced Sediment Scour, Final Report to Florida Dept. of Transportation, C-5749, University of Florida, Gainesville, 60p.
- Shields, A. (1936) Anwendung der aehnlichkeitsmechanik und er turbulenz forschung auf die geschiebebewegung, Mitt. Preuss. Versuchsanstalt Wasserbau Schiffbau., Vol. 26, 94 p.
- Sleath, J.F.A. (1984) Sea Bed Mechanics, John Wiley & Sons, New York, 335 p.